Feasibility Theory

by

Brian Alexander Cohn

A Dissertation Presented to the
FACULTY OF THE USC GRADUATE SCHOOL
UNIVERSITY OF SOUTHERN CALIFORNIA
In Partial Fulfillment of the
Requirements for the Degree
DOCTOR OF PHILOSOPHY
Computer Science

December 2020

Acknowledgements

I would like to express my strongest gratitude to my advisor, Francisco J. Valero-Cuevas, who both led me toward a path of adventure, and instilled in me a new sense of scientific curiosity. With his support I sought new angles in research, invented new tools to solve problems, and enjoyed a path of discovery. To my committee members, Heather Culbertson, Stefanos Nikolaidis, Lori Michener, and Gaurav S Sukhatme, I am deeply thankful for their support in shaping my perspectives from the view-points of clinical medicine, bio-robotics, and theoretical computer science; these perspectives shaped the story this dissertation tells. My appreciation extends to my fellow members of the Brain-Body Dynamics Laboratory——my unwavering support network that kept the ship afloat. And finally, I am extremely grateful to my friends and family, who are my greatest inspiration and my strongest source of joy.

Table of Contents

List Of Tables

List Of Figures

Abstract

Feasibility Theory is a conceptual and computational approach to understand the dimensionality of how tendon-driven limbs are controlled. How do the brains of animals control their bodies? This remains one of the deepest mysteries in biology, a concept with an enormous consequence upon how we understand, diagnose, and treat diseases or injuries that rob animals of manipulation and locomotion. Engineers and scientists have tackled this problem from rigorous mathematical and scientific perspectives and much progress has been made—primarily descriptive approaches that attempt to predict how the nervous system solves a motor task (e.g. modeling observed behavior based on recordings of muscle activity). However, this rigor has a downside: the efficient ways we know how to solve problems mathematically (via formal optimization) can surreptitiously bias the scientific community into hypothesizing that the brain also solves problems this way. These methods describe how the muscles function, but they do not describe **why** certain patterns of control are evolved (over millennia), learned (over a lifetime), or chosen (within just one motor task). The work presented herein delves into the problem from a full-dimensional perspective of motor control—requiring a truly Big Data exploration into, first, a view of the feasible options for control, and second, a set of constraints which faithfully describe the ways in which tendon-driven limbs truly *must* be controlled. I present new mathematically formal ways to show that many muscles are indeed needed even for *simple tasks*, and indicate how even the most 'optimal' solutions are highly prone to disruption, even with minor disability of just one muscle. I propose new computational methods for reconciling alternative approaches to motor control, including techniques in dimensionality reduction, Bayesian representation, and optimization. Ultimately, this work now enables a new perspective towards exploring how motor control affects health and quality of life.

Chapter 1

Exploring the high-dimensional structure of muscle redundancy via subject-specific and generic musculoskeletal models

Francisco J. Valero-Cuevas,[1,2],* Brian A. Cohn,[1] Hördur F. Ingvason,[3] and Emily L. Lawrence[1]

[1]Department of Biomedical Engineering, University of Southern California, Los Angeles, CA, USA

[2]Division of Biokinesiology and Physical Therapy, University of Southern California, Los Angeles, CA, USA

[3]Swiss Federal Institute of Technology-Zurich, Zurich, Switzerland

1.1   Abstract

Subject-specific and generic musculoskeletal models are the computational instantiation of hypotheses, and stochastic techniques help explore their validity. We present two such examples to explore the hypothesis of muscle redundancy. The first addresses the effect of anatomical variability on static force capabilities for three individual cat hindlimbs, each with seven kinematic degrees of freedom (DoFs) and 31 muscles. We present novel methods to characterize the structure of the 31-dimensional set of feasible muscle activations for static force production in every 3-D direction. We find that task requirements strongly define the set of feasible muscle activations and limb forces, with few differences comparing individual vs. species-average results. Moreover, muscle activity is not smoothly distributed across 3-D

directions. The second example explores parameter uncertainty during a flying disc throwing motion, by using a generic human arm with five DoFs and 17 muscles to predict muscle fiber velocities. We show that the measured joint kinematics fully constrain the eccentric and concentric fiber velocities of all muscles via their moment arms. Thus muscle activation for limb movements is likely not redundant: there is little, if any, latitude in synchronizing alpha-gamma motoneuron excitation-inhibition for muscles to adhere to the time-critical fiber velocities dictated by joint kinematics. Importantly, several muscles inevitably exhibit fiber velocities higher than thought tenable, even for conservative throwing speeds. These techniques and results, respectively, enable and compel us to continue to revise the classical notion of muscle redundancy for increasingly more realistic models and tasks.

1.1.0.1 Author Contribution

My primary contribution to this work was the extension of [113], invention of the methods for generating FAS and FFS species averages, and the invention of vector mapping for tendon-driven feasible activation sets. Further, I contributed to the analysis and visualization of frisbee-throwing by EL.

1.2 Introduction

This invited paper has the dual purpose of being didactic about computational methods to test neuromechanical hypotheses in the context of high-dimensional subject-specific and generic models; and applying these methods to explore the classical notion of muscle redundancy, a central tenet in our field. This is made possible by computational geometry and stochastic techniques we have been developing to understand the interactions among (i) model topology (the number and type of and connectivity among the elements of the model); (ii) parameters values (the individual and specific numerical values assigned to each model parameter); and (iii) the requirements of real-world tasks for tendon-driven biomechanical systems with numerous kinematic degrees of freedom and muscles.

The notion of computational models as instantiations of specific hypotheses, the stochastic exploration of model capabilities to test these hypotheses, and the relationship between generic vs. subject-specific models has been addressed elsewhere [151, 150, 98, 65, 155]. However, increasing the physiological realism and utility of these techniques requires extending them to ever higher dimensions (i.e., larger numbers of muscles and kinematic degrees-of-freedom, DoFs), and to real-world tasks involving the production of static forces and fast motions—while limiting computational cost. But working with ever-greater numbers of muscles and DoFs inevitably challenges our ability to visualize the complex and high-dimensional structure of the set of feasible muscle activation patterns. It also significantly challenges our ability to find unique solutions (if they even exist) to these computational problems, or defend their optimality/uniqueness.

We have found these stochastic modeling techniques particularly useful to test the classical notion of muscle redundancy, which has often been called the central problem of motor control [16]. The classical notion of muscle redundancy is thought to arise by virtue of having (many) more muscles than DoFs. With many muscles acting upon the same number or fewer joints, some argue that the central nervous system (CNS) must solve an optimization problem to select and implement specific muscle activation patterns from a theoretically infinite set of possibilities [93, 105]; while others argue for near- or sub-optimal solutions being good enough [80, 105]. If fewer muscles actuated a limb, the arguments go, feasible forces and motions could be produced without significant need for such optimizations.

Several of us have argued that this classical interpretation of the number of muscles in vertebrate limbs is paradoxical with respect to evolutionary biology, and the clinical reality of motor dysfunction: extant vertebrates tend to have many more muscles than DoFs, even though it is energetically expensive to develop and maintain muscle mass—and injury to even a few muscles can cause dysfunction. Using the same argument of energetic efficiency invoked for optimization in motor control—but at the scale of evolutionary time—we, and others, have argued that we likely have barely enough muscles for versatile real-world behavior [64, 79, 147, 72, 74]. This view is closely aligned with the computational neuroethology approach [11, 7, 28] that argues that perhaps we need all our muscles because of the sheer variety

3

of tasks—each distinguished by the type and number of constraints they must meet—over the course of a day/week/lifespan. Put differently, if we have too many muscles in our limbs, which ones would you like to donate or paralyze? Therefore, it is important that our research into muscle redundancy work toward reconciling these different views.

Still, for most tasks in healthy individuals, some redundancy is bound to remain; regions of feasible activation solutions that are not a single point will consist of a neighborhood or subspace that naturally contains an infinite number of solutions (i.e., points). The nervous system is still confronted with the need to choose a specific solution to implement at any point in time; however, that collection of feasible solutions remains highly structured due to both the mechanics of the limb and the constraints of the task [113, 72, 74, 156, 133, 17]. The purpose of this work, therefore, is to begin to address the need posed by us [72, 74, 156], and others [113, 79, 133], to improve computational methods for understanding and visualizing the dimensionality and structure of feasible solutions sets for limbs with large numbers of muscles performing tasks with realistic constraints. Here we do so for 3-D musculoskeletal models of a cat hindlimb and a human arm with 31 and 17 muscles, respectively, using MATLAB (v2013b, The Mathworks, Natick MA).

1.3   Cat hindlimb model: Methods

The purpose of this cat hindlimb model is to present a novel way to visualize the structure of the set of all feasible muscle activations to produce maximal and submaximal static paw forces in every 3-D direction. In addition, we compare solutions among three subject-specific models to explore the effect of between-subject anatomical variability on muscle activation. The models consist of three feline (Felis catus) hindlimbs, each with 31 muscles actuating 7 kinematic DoFs from the hip to the ankle. We used the bone lengths and moment arms for the cat hindlimbs originally presented by McKay and Ting in 2008 [87], and modified by Sohn et al. 2013 [113], that were graciously shared with us by the authors. The species average model for the cat hindlimb is shown in Figure 1.3.

As described in detail elsewhere (e.g., [156, 86, 148]), a feasible force set (FFS) describes the set of all static forces that can be produced at the endpoint of a limb. Briefly, the feasible mechanical output of the endpoint of a limb is 6-dimensional: 3 forces (the FFS) and 3 torques (the feasible output torque set)—which arises from the fact that a rigid body (i.e., the endpoint of a limb) has six degrees of freedom, three displacements and three rotations. Together they form a 6-dimensional feasible output wrench [89]. In the robotics literature [88], feasible force and torque outputs are plotted separately as they have different units. Thus the FFS can be at most 3-D, and is a subset of the feasible wrench set. For the task of producing pure output force as in this model, we enforce the constraint that the endpoint produce no output torques [156]. Thus the FFS is the complete representation of the maximal mechanical output of the limb. For limb models constrained to move on a plane, the FFS is a convex 2-D polygon (Figure 1.4.2, Left). For models that can move in 3-D space, the FFS is a convex 3-D polyhedron (Figure 2, Center) with its origin at the endpoint of the limb [156, 148].

Importantly, as described elsewhere [156, 86, 148, 71], the FFS is produced by the feasible activation set (FAS)—the set of all muscle activations that meet the constraints of the task. For linear constraints as in this case, the FAS is a convex polytope in n-dimensional space, where n is the number of independently controlled muscles acting on the limb. The FAS is at the center of studies of muscle redundancy because it contains an infinite number of points. Sometimes this subspace is called the nullspace of the task as any point in it can, by construction, meet its constraints [24]. But it is nevertheless a highly structured subset of n-dimensional space. A critical result of our work is that we present a means to visualize and characterize the FFS by examining one muscle at a time.

1.3.1   Vector mapping of the feasible force set

It is challenging to understand and visualize a 3-D FFS, as it is an irregularly shaped convex polyhedron (Figure 2, Center). Likewise, those difficulties are exacerbated for the FAS as it is also an irregularly shaped polytope, but in high dimensions. As mentioned in the Introduction, it is critical to understand the structure of the FFS and FAS as they lie at the heart of many debates about muscle redundancy, muscle synergies,

disability, rehabilitation, motor learning, etc. One approach to connect the structure of the FFS and the FAS is by computing their bounding boxes (i.e., the extreme points in every dimension [113, 72, 59]). However, this overestimates both their size and volume, and ignores the complexity of their structure. Another possibility is to find the largest sphere the polytope can encase [59], but this underestimates their size and volume, and assumes a uniform structure. We now propose an alternate method that helps us visualize the structure of the FFS, in a 'vectormap'. After identifying the maximum feasible force in a given direction (Figure 2, Left), we assign that value of force to a 3-D point, where color denotes the force intensity. A spherical heatmap is formed with all of the computed directions and respective maximum forces; Figure 2 (Right) shows the vectormap representation of the FFS.

Traditionally, polyhedra like the FFS cannot be combined or compared quantitatively because the vertices do not align across different individual musculoskeletal models. As vectormaps are composed of consistent unit vectors for force output (or muscle activation, see next section), they can be averaged and compared. For example, they can be compared across individuals of a species to identify regions that have higher variability within a population. The color on the surface of the sphere can then be used to represent the mean or standard deviation of maximal output force or muscle activation (Figure 3).

1.3.2   Vector mapping of the feasible activation set

We present a way to visualize the structure of the FAS, a convex polytope in n-dimensional space, on a muscle-by-muscle basis. For each muscle we can generate activation vectormaps where color represents its unique activation level for every point on the surface of the FFS (Figure 4). This is possible because any point on the surface of the FFS (i.e., the maximal force in every direction) is generated by a unique muscle activation pattern [156]. This unique activation pattern assigns the color to that point on the vectormap of each muscle. In the case of the cat hindlimb there are 31 muscles, and therefore, 31 vectormaps of unique muscle activations.

Importantly, submaximal forces in each 3-D direction (i.e., points within the FFS) can be produced by an infinite number of solutions [21, 30]. The structure of those solutions can be approximated by the

6

bounding box approach in [113, 72]. We extend that prior work by creating vectormaps of the lower and upper bounds of activation for each muscle, for all directions in 3-D (Figure 4).

1.4 Cat hindlimb model: Results

1.4.1 Intra-species differences in the feasible force set

With one FFS per cat, we find that force capability distributions for the three cats can differ in specific 3-D directions. Figure 3 shows between-cat comparisons: a species average (top), and standard deviation (bottom) plots across the three FFSs. We see that species average and individual FFSs are of the same general shape (c.f. Figure 2, Right and Figure 3, Top) with maximal force magnitudes remaining in the same general direction (towards the posterior direction) and of similar magnitude (c. 60 N) as for the individual cat in Figure 2. However, the standard deviation among the FFSs of the three cats can show important differences in the range of 20 N in those same directions as the maximal magnitude. But in most other 3-D directions the differences remain below 5 N.

1.4.2 Structure of feasible activation sets

Figure 4 shows what to our knowledge is the first portrayal of the structure of the FAS for force production in every 3-D direction. For the sake of brevity, we only show the results for three muscles. The plots for all 31 muscles are available at https://valerolab.org. The vectormaps on the far right show the unique level of activation for maximal feasible forces in all directions. While in several 3-D directions that activity of a muscle can remain unchanged, we also see discontinuities where muscle activity is not smoothly distributed across 3-D directions as, for example, the 'fingers' of higher activations penetrating into areas of lower activations for *vastus lateralis*.

To extend prior work [113, 72], we also found the lower and upper bound vectormaps for all muscles for submaximal forces in all 3-D directions. This is the bounding box approach in [113, 72], but extended to every direction in 3-D. These plots provide a detailed view of the structure of the 31-dimensional FAS

7

for different force magnitudes, viewing one muscle at a time. The smaller vectormaps to the left in Figure 4 show the lower and upper bounds as one increases force magnitude in all directions in 10% steps, starting at 50% of maximal force. The lower and upper bounds naturally converge for maximal output, but they converge at different rates across muscles and directions of force output—sometimes towards the upper bound, and sometimes towards the lower bound. These vectormaps of the FAS enable us to understand the rate at which redundancy is 'lost,' or not for every direction of force production. They also enable future studies where, say, the loss of the *soleus* muscles, or its hypertonia, are simulated by driving its activation to the lower or upper bound, respectively, to visualize the feasible range of compensations by other muscles.

1.5   Human arm model: Methods

The purpose of this human arm model is to understand the constraints imposed on time varying muscle activation during the kinematics of a high-speed athletic movement. Specifically, our model predicts muscle fiber lengths and velocities during a specific athletic activity—in this case throwing a flying disc with a backhand motion, like throwing a Frisbee®. A five-DoF, 17-muscle arm model of the right arm was modeled after [1], and consisted of three joints (shoulder, elbow, and wrist) articulating three limb segments (upper arm, lower arm, and hand) with lengths of 0.35m, 0.27m, and 0.11m, respectively (Figure 5). The three DoFs at the shoulder included internal/external rotation, abduction/adduction, and horizontal abduction/adduction, and the DoF at both the elbow and wrist is flexion/extension. We note that our simplified model does not consider all DoFs at the elbow and wrist. This limitation affects the calculation of joint angles and fiber velocities, but likely does not challenge our results as in some cases fiber velocity would be somewhat lower, but also somewhat higher. We added 17 muscles/muscle groups with resting fiber length and moment arm data from various sources [48, 51, 56, 90]. The moment arm data are shown in Figure 5.

1.5.1 Kinematics of throwing a flying disc and resulting muscle fiber velocities

The time-history of joint angles of the throwing motion were also obtained from [58]. We considered the initiation of forward motion, release, and follow-through portions of the throw to last, conservatively, 450ms; and approximated it as 45 unique postures at 10ms time steps, as illustrated in Figure 6. We combined measured limb kinematics with moment arm values to predict the instantaneous normalized muscle fiber velocity throughout the throw (Fig. 5).

Consider a tendon-driven limb with n muscles (17 in this case) and m joints (or DoFs, five in this case), and a limb posture defined by joint angles $\theta = [\theta_1...\theta_m]^T$. The moment arm matrix $R(\theta)^{mxn}$ can be defined for this tendon-driven system, having entries consisting of the moment arms $r(\theta)_{i,j} : i = 1,...,m, j = 1,...,n$, at the ith joint and j^{th} muscle [5] forming the posture-dependent moment arm matrix 1.1

$$R(\theta) = \begin{pmatrix} r(\theta)_{1,1} & r(\theta)_{1,2} & r(\theta)_{1,3} & \ldots & r(\theta)_{1,n} \\ r(\theta)_{2,1} & r(\theta)_{2,2} & r(\theta)_{2,3} & \ldots & r(\theta)_{2,n} \\ \vdots & \vdots & \vdots & \vdots & \vdots \\ r(\theta)_{m,1} & r(\theta)_{m,2} & r(\theta)_{m,3} & \cdots & r(\theta)_{m,n} \end{pmatrix} \tag{1.1}$$

As per the right-hand-rule, $r(\theta)_{i,j}$ is positive when pulling j^{th} tendon induces a counterclockwise rotation at the ith joint, and negative otherwise. A postural change is a rotation of joints from a reference limb posture $\theta_0 = [\theta_1...\theta_m]^T$ to a new limb posture $\theta_0 = [\theta_1...\theta_m]^T$ and is denoted $bm\Delta\theta = \theta - \theta_0 = [\Delta\theta_1...\Delta\theta_m]^T$. fully determines the excursions Δ_s of all n muscles [36], where negative and positive excursion values correspond to eccentric and concentric contractions, respectively:

In this case we obtain the over-determined system where the changes of angles of a few variables (the joint angles) specify the excursions of all the many muscles.

$$\Delta s = -\boldsymbol{R^T}(\boldsymbol{\theta})\Delta\boldsymbol{\theta} = - \begin{pmatrix} r(\boldsymbol{\theta})_{1,1} & r(\boldsymbol{\theta})_{2,1} & \cdots & r(\boldsymbol{\theta})_{5,1} \\ r(\boldsymbol{\theta})_{1,2} & r(\boldsymbol{\theta})_{2,2} & \cdots & r(\boldsymbol{\theta})_{5,2} \\ r(\boldsymbol{\theta})_{1,3} & r(\boldsymbol{\theta})_{2,3} & \cdots & r(\boldsymbol{\theta})_{5,3} \\ \vdots & \vdots & \vdots & \vdots \\ r(\boldsymbol{\theta})_{1,17} & r(\boldsymbol{\theta})_{2,17} & \cdots & r(\boldsymbol{\theta})_{5,17} \end{pmatrix} \Delta\boldsymbol{\theta} \tag{1.2}$$

To be clear, this is the very opposite of redundancy.

When the interval between postures is allotted a given amount of time, the instantaneous velocity of the muscle fibers is

$$\nu = \frac{\Delta s}{\Delta t} \tag{1.3}$$

Please note that the velocity of the muscle fibers is not necessarily the velocity of the musculotendon. Muscle fiber pennation angle and tendon elasticity can both contribute to this [160]. For the sake of simplicity, and without loss of generality, we assume muscle fibers span the length of the whole muscle and have a small pennation angle so that we can consider them to be equivalent. A recent modeling study [42] also suggests that 'paradoxical' contractions—where the extreme case of muscle fibers shortening while the musculotendon as a whole is lengthening due to tendon stretch—are brief events limited mostly to large eccentric contractions to reverse movement direction. Due to these reasons, we assumed the velocities of the muscle fibers and tendons were mostly equivalent during the midsection of the uni-directional throwing motion we consider in our analysis. As is customary, we calculated the normalized muscle fiber length velocities by dividing fiber velocities by the resting muscle fiber length (l_O) of each muscle [160].

$$\bar{v} = \frac{v}{l_o} \tag{1.4}$$

1.6   Human arm model: Results

1.6.1   Muscle fiber velocities for flying disc throw

Figure 7 shows the normalized muscle fiber velocities for all muscles during a 450ms flying disc-throwing motion. Notice that multiple muscles have normalized muscle fiber velocities exceeding ± 5 fiber lengths/s (deep blue and deep red in Figure 7 Top, respectively). Because these high velocities are considered to be unrealistically fast [160, 55], we used Monte Carlo simulations to explore the robustness of our findings (Figure 7, Bottom). As is often done in musculoskeletal modeling [151], we explored the effect of modeling uncertainty by iteratively running our model while sampling parameter values from uniform distributions spanning $\pm 25\%$ of the nominal moment arm values. Given that the joint kinematics and segment lengths come from direct measurements, our stochastic approach focused in the uncertainty of moment arm values obtained from the literature as they may or may not be appropriate for the arm of the subject who performed the flying disc throw. Note we fixed the duration of the motion to 450ms because, although slow in comparison to competitive athletes, it provides a conservative estimate of muscle fiber velocities and thus a more reasonable and defensible set of results. We guaranteed convergence of the Monte Carlo simulation by testing the variability of the running mean of normalized fiber velocity of the *infraspinatus* [151].

This muscle experienced the largest lengthening velocities, and as such, was at the greatest risk for injury. Only twelve iterations sufficed for the running mean of the maximal *infraspinatus* normalized fiber velocity to vary less than 2%. Running the Monte Carlo simulation for more iterations unnecessarily increases processing time without refining the results of maximal fiber velocities for this task. The results of our Monte Carlo simulation (Figure 7, Bottom) provide confidence in the assertion that the task of throwing a flying disc using a stroke that lasts 450ms will induce multiple muscles to exhibit normalized fiber velocities exceeding ± 5 fiber lengths per second.

1.7 Discussion

In this invited methods-driven paper, we present two examples of computational methods to test neurome-chanical hypotheses in the context of subject-specific and generic models, and apply these methods to explore different aspects of the classical notion of muscle redundancy. In the first example, three indi-vidual models of a cat hindlimb with 31 muscles allowed us to investigate the intra-species variation in maximal force production. This was made possible by novel computational and visualization techniques to complement a computational geometry approach to the control of tendon-driven limbs. The results presented in this manuscript, and supplemental results online at https://valerolab.org, allows us to, for the first time, describe detailed features of intra-species differences in maximal force production, and of the structure of the 31-dimensional feasible set of muscle activation patterns for submaximal and maximal forces in all 3-D directions. In the second example, we used stochastic Monte Carlo methods to demon-strate that the kinematics of the everyday recreational and sports task of throwing a flying disc inevitably leads to unexpectedly fast eccentric and concentric muscle fiber velocities. These two examples challenge different aspects of the classical notion of muscle redundancy, and lead to specific new testable hypotheses to move our field forward. It is useful to first mention that the analytical support for the perspective that musculature is not as redundant as we have come to believe comes from examining the set of feasible muscle activations that gives rise to the set of feasible limb outputs [156, 71]. This is the counterpart to using an optimization approach to find a single unique and optimal solution to that task [147, 156]. Rather, it seeks to find the set of all feasible muscle activation strategies that, naturally and by construction, are a well-defined region in the high-dimensional space formed by the intersection of all operating mechanical constraints of the task, given the anatomy of the limb. Therefore, the number of constraints that define the task is as important as the number of muscles in the limb—where more muscles allow meeting a greater variety and number of functional constraints [64, 79, 158].

Thus an argument against the classical notion of muscle redundancy is that the number of muscles in vertebrate limbs has evolved under functional constraints of versatile real-world behavior [64, 79, 147, 72,

74, 156]. We can perform 'complex' tasks (complexity defined as satisfying many constraints simultane-

ously or sequentially [79]) because we have many muscles—and muscle redundancy is most prominently

seen in laboratory tasks that are too simple, and not equivalent to tasks in the natural environment [28]. This

view is compatible with the above reasoning that a task is defined by the type and number of constraints

that must be met. The geometric approach to define feasible outputs and their associated feasible neural

inputs (FFS and FAS, respectively) provides a rigorous computational approach to the concept of muscle

redundancy. Thus muscle redundancy is really more a feature of the task than of the limb [64, 79, 158].

1.7.1 Structure of the feasible activation and feasible force sets of the cat hindlimb

We present the vectormap as an innovative way to visualize and analyze the structure of the irregular FFS

polyhedra and FAS polytopes that result from the interaction of the biomechanics of the limb and the

constraints of the task. This allows us not only to interpret individual feasible sets, but also provide a

coordinate system (i.e., the surface of the sphere) to combine or compare feasible sets. This differs from

prior approaches that have compared their relative volume, shape, or bounding box, as described above.

Figure 3 identifies the specific 3-D directions and regions of feasible force generation that exhibit the high-

est variability across three individuals of a species. This has applications to, for example, understanding

how phenotypical (i.e., anatomical) changes lead to behavioral changes in feasible force and activation on

which evolutionary selection may act.

It is of critical interest to the field of neural control to understand why extant vertebrates have 'so many'

muscles—yet we previously lacked means to visualize the structure of the set of feasible muscle activations

for a given task. The main difficulty is that selecting a given muscle activation pattern necessitates selecting

a point from within the set of all feasible activations determined by the mechanics of the limb and the

constraints of the task [74, 156, 133]. As described above, prior work approximated the structure of

feasible activations for force production in a given direction by their bounding box [113, 72, 74]. In

Figure 4 we present how it is now possible to visualize the lower and upper bounds of feasible levels of

activation for each and every muscle when producing submaximal force in every 3-D direction. It can be

quite striking that even for very near maximal activation (i.e., at 90%), the range in between these upper and lower bounds can be exceptionally wide, as in Figure 4. This had been reported in a single direction of force production by [113], but here we can show the rate of convergence to the unique solution for maximal force for every direction of force production.

The wide (or narrow) latitudes in allowable coordination patterns for submaximal force seem to very clearly demonstrate that trying to find and justify a 'unique' solution to these types of problems is highly dependent on the task and the cost function chosen. Note that in other muscles and/or directions this rate of loss of redundancy can proceed at different rates, directly affecting the latitude the nervous system has to select a given coordination strategy—and the necessary correlations in activations among muscles [72, 74].

The structure of the solution space, the latitude it affords, and the necessary correlations in muscle activations are all at the root of the study of muscle redundancy, muscle synergies, learning and adaptation, uncontrolled manifolds, etc. Importantly, these vectormaps of feasible activation ranges for submaximal forces motivate EMG studies to understand whether and how vertebrates actually make use of them (e.g. during learning and adaptation). This ties into the spatiotemporal exploration-exploitation of the null-space of a task. As discussed in detail elsewhere ([41] and references therein), traversing the solution manifold is likely an active spatio-temporal process where the neural controller can choose to inhabit a particular region or subset of the solution space to meet the requirements of the task. Thus, the nature of motor control may be more related to exploring and learning the feasible set of activations, and using memory and improvements via fast and slow gradients, than the current thinking emphasizing optimization to find unique solutions. A subtle point is that muscle synergies will naturally be detected from such explorations-exploitations of a well-structured feasible activation space. Our hope is that these techniques may help the evolution of this [74, 133, 17, 132] and other debates in motor control.

While questions remain about which muscles are necessary or optional to produce submaximal force output for a given set of constraints and why [2], they can only be answered as we begin to add all spatio-temporal constraints [99, 38] for natural behavior in the real world [64, 79]—as opposed to tasks in the laboratory setting. But for now, we at least demonstrate that we have the tools to visualize and compare changes in

the structure of the FAS. In fact, for the case of maximal force output for which the activation levels are unique, we can already glean important lessons that motivate testable hypotheses (Figure 4, far Right). An example that comes to mind looking at the three muscles shown (and more available online), is that the interaction between limb mechanics and task constraints leads to irregular and complex levels of activation across 3-D directions of force production. This counters the widespread view that muscles are engaged in a manner consistent with spatially smooth cosine tuning functions [44]. Therefore, these tools begin to address the need for computational tools pointed out in [113, 74, 17] to characterize and explore the extent to which mechanical considerations determine the neural control of numerous muscles.

1.8   Muscle activation for fast everyday recreational and sports tasks

The velocities of individual muscle fibers, and how they are determined by the kinematics of a task, are a particular example of task constraints that have often been overlooked. We find the common recreational task of throwing a flying disc (and reasonably other similar tasks such as throwing a ball, etc.) invariably leads to muscle fiber velocities greater than c. 5 muscle fiber lengths per second (Figure 7). Such high concentric and eccentric muscle fiber velocities are thought to incapacitate active force production or lead to tearing injuries, respectively [160, 55]. We employed a process of elimination to systematically investigate our model and its parameters to give us confidence in our interpretation of the results. Intuitively, we can assume that the bone (segment lengths) and joint kinematics were obtained experimentally and are physiologically reasonable. The muscle fiber lengths and moment arms we considered in our study were obtained from published data [48, 51, 56, 90]. Due to the between subject variability, we applied a Monte Carlo analysis to consider a range of moment arm values for each muscle and still find high fiber velocities (Figure 7, bottom). While we do not show them, we find similar results in a Monte Carlo analysis of the muscle fiber lengths. Moreover, even though our model is limited in that it did not include the acceleration and deceleration phases of the movement, adding them could only increase muscle fiber velocities

we report. Likewise, assuming a less conservative total time for the movement would only exacerbate the high velocities we find. Despite this systematic Monte Carlo analysis, we still find muscle fiber velocities greater than 5 fiber lengths per second. Thus we are compelled to challenge the traditional understanding of the force-velocity properties of muscles and motivate future research in muscle mechanics: somehow, such high fiber velocities are likely present in everyday tasks do not lead a complete loss of force production capabilities in the concentric phase, or injury in the eccentric phase. This is not the first time we question the functional role of the force-velocity properties of muscles for everyday tasks [64].

Another fundamental result from these simulations is that they emphasize the need to study the temporal structure of muscle activation in the context of muscle redundancy [99, 38]. Consider Eq. 2 defining the over-determined physical relationship between changes in joint angles and tendon excursions that drive changes in muscle fiber lengths. This relationship defines the obligatory correlations among tendon excursions where a sequence of (a few) joint angles uniquely and completely determines the excursions of all (numerous) musculotendons. This is the opposite of muscle redundancy as there is a single and unique set of tendon excursions that can satisfy the kinematics of a given movement. This begs the question of how the nervous system coordinates eccentric and concentric contractions to produce such fast movements. If, for any reason, any muscle fails to lengthen (i.e., contract eccentrically) to satisfy the rotations of the joints it crosses, the desired motion will, at best, be disrupted, or at worst, the limb will freeze.

What inhibits stretch reflexes to allow such coordinated eccentric contractions? Alpha-gamma co-activation, reciprocal-inhibition, and gating of spindle afferent information are some of neural interactions thought to be necessary to modulate/inhibit stretch reflexes [45]. Thus the nervous system must issue neural commands, coordinated throughout the entire duration of the movement, to (i) alpha-motoneurons to produce the necessary joint torques as per the standard force-sharing motor control problem (e.g., [93, 24]); (ii) coordinate reciprocal-inhibition of alpha-motoneuron pools across shortening and lengthening muscles (e.g., [57]); (iii) inhibit the stretch reflex in muscles needing to undergo eccentric contractions (e.g., [161]); while (iv) satisfying the time constants of muscle excitation-contraction dynamics [160] to ensure the continuity of these neural commands as the motion progresses. This compounding of multiple spatial and temporal

constraints naturally leads to a shrinking of the set of feasible motor commands for natural movements (see above discussion and [64]).

In fact, clinicians have long been aware of how disorders of reflexes or the neural circuits of 'afferented muscles' lead to disruptions or failures of movements (for an overview see [101, 102]. We now propose that these so-called dystonias may in fact be a natural consequence of the nervous system failing to meet the stringent temporal demands on alpha-gamma neural drive for the eccentric and concentric contractions essential to smooth limb movement. This again supports the view that extant vertebrates have barely enough neural degrees of freedom for versatile real-world behavior [64, 79, 147, 72, 74] as the muscle activations to produce smooth movements is likely not redundant, or at the very least not as redundant as currently thought.

One last comment is on the over-determined nature of producing the necessary muscle excursions for a limb movement. As mentioned above, over-determined systems either have one unique solution (if it exists), or no solution at all. When no solution exists, a practical alternative is found by violating some or all constraints as in the method of least squares for a set of equations in which there are more equations than unknowns. This may actually begin to explain why muscles and tendons have non-trivial amounts of passive elasticity—to provide tolerance to errors in the neural control of their excursions when eccentric and concentric contractions are not controlled accurately enough by the CNS. From the engineering perspective, such elasticity complicates control as it adds delays and internal actuator dynamics, and reduces actuator bandwidth. But in the case of biological tendon-driven limbs, this built-in tolerance to excursion errors may be a critical compliment to, and enabler of, the neural control of smooth movements.

1.9   Acknowledgments
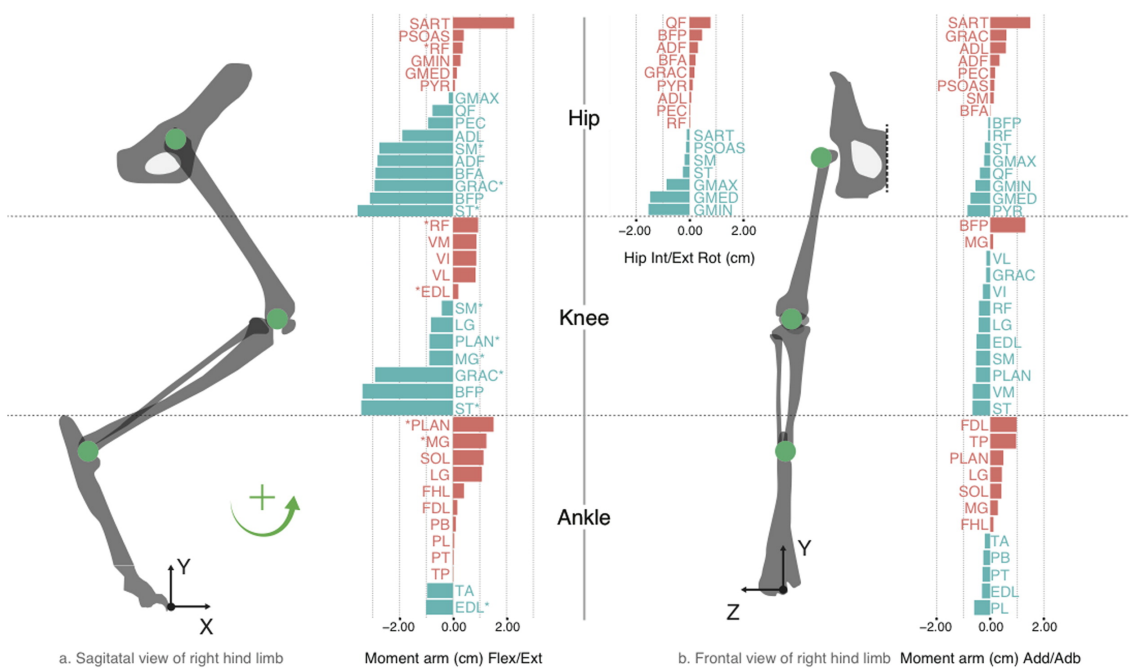
Figure 1.1: Bone lengths, joint axes of rotation, and moment arm matrix for the species average cat hindlimb model, in cm. Positive values are shown in red and negative values in blue, as per the right-hand-rule.
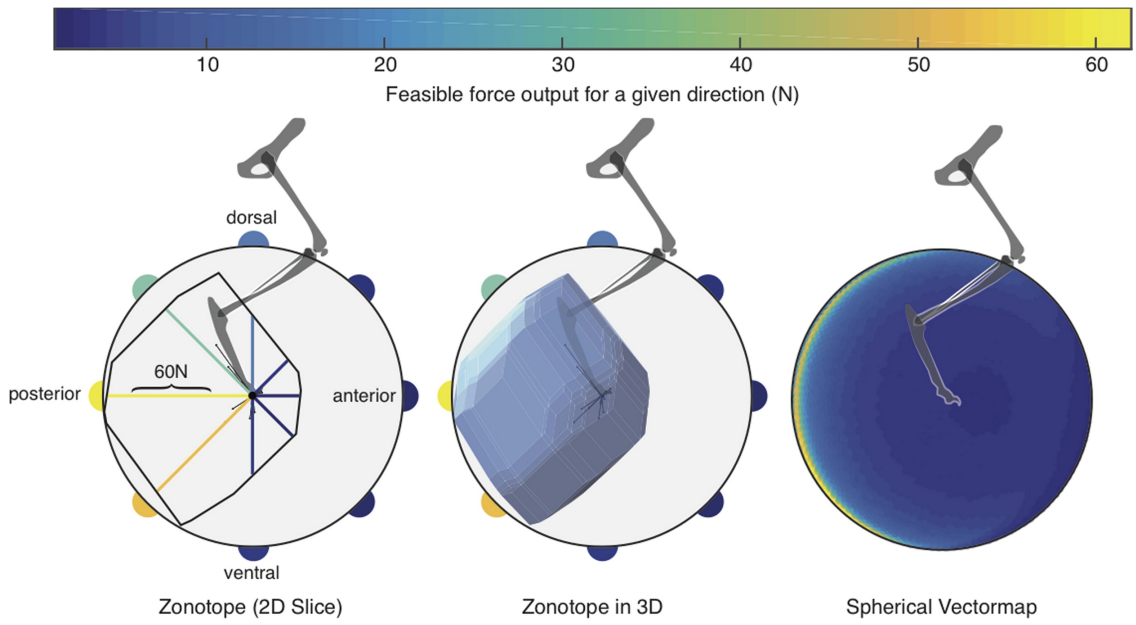
Figure 1.2: **Left:** The polygon of the 2-D feasible force set in the sagittal plane. The color-coded vectormapping of radial lines indicate the magnitude of the maximal feasible force along that direction, then vectormapped onto the perimeter of the circle surrounding the FFS. The very thin lines emanating from the origin are the lines of action of each of the 31 muscles. **Center:** the polyhedron of the 3-D FFS, again with the vectormapping of force magnitude values onto a circle in the sagittal plane. **Right:** The color-coded vectormapping onto the surface of a sphere indicating the maximal feasible force in every direction in 3-D. Note the FFS is rather flat on the sagittal plane, but elongated towards the posterior direction. All data are for the cat called Birdy in [113].
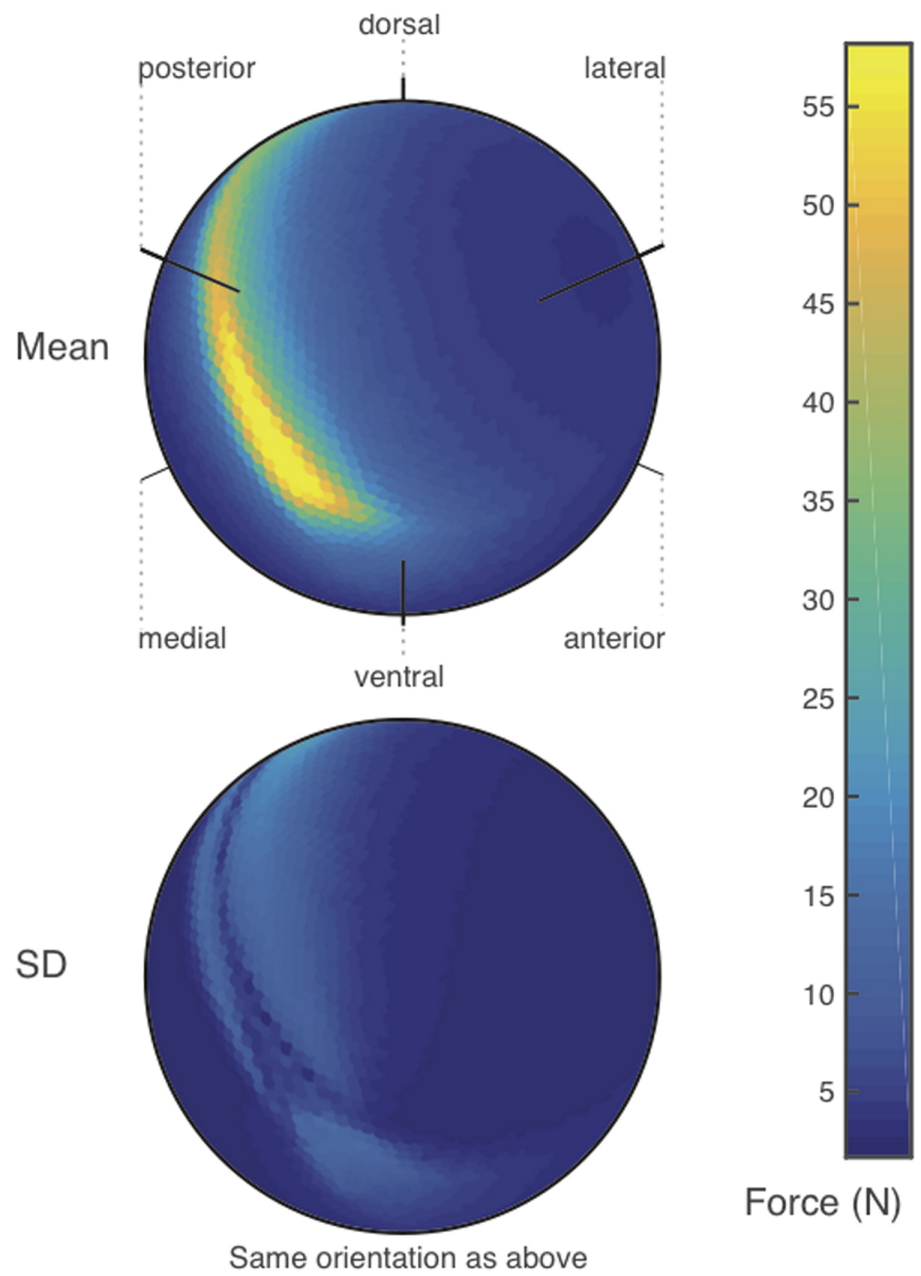
Figure 1.3: **Top:** Vectormap of the average of maximal feasible force across all sampled output vectors in three feline hindlimbs. **Bottom:** A vectormap displaying regions of the feasible force space that have higher standard deviation across three cat hindlimbs. Force in Newtons represented by color scale.
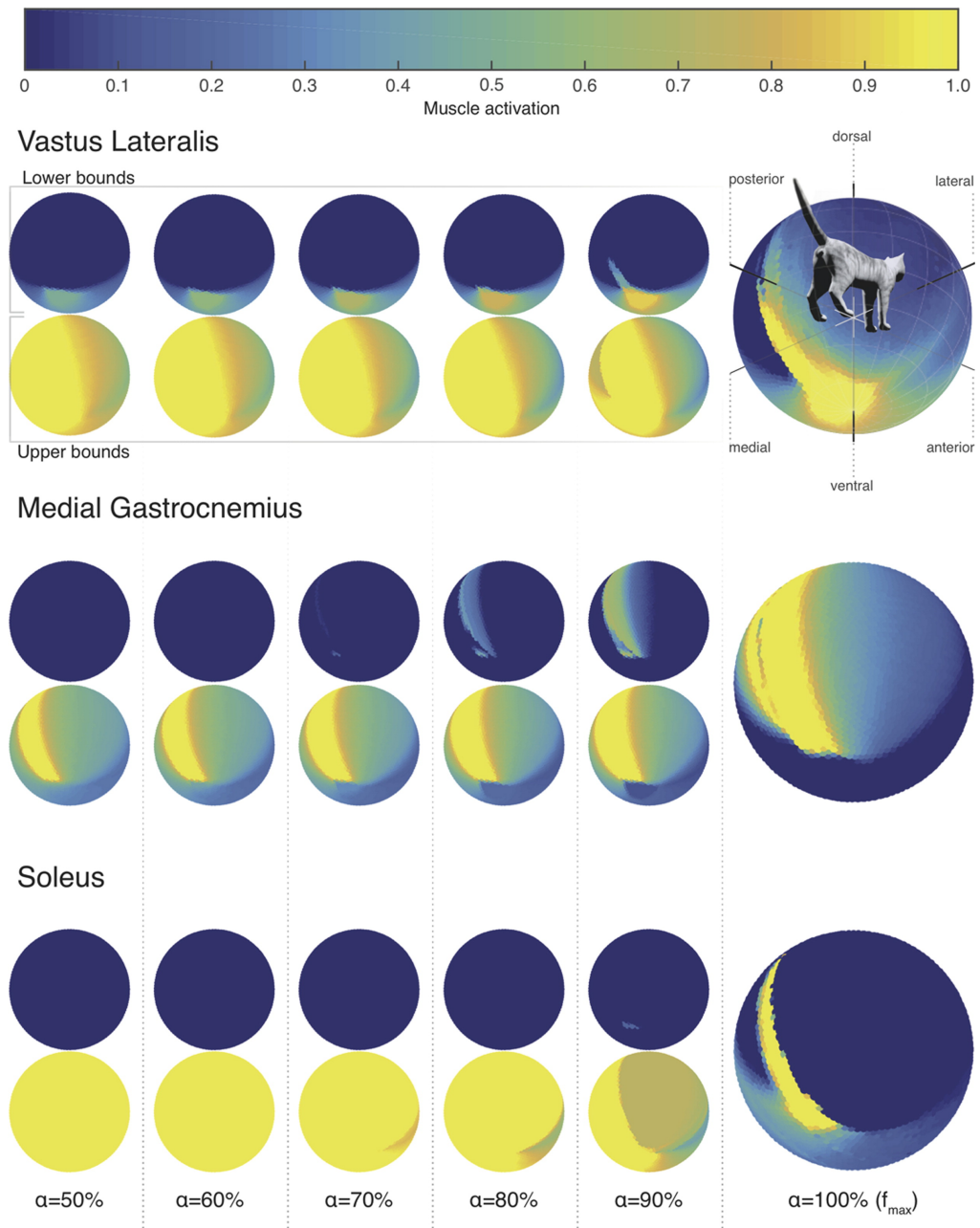
Figure 1.4: Structure of the feasible activation set for three muscles. The large vectormaps on the far Right show their unique activation level for maximal force output in every 3-D direction. Because multiple activation levels can produce submaximal forces, the small vectormaps to the Left show the lower and upper bounds of those feasible activation levels for force magnitudes (a) gradually increasing from 50% of maximal in every 3-D direction.
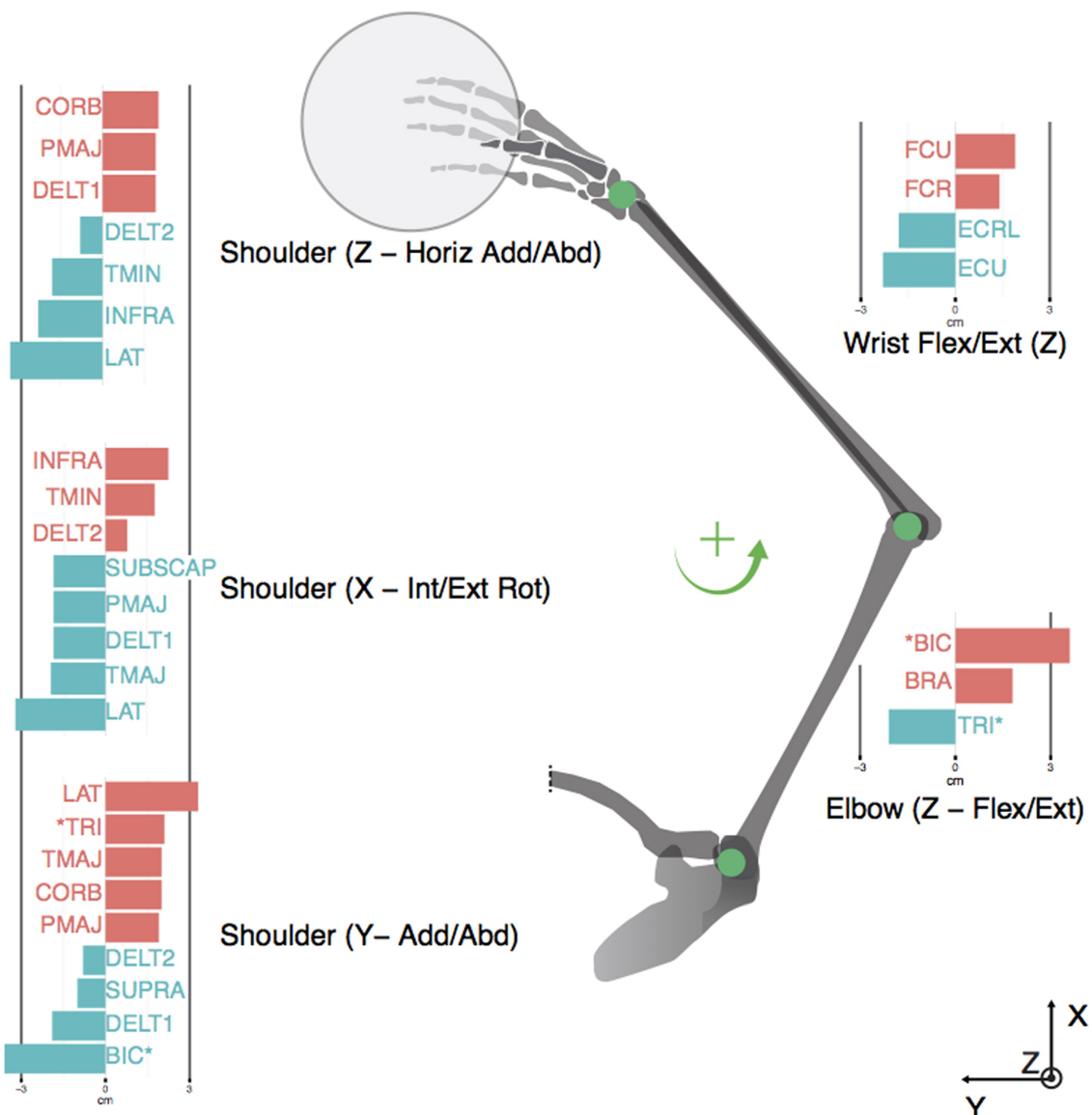
Figure 1.5: Moment arm values for human arm model. The moment arms from the 17 muscles considered in this model and their associations with the five DoFs are illustrated, in cm. The moment arms are grouped by DoF and are shown below the associated joint. Positive values are shown in red and negative values in blue.
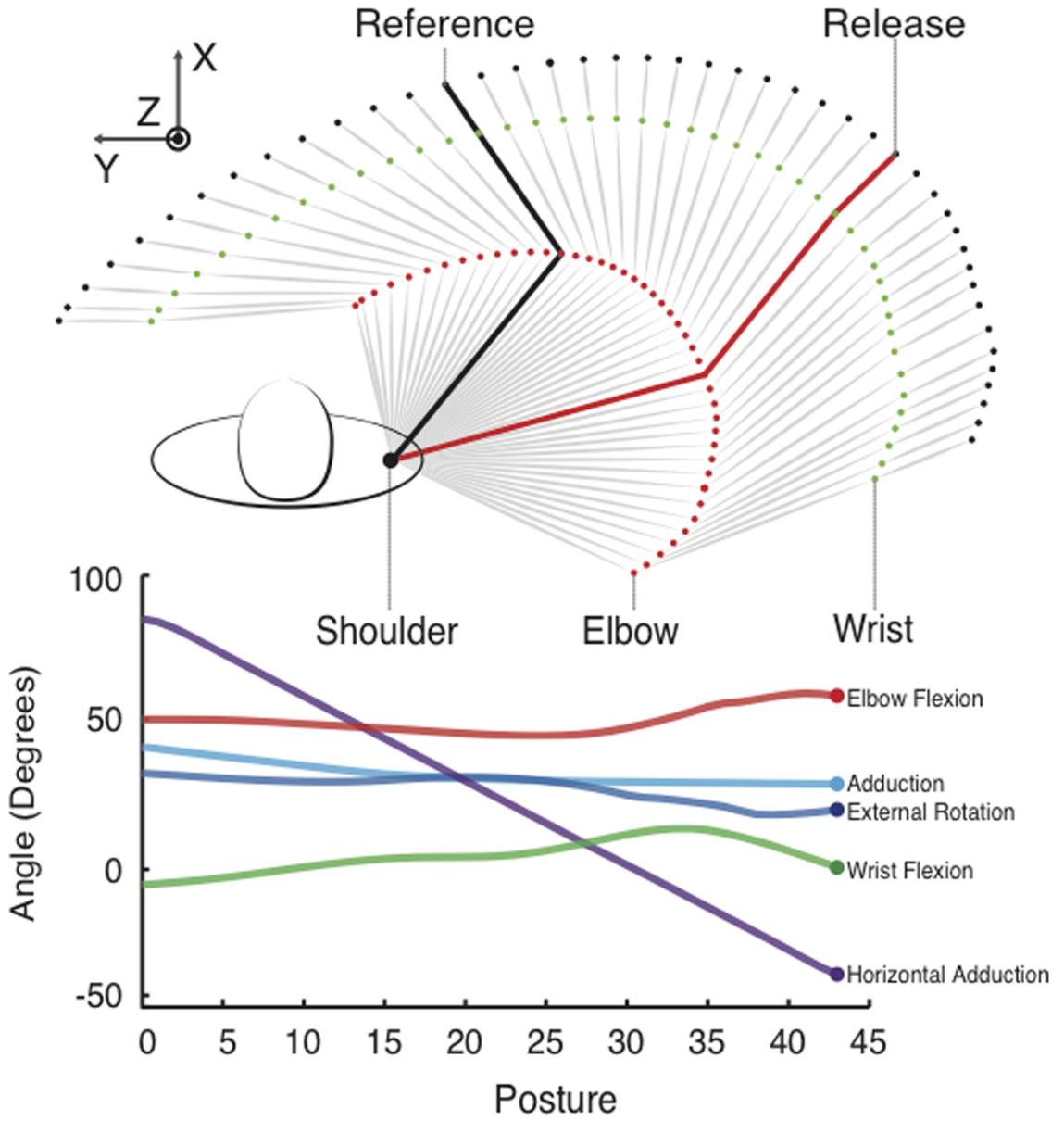
Figure 1.6: Top view of the 3-D human arm model. This figure illustrates the initiation of forward motion through follow-through of the flying disc throw. The reference posture is shown in black and the release point in the throw is shown in red. The interpolated joint angles for the 45 postures describing this motion, obtained from [58], are shown in the bottom panel.
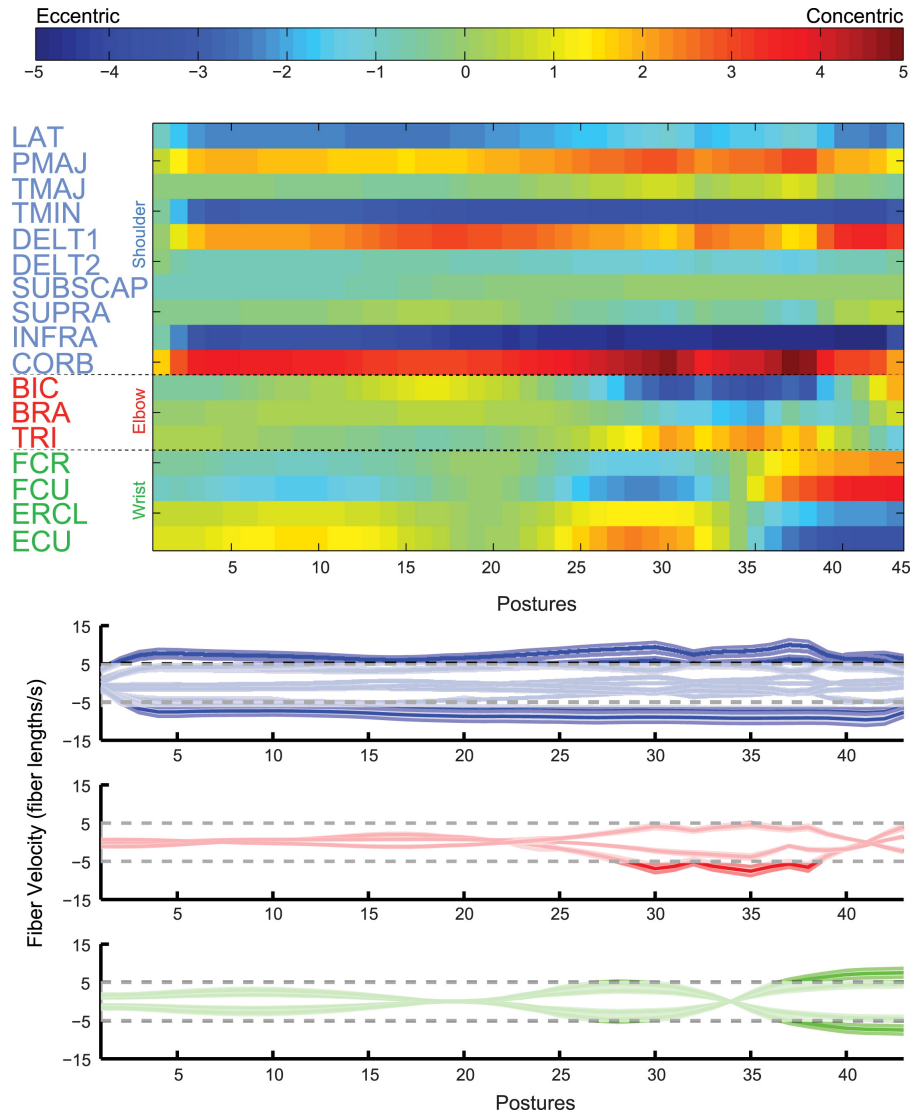
Figure 1.7: Normalized instantaneous fiber velocities during the throw for the nominal model. **Top:** The muscles are listed on the y-axis and the 45 postures making up the throw are shown on the x-axis. Excessive muscle velocities are shown in red (shortening) and blue (lengthening). **Bottom:** The same data are illustrated with individual traces for each muscle that show the fiber velocity. Muscles controlling the shoulder, elbow, and wrist are illustrated in blue, red, and green, respectively. Instantaneous fiber velocity is given on the y-axis and the postures during the throw are on the x-axis. Regions of the traces outside of the horizontal dashed lines indicate excessive muscle velocities. In both figures, the release point of the throw is indicated with a vertical dashed line.

Chapter 2

Structure of the set of feasible neural commands for complex motor tasks

Valero-Cuevas FJ[1], Cohn BA[3], Szedlák M[4], Fukuda K[4] and Gärtner B[4]

[1]Department of Biomedical Engineering, University of Southern California, Los Angeles, CA [2]Division of Biokinesiology and Physical Therapy, University of Southern California, Los Angeles, CA [3]Department of Computer Science, University of Southern California, Los Angeles, CA [4]Swiss Federal Institute of Technology-Zurich, Zurich, Switzerland

2.1 Abstract

The brain must select its control strategies among an infinite set of possibilities; researchers believe that it must be solving an optimization problem. While this set of feasible solutions is infinite and lies in high dimensions, it is bounded by kinematic, neuromuscular, and anatomical constraints, within which the brain must select optimal solutions. That is, the set of feasible activations is well structured. However, to date there is no method to describe and quantify the structure of these high-dimensional solution spaces. Bounding boxes or dimensionality reduction algorithms do not capture their detailed structure. We present a novel approach based on the well-known Hit-and-Run algorithm in computational geometry to extract the structure of the feasible activations capable of producing 50% of maximal fingertip force in a specific

direction. We use a realistic model of a human index finger with 7 muscles, and 4 DOFs. For a given static force vector at the endpoint, the feasible activation space is a 3D convex polytope, embedded in the 7D unit cube. It is known that explicitly computing the volume of this polytope can become too computationally complex in many instances. However, our algorithm was able to sample $1,000,000$ uniform at random points from the feasible activation space. The computed distribution of activation across muscles sheds light onto the structure of these solution spaces—rather than simply exploring their maximal and minimal values. Although this paper presents a 7 dimensional case of the index finger, our methods extend to systems with at least 40 muscles. This will allow our motor control community to understand the distributions of feasible muscle activations, providing important contextual information into learning, optimization and adaptation of motor patterns in future research.

2.1.0.1 Author Contribution

In a collaboration with ETH, this work represented the seminal work that led to the introduction of Feasibility Theory, and I contributed all code, analyses, while MS and BG, and FV contributed to the theoretical implementations and the neuromuscular implications, respectively.

2.2   Introduction

Muscle redundancy is the term used to describe the underdetermined nature of neural control of musculature. The classical notion of muscle redundancy proposes that, faced with an infinite number of possible muscle activation patterns for a given task, the nervous system uses optimization to select a specific solution. Here, each of the N muscles represents a dimension of control, and a muscle activation pattern is a point in $[0, 1]^N$ [144]. Thus researchers often seek to infer the optimization approach and the cost functions the nervous system likely uses to find points in activation space to produce natural behavior [23, 92, 106, 129, 32, 54].

Implicit in these optimization procedures is the notion that there exists a well structured set of feasible solutions. Thus several of us have focused on describing and understanding those high-dimensional subspaces embedded in $[0,1]^N$ [73, 75, 110, 144, 62].

For the case of muscle redundancy for submaximal and static force production with a limb, the problem is phrased as one of computational geometry: find the convex polytope of all feasible muscle activations given the mechanics of the limb and the constrains of the task [9, 144, 139, 62]. This convex polytope is called the *feasible activation set*. To date, the structure of this high-dimensional polytope is inferred by its bounding box [73, 110, 62]. But the bounding box of a convex polytope will always exclude the details of its shape. Empirical dimensionality-reduction methods have also been used to calculate basis vectors for such subspaces [27, 33, 69]. But those basis vectors only provide a description of the dimension, orientation, and aspect ratio of the polytope, but not of its boundaries or internal structure.

Here we present a novel application of the well-known Hit-and-Run algorithm [109] to describe the internal structure of these high-dimensional feasible activation sets. We apply our technique to a schematic example with three muscles to describe the method, and then use a realistic model of an index finger with seven muscles and four joints [144].

2.3 Methods

2.3.1 Hit-and-Run algorithm

The boundaries of the convex polytope defining the feasible activation set are defined by the mechanics of the limb and the constraints of the task, as is described in Subsection 3.3.1. The goal of the Hit-and-Run algorithm is to uniformly sample a convex body [109]. In the case of a schematic tendon-driven limb with three muscles, the feasible activation space is the unit cube (as muscles can only be activated positively from 0 to a maximal normalized value of 1). As explained in [139], when task constraints are introduced to the system, the feasible activation set is further reduced; in this context, a task is a static force vector produced at the endpoint of the limb, which is represented as a set of inequality constraints. Thus

if this simple limb meets all constraints, the feasible activation set of the polygon P contains all feasible activations $\mathbf{a} \in \mathbb{R}^n$ that satisfy

$$\mathbf{f} = A\mathbf{a}, \mathbf{a} \in [0,1]^n,$$

where $\mathbf{f} \in \mathbb{R}^m$ is a fixed force vector, and $A = J^{-T}RF_o \in \mathbb{R}^{m \times n}$—where J, R, and F_o are the matrices of the Jacobian of the limb, the moment arms of the tendons, and the strengths of the muscles, respectively [144, 139]. P is bounded by the unit n-cube since all variables a_i, $i \in [n]$ are bounded by 0 and 1 from below, above respectively. Consider the following 1×3 fabricated example, where the task is a 1N unidimensional force.

$$1 = \frac{10}{3}a_1 - \frac{53}{15}a_2 + 2a_3$$

$$a_1, a_2, a_3 \in [0,1],$$

the set of feasible activations is given by the shaded set in Figure 1TODO.

The Hit-and-Run walk on P is defined as follows (it works analogously for any convex body).

1. Inner Point: Find a given starting point $\mathbf{p}$ of P (Figure 2.2a) .

2. Direction: Generate a random direction from $\mathbf{p}$ (uniformly at random over all directions) (Figure 2.2a).

3. Endpoints: Find the intersection points of the random direction with the edges of the polytope (Figure 2.2b).

4. New Point: Pick a point uniform at random along the line segment defined by the endpoints (Figure 2.2c).

5. Repeat from (a) the above steps with the new point as the starting point .

To find a starting point in

$$\mathbf{f} = A\mathbf{a}, \mathbf{a} \in [0,1]^n,$$
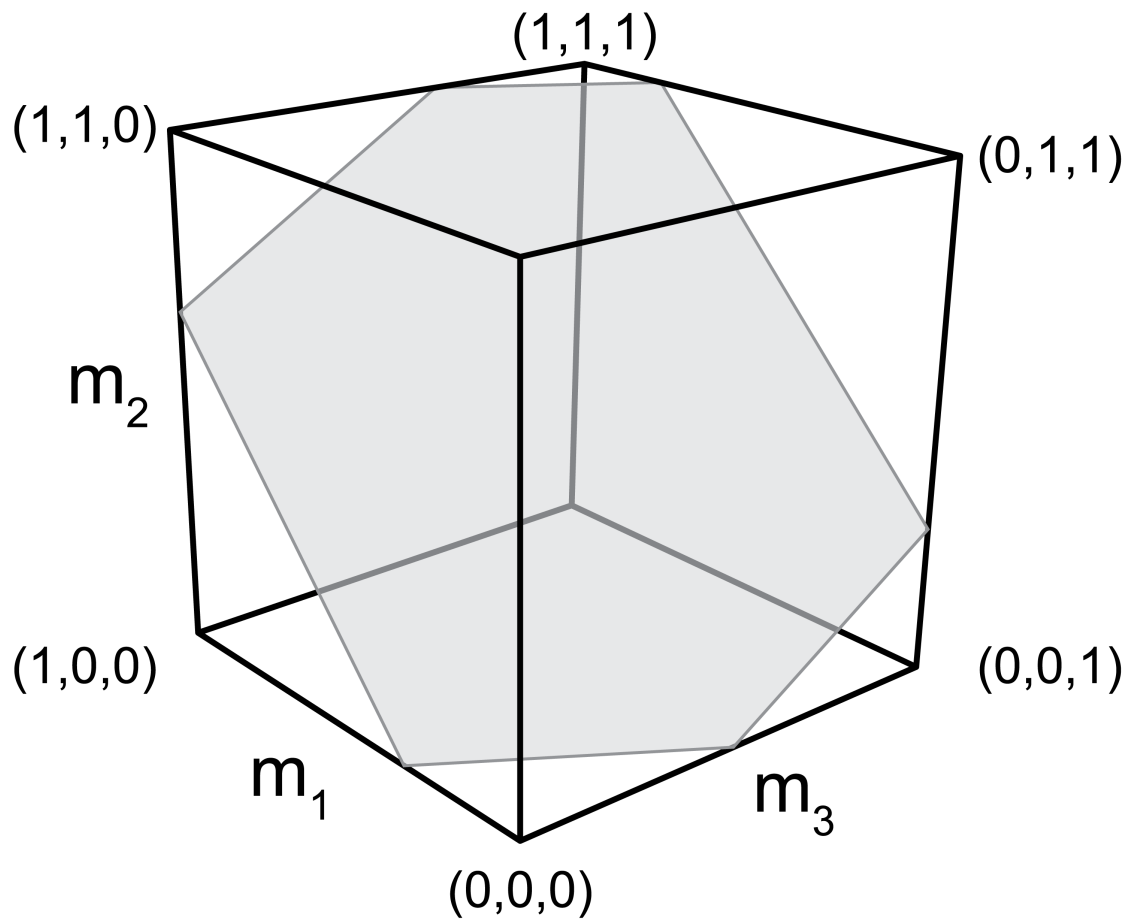
Figure 2.1: The feasible activation set for a three-muscle system meeting one functional constraint is a polygon in $\mathbb{R}^3$. Note that muscle activations are assumed to be bounded between 0 and 1.
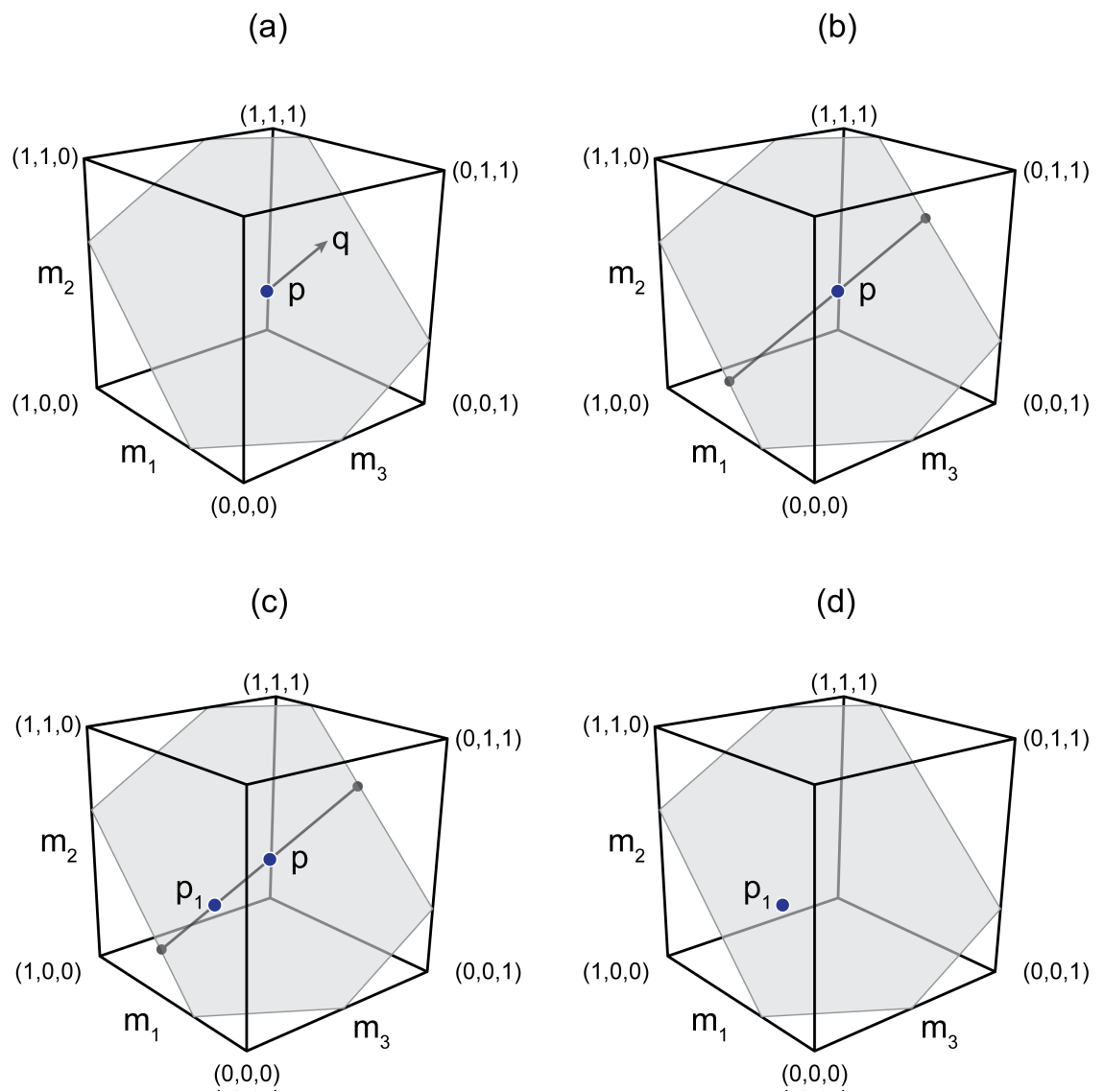
Figure 2.2: Graphical description of the Hit-and-Run algorithm.

we only need to find a feasible activation vector. For the Hit-and-Run algorithm to mix faster, we want the starting point to be centrally located within the polytope. We use the following standard trick with slack variables ε_i.

$$
\begin{aligned}
\text{maximize} \quad & \sum_{i=1}^{n} \varepsilon_i \\
\text{subject to} \quad \mathbf{f} \ &= \ A\mathbf{a} \\
a_i \ &\in \ [\varepsilon_i, 1 - \varepsilon_i], \quad \forall i \in \{1, \ldots, n\} \\
\varepsilon_i \ &\geq \ 0, \quad \forall i \in \{1, \ldots, n\}.
\end{aligned}
\tag{2.1}
$$

The recursive nature of the algorithm means that consecutive points are autocorrelated; it's important that each point sampled from the polytope is uniform at random, so we subset points separated by a number of iterations. For convex polygons in higher dimensions (over 40 dimensional), experimental results suggest that $\mathcal{O}(n)$ steps of the Hit-and-Run algorithm are sufficient. In particular Emiris and Fisikopoulos paper suggest that $(10 + \frac{10}{n})n$ steps are enough to converge upon the uniform distribution [43]. In the index finger model we executed the Hit-and-Run algorithm $1{,}000{,}000$ times, selecting only every 100th point.

2.3.2 Realistic index finger model

We used our published model in [144] to find matrix $A \in \mathbb{R}^{4 \times 7}$, where $\mathbf{a} \in \mathbb{R}^7$. The seven muscles are *flexor digitorum profundus* (FDP), *flexor digitorum superficialis* (FDS), *extensor indicis proprius* (EIP), *extensor digitorum communis* (EDC), *lumbrical* (LUM), *dorsal interosseous* (DI), and *palmar interosseous* (PI). The four degrees of freedom were ad-abduction, flexion-extension at the metacarpophalangeal joint, and flexion-extension at the proximal and distal interphalangeal joints. The force direction we simulated is in the palmar direction in the posture shown in Figure 2.3.
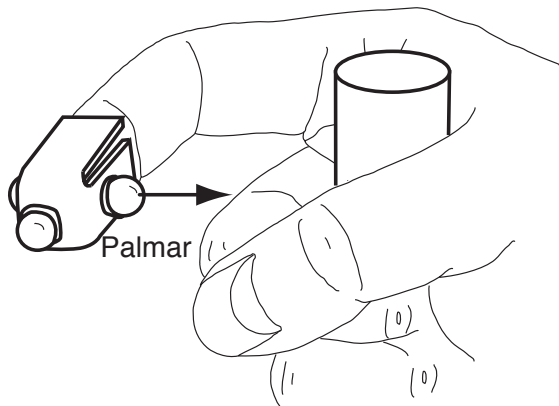
Figure 2.3: The index finger model simulated 50% of maximal force production in the palmar direction. Adapted from [144].

2.4 Results

Figure 2.4 shows the distributions of activations resulting from the solutions computed with Hit-and-Run sampling. This is the first time (to our knowledge) that the internal structure of the feasible activation set has been visualized for a sub-maximal force.

Notice that the lower and upper bounds of the activations (i.e., the dashed lines indicating their bounding box), are unhelpful in determining the actual density distribution of feasible activations. The activation needed for the maximal force output (thick gray line) is very often not the mode of the activations at 50% of output. It's important to note that these histograms are unidimensional- they do not illustrate the between-muscle associations.

2.5 Discussion

Our results and methodology raise the following ideas:

- The Hit-and-Run algorithm can explore the feasible activation space for a realistic 7-muscle finger in a way that is computationally tractable.
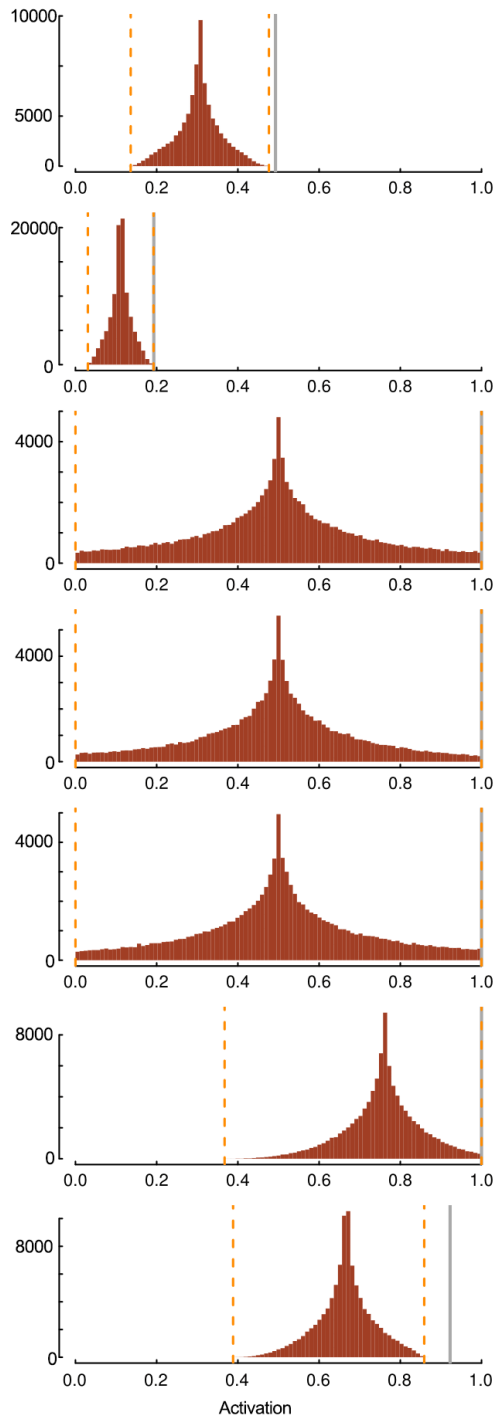
Figure 2.4: We show one histogram for each muscle of the index finger to illustrate how the muscle is used across all feasible solutions. For this set of distributions, the task was 50% of maximal force output in the palmar direction. Muscles are *FDP*, *FDS*, *EIP*, *EDC*, *LUM*, *DI*, and *PI* are shown in that order from top to bottom. The orange dotted lines are the lower and upper bounds of activation.

- For some muscles, we find that the bounding box exceptionally misconstrues the internal structure of the feasible activation set.

- The Hit-and-Run algorithm is cost-agnostic in the sense that no cost function is needed to predict the distribution of muscle activation patterns. Therefore, we can provide spatial context to where 'optimal' solutions lie within the solution space; this approach can be used to explore the consequences of different cost functions.

- The distribution of muscle activations may be intricately related to strong modes which critically affect the learning of motor tasks.

With the spatial context of the feasible activation space, we can explore the statistical tendencies of a musculoskeletal system, and better define the landscape upon which optimization occurs. This application of Hit-and-Run provides a tool to generate testable hypotheses of how coordination habits may come about, how they are learned, and how difficult or easy it is to break out of them.

Chapter 3

Feasibility Theory reconciles and informs alternative approaches to neuromuscular control

Brian A. Cohn [1], May Szedlák [2], Bernd Gärtner[2] and Francisco J. Valero-Cuevas [3,4]

3.0.0.1 Affiliations

[1]University of Southern California, Department of Computer Science, Los Angeles, CA. [2]ETH Zurich, Department of Theoretical Computer Science, Zurich, Switzerland.

[3]University of Southern California, Department of Biomedical Engineering, Los Angeles, CA.

[4]University of Southern California, Division of Biokinesiology and Physical Therapy, Los Angeles, CA.

3.1 Abstract

We present Feasibility Theory, a conceptual and computational framework to unify today's theories of neuromuscular control. We begin by describing how the musculoskeletal anatomy of the limb, the need to control individual tendons, and the physics of a motor task uniquely specify the family of all valid muscle activations that accomplish it (its 'feasible activation space'). For our example of producing static force with a finger driven by seven muscles, computational geometry characterizes—in a complete way—the structure of feasible activation spaces as 3-dimensional polytopes embedded in 7-D. The feasible activation

space for a given task is *the* landscape where all neuromuscular learning, control, and performance must occur. This approach unifies current theories of neuromuscular control because the structure of feasible activation spaces can be separately approximated as either low-dimensional basis functions (synergies), high-dimensional joint probability distributions (Bayesian priors), or fitness landscapes (to optimize cost functions).

3.1.0.1 Author Contribution

In a collaboration with ETH, this work expands upon the techniques from Chapter 2. I contributed all code, analyses, and simulations, MS and BG contributed to the theoretical equation implementations and the neuromuscular implications, and FV supported the deep analysis of neuromuscular implications of the results.
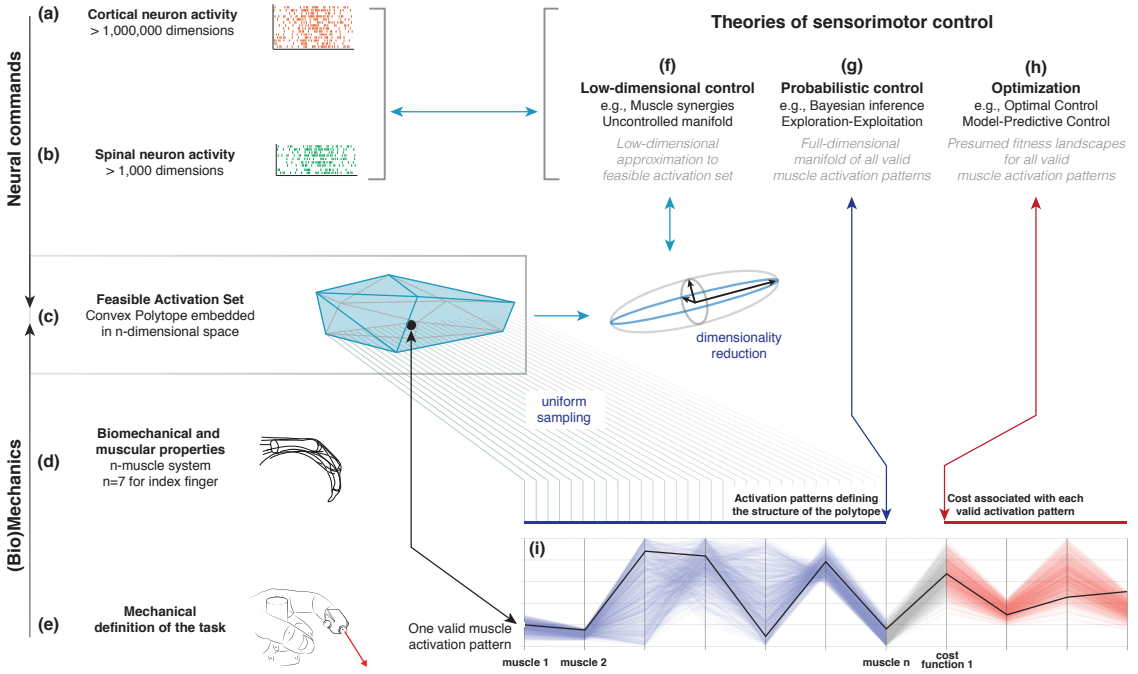
3.2 Introduction

How the nervous system selects specific levels of muscle activations (i.e. a muscle activation pattern) for a given motor task continues to be hotly debated. Some suggest the nervous system either combines low-dimensional synergies[75, 118, 18, 39, 96, 119, 3], learns probabilistic representations of valid muscle activation patterns[66, 67, 15, 100], or optimizes physiologically-tenable cost functions[23, 92, 106, 129, 32, 54]. At the core of this problem lies the nature of 'feasible activation spaces', and the computational challenge of describing and understanding their high-dimensional structure (for an overview, see[149]). A feasible activation space is the family of valid solutions (i.e. muscle activation patterns) that meet the mechanical constraints [1] of a given motor task. Fig. 3.1 illustrates these neuromechanical interactions that define the feasible activation space for a particular task.

The most the nervous system can do, therefore, is select and apply a specific muscle activation pattern from within the feasible activation space. This is because muscle activation patterns outside of this space are, by definition, inappropriate for the task. In fact, the feasible activation space defines the landscape

---

[1]Mechanical constraints is a formal way to call the physical demands, requirements, or characteristics of a given physical task.

Figure 3.1: **Emergence and interpretation of feasible activation spaces for a particular motor task.**
The descending motor command for a given task is issued by the motor cortex (a), which projects onto
inter-neurons and *alpha*-motor neuron pools in the spinal cord (b). The combined drive to all *alpha*-motor
neurons of a muscle can be considered its total muscle activation level (a value between 0 and 1). If we
consider that muscles can, to a large extent, be controlled independently and in different ways, then the
overall motor command can be conceptualized as a multi-dimensional *muscle activation pattern* (i.e. a
point) in a high-dimensional *muscle activation space*[23, 116, 70, 144, 129] (c). For that muscle activation
pattern to be valid, it has to elicit muscle forces (d) capable of satisfying the mechanical constraints of
the task—in this case defining a well-directed sub-maximal fingertip force (e). Given the large number
of muscles in vertebrates, there can be muscle redundancy: where a given task can be accomplished with
a large number of valid muscle activation patterns. We propose that our novel ability to characterize the
high-dimensional structure of feasible activation spaces (i) allows to us to compare, contrast, and reconcile
today's three dominant approaches to muscle redundancy in sensorimotor control (f, g, h).

upon which all neuromuscular learning and performance must occur for that task. Studying neuromuscular control is, therefore, equivalent to studying how the nervous system finds, explores, inhabits, and exploits the contents and structure of feasible activation spaces[75, 118, 18, 47, 39, 96, 119].

But the 'curse of dimensionality'[12, 13, 9] makes it computationally challenging to calculate, describe, and understand the nature and structure of high-dimensional feasible activation spaces[142, 23, 116, 70, 125, 104, 39]—even for an isolated human finger or cat leg generating everyday static forces[75, 62, 149, 110]. This is due to the computational complexity of algorithms to map the geometric details of objects embedded in high dimensions [46, 109, 83].

Current theories of neuromuscular control[2] are alternative responses to overcome the curse of dimensionality in this context. These alternative approaches, however, are seldom combined and often the insights from one realm are not readily applicable to the others. Here we emphasize how the mechanics of the body and the physics of the task constitute the common ground for all theories.

We now propose 'Feasibility Theory', which is a conceptual framework to characterize feasible activation spaces in detail. While prior work has described *how* to find such feasible activation spaces for static force production[144, 75, 157, 145, 85], we now explain *why* the structure of a feasible activation space can be approximated with low-dimensional synergies and probability distribution functions, and can be associated with multiple fitness landscapes over which to optimize.

3.3 Methods

In the case of the seven muscles of the human index finger producing static fingertip force, we show that the family of feasible commands, the feasible activation space, is a 3-dimensional polytope embedded in 7-dimensional muscle activation space [144]. A 'polytope' is the formal name for bounded polyhedra in dimensions higher than three. With 4 task constraints applied to 7 muscles, the result is a 3-dimensional polytope embedded in the 7-dimensional muscle activation space. By construction of anatomy, producing

---

[2]Neuromuscular control is variously referred to as neural, motor, sensorimotor, etc. control.

static force with a fixed posture naturally leads to a relationship between muscle forces and endpoint torques. The linear constraint equations that define this relationship (and in parallel the polytope that arises from the constraints) accurately represent the set of feasible motor commands [144, 149, 110]. Our computational approach hinges on the efficient sampling and complete representation of the geometric structure of high-dimensional polytopes, which fully characterizes the family of all valid muscle activation patterns—each of which solves the same task. By definition, this polytope is the null space of the task.

The methods to obtain feasible activation spaces for 'tendon-driven' limbs are described in detail in the textbook *Fundamentals of Neuromechanics* and references therein[149]. This tendon-driven approach explicitly and distinctly avoids the conceptual approach to calculate net torques at each joint. Rather, it emphasizes studying the individual actions of all muscles at all levels of analysis, from their neural activation to their contributions to fingertip force. We describe them briefly here.

Consider a tendon-driven limb, such as a finger, with n independently controllable muscles, where we define the neural command to each muscle as a positive value of activation between 0 (no activation) and 1 (maximal activation), where a value of 1 would produce the maximum possible tendon force for that muscle. We do not differentiate between concentric or eccentric contraction—we define muscle activation as the net static tendon tension, normalized by the maximum tendon tension possible by that muscle. We can then visualize the set of all feasible neural commands (i.e. all possible muscle activation patterns) as the points contained in a positive n-dimensional cube with sides of length equal to 1. A specific muscle activation pattern is a *point* (i.e. an n-dimensional vector **a**) in this n-dimensional cube[23, 116, 70, 144]. Now consider a specific task, such as producing a vector of static force with the fingertip, as when holding an object. Clearly, not all muscle activation patterns inside the n-dimensional cube can produce that desired static fingertip force vector: bone lengths, kinematic degrees of freedon, anatomical routing, posture, and muscle strength inequities define the subset of points in the n-cube which produce a fingertip force vector of a specific magnitude and direction. As described in[23, 116, 70, 149] the musculoskeletal anatomy of the limb, the need to control individual tendons, and the physics of a motor task uniquely specify a polytope embedded in $\mathbb{R}^n$ (i.e. the feasible activation space). This polytope contains the family of (potentially

infinite) valid muscle activation patterns that can produce this static force production task. However, these valid muscle coordination patterns are not arbitrarily different because, by construction, the geometric structure of the polytope that contains them defines strict spatial correlations among them[75].

System of linear equations to simulate static force production by a tendon-driven system

Consider producing a vector of static force with the endpoint of the limb in a given posture. The constraints that define that task (i.e. the direction and magnitude of the force vector at the endpoint) are linear equations[149] that come from the mapping between neural activation of individual muscles to static endpoint forces and torques the limb can produce. This mapping is linearly modeled by the equation

$$
\begin{pmatrix} f_x \\ f_y \\ f_z \\ \tau_x \\ \tau_y \\ \tau_z \end{pmatrix} = \mathbf{w} = H\mathbf{a} = H \begin{pmatrix} a_1 \\ a_2 \\ a_3 \\ ... \\ a_n \end{pmatrix}, \mathbf{a} \in [0,1]^n \tag{3.1}
$$

where H is the matrix of linear constraints defined by the musculoskeletal anatomy of the limb[62], $\mathbf{a}$ is the input vector of n muscle activations, and $\mathbf{f} \in \mathbb{R}^m$ is the m-dimensional limb output 'wrench' (i.e. the forces and torques the finger can produce at the endpoint).

The output wrench, w, is at most 6-dimensional (i.e. 3 forces and 3 torques) depending on the number of kinematic degrees of freedom of the limb, and usually $m < n$ because limbs have more muscles than kinematic degrees of freedom[149]. Muscles can only pull, so elements of $\mathbf{a}$ cannot be negative, and are capped at 1 (i.e. 100% of maximal muscle activation).

What are the muscle coordination patterns that produce a given task? As explained in[149], the task of producing a static fingertip force vector is defined by specifying the desired values for the elements of the endpoint forces and torques of $\mathbf{w}$. Each value yields a constraint equation, which in turn defines a

hyperplane of dimension $n - 1$, and their combination defines the task completely. The *feasible activation space* of the task, if it is well posed[25], is defined by the points **a** that lie within the n-cube and at the intersection of all constraint hyperplanes.

Geometrically speaking, the feasible activation space is a $(n - m)$-dimensional convex polytope P embedded in $\mathbb{R}^n$ that contains all n-dimensional muscle coordination patterns (i.e. points **a**) that satisfy all constraints, and therefore can produce the task. Increasing task specificity by adding more constraints naturally decreases the dimensionality and changes the size and shape of the feasible activation space[70, 110, 61].

The Hit-and-Run algorithm uniformly samples from feasible activation spaces

Calculating the geometric properties of convex polytopes in high dimensions is computationally challenging. Taking the generalized concept of an n-dimensional volume as an example of a geometric property of interest, the exact volume computations for n-dimensional polytopes is known to be tractable only in a polynomial amount of time (i.e. #P-hard)[41]. Currently available volume algorithms can only handle polytopes embedded in small dimensions like 10 or slightly more[21]. Studying vertebrate limbs in general, however, can require including several dozen muscles, such as our studies of a 17-muscle human arm and a 31-muscle cat hindlimb model[62]; and other models have over 40 muscles of the human lower limb [8, 75, 52, 36].

Similar difficulties arise when computing other geometric properties such as the shape and aspect ratio of P in high dimensions. We and others have described polytopes P by their bounding box (i.e. the range of values in every dimension)[110, 73], but that singularly overestimates the shape and volume of the feasible activation space as discussed in[62]. Consider a 3-muscle system with only one constraint, producing a 2-dimensional polygon as the feasible solution space. The bounding box of the polygon has a volume—even though a plane has zero volume—, and can be almost as large as the positive unit cube itself. Similar problems arise in the interpretation of the inscribed and circumscribed ball[60].

We applied the Hit-and-Run method to sample points from the feasible activation space. We have presented a detailed explanation of the Theory (In Chapter 9 of [149]), and have justified the utility of this method on tendon-driven models of the index finger [145]. This complete probabilistic method describes the structure of feasible activation spaces P with a set of uniformly-at-random muscle activation patterns that produce the same wrench. This enables us to derive descriptive statistics, histograms, and point densities of the set of valid muscle activation patterns $\mathbf{a}$ uniformly sampled from the polytope. To do so, we use the Hit-and-Run method.

This approach can scale up to ∼40 dimensions (i.e. limbs with ∼40 independent muscles). This suffices to study extant vertebrate limbs, and thus compare, contrast, combine—and reconcile—today's three dominant approaches to neuromuscular control.

3.3.1 Example of a tendon-driven system

Realistic 3-D model of a 7-muscle human index finger We applied this methodology to our published model of an index finger for static fingertip force production. The model is described in detail elsewhere[146]. Briefly, the input to the model is a 7-D muscle activation pattern $\mathbf{a}$, and the output is a 4-D wrench $\mathbf{w}$ (i.e. static forces and torques) at the fingertip:

$$\mathbf{w} = H\mathbf{a} \tag{3.2}$$

$$H = J^{-T}RF_o, H \in \mathbb{R}^{4 \times 7} \tag{3.3}$$

where

$$\mathbf{a} = \begin{pmatrix} a_{FDP} \\ a_{FDS} \\ a_{EIP} \\ a_{EDC} \\ a_{LUM} \\ a_{DI} \\ a_{PI} \end{pmatrix} \tag{3.4}$$

In Cartesian coordinates, the 4-D output wrench corresponds to the anatomical directions shown in Fig. 3.1e.

$$\mathbf{w} = \begin{pmatrix} f_x \\ f_y \\ f_z \\ \tau_x \end{pmatrix} = \begin{pmatrix} f_{radial} \\ f_{distal} \\ f_{palmar} \\ \tau_{radial} \end{pmatrix} \tag{3.5}$$

The biomechanical model H includes three serial links articulated by four kinematic degrees of freedom (ad-abduction, flexion-extension at the metacarpophalangeal joint, and flexion-extension at the proximal and distal interphalangeal joints). The action of each of the seven muscles (FDP: *flexor digitorum profundus*, FDS: *flexor digitorum superficialis*, EIP: *extensor indicis proprius*, EDC: *extensor digitorum communis*, LUM: *lumbrical*, DI: *dorsal interosseous*, and PI: *palmar interosseous*) on each joint to produce torque is given by the moment arm matrix $R \in \mathbb{R}^{4 \times 7}$. Lastly, $J \in \mathbb{R}^{4 \times 4}$ and $F_0 \in \mathbb{R}^{7 \times 7}$ are the Jacobian of the fingertip with 4 kinematic degrees of freedom, and the diagonal matrix containing the maximal strengths of the seven muscles, respectively[149, 138]. The finger posture was defined to be $0°$ ad-abduction and $45°$ flexion at the metacarpophalangeal joint, and $45°$ and $10°$ flexion, respectively, at the proximal and distal interphalangeal joints.

Feasible activation space for a static fingertip force task   Our goal is to find the family of all feasible muscle activation patterns that can produce a given task. In particular, the task we explored is producing various magnitudes of a submaximal static force in the distal direction f_{distal} — in the absence of any τ_{radial}, shown in Fig. 3.1e. Therefore the feasible activation space is a polytope P in 7-dimensional activation space that meets the following *four* linear constraints in **a**[144, 149, 138]

$$f_{radial} = \qquad\qquad 0 \qquad\qquad\qquad\qquad (3.6)$$

$$f_{distal} = \quad \textit{desired magnitude as \% of maximal} \qquad\qquad (3.7)$$

$$f_{palmar} = \qquad\qquad 0 \qquad\qquad\qquad\qquad (3.8)$$

$$\tau_{palmar} = \qquad\qquad 0 \qquad\qquad\qquad\qquad (3.9)$$

These four constraints on the static output of the finger yield a 3-dimensional (i.e. $7-4=3$) polytope P embedded in 7-dimensional activation space. For details on how to create such models, apply task constraints and find such polytopes via vertex enumeration methods, see[149].

For the index finger model used in this paper, the published maximal feasible force in the distal direction is 28.81 Newtons. We defined the normalized desired distal task intensity as a value ranging between 0 and 1, i.e. each submaximal force can be produced by any of the points contained in its corresponding feasible activation space. For the production of a maximal force, the feasible activation space shrinks to a single point[116, 23, 25, 138].

3.3.2   Analysis of feasible activation spaces

Parallel coordinate visualization   For us to understand the structure of the feasible activation space, we aim to visualize the data. If we had a simple model with only three muscles (and one task force dimension), we could plot the feasible activation space as a plane within a 3D cube, as illustrated in Fig. 3.2a. However, in our model, we have seven muscles. In our 3D reality, we cannot create a 7D scatter plot to highlight

45

how muscle activation patterns are spatially located across the muscle dimensions, so we must project the data in a different way.

Parallel coordinates are a common graphical approach to visualize interactions among high-dimensional data [10, 68]. To build familiarity with this visualization method, consider the results of a simple 3-dimensional (3-muscle) toy example shown in Fig. 3.2a. This is the dimensionality of a finger with only 3 muscles, aiming to create a unidimensional pressing force. We begin by drawing n parallel vertical lines for each of the dimensions n (i.e. 3 muscles). With the axis limits of each line set between 0 and 1 (at the bottom and top of the plot, respectively), each muscle activation pattern (Fig. 3.2a) is then represented by a zig-zag line that connects to the coordinates between 0 and 1 on each axis, as shown in Fig. 3.2b. The blue zig-zag line that is connected at the top of m_1 in Fig. 3.2b represents the muscle activation point equal to $(m_1 = 0.8, m_2 = 0.9, m_3 = 0.4)$. You can see its corresponding location in the 3D cube, mapped to the parallel coordinate zig-zag line (the gray dotted line connects the two representations of the muscle activation pattern).

Neural and metabolic cost functions As mentioned in the Introduction, the field of neuromuscular control has a long historical tradition of using optimization to find muscle activation patterns that minimize effort, which requires the (often contentious) definition of cost functions[116, 23, 92, 32]. Therefore, we used four representative cost functions to calculate the relative fitness of each of the muscle activation patterns sampled—in effect also calculating the fitness landscape across all possible solutions. The cost functions are defined at the level of neural effort (L_1, and L_2 norms, representing the normalized sum of descending neural α-drive to the motor neuron pools); and at the level of metabolic cost, thought to be approximated by neural drive weighted by the strength of each muscle (L_1^w and L_2^w norms)[92, 32].

To visualize the costs associated with each valid muscle coordination pattern, we simply added three vertical lines at the far right of the parallel coordinates plot, one for each of the three cost functions, Fig. 3.2c. The variables a_i and F_{0i} represent the activation of the ith muscle in a given muscle activation pattern, and the maximal strength of each muscle[92, 32]. Maximal muscle strengths are approximated

by the multiplying each muscle's physiological cross-sectional area, in cm^2, by the maximal active muscle stress of mammalian muscle, 35 N/cm^2[159]. These four cost functions are but four examples from the literature; an investigator is free to use this visualization of the feasible activation space with any cost function deemed relevant to their study.

Histograms of the activation level of each muscle across all valid solutions Muscle-by-muscle histograms are another straightforward way to visualize the many points sampled from the convex polytope. Histograms are particularly helpful because they illustrate the structure of the space of all feasible activations, allowing us to see which muscle activation patterns are on the edge of the space, which solutions exist in the middle of the space, and how the bounds of the space and the distribution change across different tasks (in this case, as the task force increases). They visualize the relative number of solutions (i.e. density of solutions) that required a particular level of activation from a particular muscle within its range of $[0, 1]$. In addition, the upper and lower bounds of the histograms show, in fact, the size of the side of the bounding box of the polytope in every dimension (i.e. for each independently controlled muscle).

Dimensionality reduction Investigators have repeatedly reported that electromyographical signals (i.e, experimental estimates of muscle activation patterns) tend to exhibit strong correlations with one another. In these experimental descriptions of dimensionality reduction of neuromuscular control, only few independent functions—sometimes called synergies—suffice to explain the majority of the variability in the observed muscle activation patterns[75, 118, 18, 39, 119, 3, 69]. Principal components analysis (PCA) is a widely used technique to extract these few independent basis functions (correlation vectors called principal components, PCs) from high-dimensional data[27]. In this case, PCs are often called the experimental representations of synergies of neural origin[75].

Therefore, we applied PCA to points (i.e. muscle coordination patterns) sampled from the feasible activation space at each force level. This provides the PCs that describe the correlations among valid muscle activation patterns for a given task. For example, the feasible activation space P in a 3-muscle system with one constraint is a 2-dimensional polygon embedded in 3-dimensional activation space. Thus,

applying PCA to points sampled from the polygon will extract 2 synergies (i.e. 3-dimensional correlation vectors PC1 and PC2) that wholly explain the feasible activation space. By extension, in the case of fingertip force production in Fig. 3.1, the feasible activation space is a 3-dimensional polytope embedded in the 7-dimensional activation space. And PCA should extract, by construction, as many synergies as there are dimensions in the feasible activation space. For static force production with the index fingertip (i.e. 7 muscles and 4 constraints), we know that 3 principal components will describe 100% of the variance in points sampled from the feasible activation space (i.e. 7-dimensional correlation vectors PC1, PC2, and PC3).

Applying PCA to our data allows us to test whether and how its results change when applied to feasible activation spaces for different magnitudes of fingertip force. We applied PCA to feasible activation spaces for fingertip task intensities ranging from 0 to 90% of maximal. Specifically, we applied the *prcomp* function in R, and specified that the calculation operates on the covariance matrix of the raw data. We compare both the variance explained by each PC and their loadings (e.g. correlations among muscles) as the force level increases [152]. Lastly, we tested whether the dispersion (i.e., the two central quartiles) and median of our PCA estimates are sensitive to the number of points sampled from each feasible activation space. This is important in practice because experimental studies tend to record and analyze a practical number (e.g., 10) of repetitions of the same motor task from a given subject, and aggregate data from different subjects [153]. Although we have reported that subjects tend to exhibit similar muscle activations for a given task [138], performing dimensionality reduction on such few trials and across multiple non-identical subjects (i.e., samples in Figure 3.5) may lead to imprecise (i.e., uncertain) estimates of the synergies when sampling from high-dimensional spaces.

3.4 Results

We used our realistic index finger model to calculate the feasible activation space for the task of producing static fingertip force in the distal direction (see Fig. 3.1). By showing how this same space can be interpreted from three dominant perspectives, we propose a conceptual paradigm to unify today's theories of neuromuscular control. The model contains the contribution of each of the seven muscles of the finger to the resultant static fingertip force vector [149]. As described briefly in the Methods, all valid muscle activation patterns to produce a given fingertip force vector (i.e. all ways in which one can combine the actions of the seven muscles to produce a given fingertip force vector) are contained in a low-dimensional polytope embedded in 7-dimensional space. Hit-and-Run is a method for uniform polytope sampling that collects thousands of muscle activation patterns, which become a valid geometric approximation to the structure of the feasible activation space[145]. We examined how these feasible activation spaces (and their alternative representations) change with increasing task intensity (i.e. fingertip force magnitude, Fig. 3.1e). In particular, we studied task intensities between 0% (i.e. pure co-contraction without output force) and 100% of maximal static force (i.e. a unique solution [144]).

3.4.1 Parallel coordinate visualization naturally reveals the structure of the feasible activation space

Parallel coordinate visualization effectively reveals correlations that exist among the 1,000 valid muscle activation patterns for each intensity of desired fingertip force, and activation pattern cost, Fig. 3.2 and Fig. 3.3.

Parallel coordinate visualization provides deep insight into the interactions among muscles that can produce a given task. Because it allows interactive exploration of the feasible activation space, one can restrict the activation level of any one or multiple muscles to see the associated activation levels of the remaining muscles (i.e. see a subsample of the feasible activation set). Figure 3.4 shows how, for 80% of task intensity, only 46% (i.e. $\frac{461}{1,000}$) of all possible solutions survive when we only keep solutions where

EIP and EDC are below 80% of maximal excitation. We chose to limit the extensors, as they are both innervated by the radial nerve and are susceptible to limitation from, for example, neuropathy or stroke. This robustness-related system behavior is visible in other muscle pairs via the interactive parallel coordinates plot. We find that even a minor neural or muscle dysfunction can disproportionally compromise the solution space—even for sub-maximal forces. These results further challenge the definition of muscle redundancy as discussed in detail in[73, 149, 85], in that our description of redundancy may need to incorporate the structure of the feasible activation space to best describe how motor control can occur with perturbation to one or more muscles.

While we know from experience that a limitation on one muscle yields compensation from the others, Fig. 3.4 explains why, and how much to expect. All data used for Fig. 3.4 are for a task intensity of 80%. Given this task, limiting PI to 20% of maximal activation eliminates 30.1% of the valid solutions, while limiting DI to 20% eliminates 42.8% of them. The level of resilience to muscle limitation is intricately linked to muscle redundancy. When we select only the lowest 5% of L2 weighted costs (3.4, middle figure) there exist many 'near-optimal' solutions that are dramatically different (note the broad ranges and criss-cross patterns in the second panel of in Fig. 3.4). This wide space exists in spite of this strong criterion. Consider the range of activation for DI and PI in Fig. 3.4 which lies between 0 and 0.52 and 0.39, respectively. Limiting DI to 20% pulls PI's maximum down by nearly 0.20, and the converse has nearly the same effect. However, in both cases, the median activation among surviving solutions changes no more than 0.06. This emphasizes that understanding feasible activation spaces requires an understanding of its internal density and not just its bounds.

Evaluating the slope of the lines connecting muscles enables an intuitive understanding of inter-muscle correlations. The Pearson product-moment correlation coefficients were 0.99, -0.50, and -0.06 in the adjacent muscle pairs FDP—FDS, LUM—DI, and EIP—EDC, respectively. The interactive parallel coordinate visualization also allows for any pairwise comparison by simply dragging and reordering the vertical axes. This is an effective ad-hoc method to viewing the inter-muscle correlations for exploratory data analysis.

3.4.2 Low-dimensional approximations to the feasible activation space

We applied Principal Component Analysis (PCA) to sampled muscle activation patterns for 10 levels of task intensity. However, to replicate the fact that experimental studies can only collect a finite amount of data from each subject, we did this in an iterative fashion as follows. We collected 10,000 points sampled uniformly at random from each feasible activation space via Hit-and-Run [145]. From these 10,000 points, we sampled 10, 100, and 1,000 points at random (to simulate 'experimental' sample sizes), and applied PCA to each set of sampled points. For each of the sample sizes, we replicated the sampling 100 times, producing a distribution of principal component results, and thus, a distribution of variance-explained metrics for PC1 (and the same for the other components). This bootstrap analysis serves to inform how many samples one must collect from a subject to get an effective set of principal components. The H matrix was fixed across all replicates and samples.

Figure 3.5 shows the box plots describing the variances explained by the three principal components (PC1, PC2, and PC3) across task intensities. The third PC, PC3, explains the remainder of the variance (13—15%) for the resulting 3-dimensional polytope. Recall that the 4 task constraints ($f_{radial}, f_{distal}, f_{palmar}, \tau_{palmar}$) applied to 7 muscles yield a 3-dimensional polytope embedded in the 7-dimensional muscle activation space [144]); as such, the sum of all three PCs is exactly 100%. The supplemental website (linked in the Data Availability Statement below) contains alternate versions of Figure 3.6 with varying input transformations.

The box plots in Fig. 3.5 quantify how different amounts of data change the estimates of variance explained by a PC with task intensity (c.f. labels a vs. b vs. c). We see this dispersion is small in the center and right columns. Note that the ratio of variance explained between PC1 and PC2 between 50 to 80% of task intensity reveals changes in the aspect ratio of the feasible activation space with task intensity.

Importantly, we observe how using experimentally realistic samples sizes of 10 same-task repetitions per subject (the leftmost column in Fig. 3.5) not only does not capture this change, but its standard deviation is large enough to blur the notable differences that are known to appear with larger (but experimentally

unrealistic) sample sizes. The impact of impoverishing the number of independent samples fed to PCA reminds us that inadequate amounts of data obfuscate the underlying changes in the structure of the data analyzed (Fig. 3.5).

There were also changes in the loadings of the PCs, especially above 60% task intensity. While the ratio of variance explained between PC1 and PC2 gives a sense of the aspect ratio of the feasible activation space, the loadings of PC1 and PC2 speak to its orientation [149, 152]. Figure 3.6 shows how the loadings of the PC1 and PC2 vectors change across labels a, b, and c, Fig. 3.5. These loadings indicate that the orientation of the feasible activation space in 7-dimensional space change mildly at forces less than 65% of the maximal task force, and change more dramatically with higher forces.

These changes we see in (i) the lower and upper bounds of activations, and in (ii) the relative variance explained and (iii) loadings for all three PCs, demonstrate that the size, shape, and orientation of the feasible activation space changes with task intensity. The muscle activation distribution 'between the bounds' has profound implications for prior work which chiefly examines the ultimate upper- and lower-bounds of activation for tasks in different directions [107, 62]. Moreover, detecting changes in these high-dimensional structures is done in the best-case scenario, as it exists in the absence of experimental noise, within- and across-subject variability, and measurement error. As will be elaborated in the Discussion, this implies that PCs (i.e. synergies) are laborious to obtain experimentally, and even then do not necessarily generalize across intensity levels.

3.4.3 Changes in the probabilistic structure of the feasible activation space with increasing task intensity, or how muscle redundancy is lost.

The maximal static fingertip force vector in a given direction is produced by a single and unique combination of muscle activations. In contrast, any sub-maximal magnitude of that same vector is produced by an infinite number of solutions[116, 23, 149, 138]. Our analysis of feasible activation spaces at different

task intensities also allows us to characterize how this redundancy changes, and is eventually lost. The histogram heatmaps in Fig. 3.7 illustrate the changes and shrinking of within-muscle histograms (the space upon which probability density functions must operate) of valid activation levels across task intensities, converging to a single solution at maximal force output. These surface plots show how the normalized histograms (of 1,000 valid activation levels for each muscle at each intensity level) change at each of 100 equally-spaced levels of task intensity between 0 and 1. Following a muscle's column from bottom to top shows the activation histograms converge, naturally, to a spike at the unique value for maximal force production.

The low flat areas on the sides of each surface plot (e.g., clearly visible for DI) represent muscle activation levels that are not valid for that task intensity. That is, there exist no valid muscle activation patterns that contain that muscle at that level, and thus no points are found there.

These plots show *within-muscle probability functions* and their and rate of convergence to the unique solution for maximal force output across muscles. This is in contrast with the parallel coordinate plots in Fig. 3.3 that shows the *correlation across muscles*. Importantly, the histograms of activation levels for each muscle need not be symmetric, nor have the same shape (skewness and kurtosis) as the magnitude of the output force increases. For some muscles, the convergence accelerates after 60% or 80% of task intensity (as in LUM and EIP), while others converge monotonically along the entire progression (e.g., DI and PI). The peaks (i.e. modes or most common values) of each histogram at each task intensity represents the slice of the polytope that has the largest relative volume along that muscle's dimension (i.e. greatest frequency of that level of muscle activation across all valid solutions). Importantly, for most muscles (FDP, FDS, EIP, EDC, and LUM), the mode is not necessarily located at the same relative level of activation needed for maximal force output—even when scaling it linearly with task intensity. That is, the histogram at high levels of force is not simply a shifted version of the histogram at low levels of force. The histograms for DI are the exception, whose modes seem to scale linearly with task intensity.

These histograms and the parallel coordinate visualizations demonstrate that the probabilistic and correlation structure, respectively, of feasible activation spaces, do not necessarily generalize across task

intensities. Nor can they be inferred from their bounding boxes alone (i.e. upper and lower activation bounds for each muscle). An immediate example is how, for most task intensities, both EIP and LUM have similar lower and upper bounds near 0 and 1, respectively—yet their distributions are thoroughly distinct.

3.5 Discussion

3.5.1 Summary

Feasibility Theory, as a conceptual and computational approach, is a means to pierce the curse of dimensionality to establish a physics-based ground truth for neuromuscular control. This practical approach can now characterize—in an arguably complete way—the space of all valid ways to activate multiple muscles to produce a given task. This initial presentation is limited to the case of static force production. Additional work is needed to extend to sequences of tasks, as has been done for optimization during gait analysis—where the dynamical constraints during movement are applied in the context of static optimization [6, 107]. But we can already say that feasible activation spaces are, in fact, *the* high-dimensional landscapes upon which all neuromuscular learning, control, and performance must occur. These landscapes are predicated upon the strong experimental evidence for linearity in tension-to-force transduction in cadaveric [73], live [63], and modeled [122] studies. Therefore, they provide an integrative and unifying perspective that demonstrates how today's dominant theories of neuromuscular control are alternative approximations to feasible activation spaces from optimization, synergistic, and probabilistic perspectives. Feasibility Theory unifies these alternative approaches to motor control in the sense that feasible activation spaces represent an objective conceptual and computational common ground for these theories.

Note that these changes in the structure of the feasible activation space do not imply a given control strategy. They merely establish the bounds within which a species evolve a control policy for a given body

morphology. It is possible that the nervous system operates within a very small subset of this space—which could be described by different principal components and even probability distribution functions. Feasibility Theory, however, allows us to formally phrase and test such hypotheses.

3.5.2 The value of a cost function

Optimization is the oldest computational approach to finding valid muscle activation patterns that produce limb function (e.g.,[23]). While optimization is, of course, a reasonable hypothesis to explore neuromuscular control[129], some criticize it as a mathematical abstraction that anthropomorphizes neurons with the ability to choose, evaluate and follow cost functions in high-dimensions[35, 80]. There is, nevertheless, an intimate relationship between optimization and feasible activation spaces[25]. Optimization is analogous to finding the best solution in the dark—guided by repeated small steps based on evaluations of cost- and constraint-function. Computing the feasible activation space is then a means to 'turn on the lights' to see all possible valid solutions independently of cost[149]. Our complete sampling of high-dimensional feasible activation spaces [109, 83] allows us to compare and contrast *families* of solutions as per alternative cost functions instead of *individual* optimal solutions for a particular cost function. Fig. 3.3 demonstrates a complete description of families of valid coordination patterns and their relationship to alternative cost functions. Importantly, similar valid muscle activation patterns can have dissimilar costs and vice versa.

Thus, Feasibility Theory allows us to compare, in detail, alternative 'cost landscapes' across the entire set of feasible motor commands. By not having to insist on (or settle for) individual optimal—or near-optimal—solutions, we now have the same ability the nervous system has to explore, compare and contrast multiple valid (be they optimal or suboptimal) ways to coordinate muscles. Importantly, the relationships among valid muscle activation patterns emerge naturally from the physical properties of the limb and definition of the task. This *cost-agnostic* approach allows us to re-evaluate our assumptions about what the nervous system cares—and does not care—about. Lastly, this cost-agnostic approach also provides a powerful tool for inverse optimization, i.e. uncovering latent cost functions from data[137]. Our comparison across cost functions using parallel coordinates is already a form of inverse optimization.

55

3.5.3 Freedom under constraints

We have so far only used 'hard' task constraints which must be met exactly. However, Feasibility Theory also holds for soft constraints. For example, if a tendon-driven system is required to produce a 3D force vector in general distal direction and of a general magnitude (defined, say, as a sphere of 1.0 N radius centered on the nominal force), then we can apply these tolerances to the constraints defining the task. In effect, Feasibility Theory allows us to study both soft and hard constraints, where the latitude of the accuracy of the task naturally defines the precision with which muscle activation patterns must be selected. One can define the task intensity to be, say, anywhere between 50 and 60%, and study the concomitant increase in options available to produce forces within that range. Thus, one can characterize the changes in the feasible activation space as the task constraints are relaxed or tightened. Similarly, adding task constraints, such as the need to produce a particular stiffness at the endpoint [61], naturally reduces the dimensionality of the feasible activation space.

3.5.4 How to apply Feasibility Theory in an experiment

The most important input to this analysis is the relationship between muscles and the endpoint wrench. With this relationship composed as the H matrix as in 3.1, and a desired wrench w, Hit-and-Run can be used to produce parallel coordinate plots and density histograms for static force production with vertebrate limbs. For example, using a measure of muscle activation (such as fine-wire EMG), an experimentalist can compare the muscle activation pattern chosen by a research participant in comparison to the full feasible activation space that could achieve the same force, and see how those patterns change across fatigue, disability of a muscle, or manipulation of the feedback. After a tendon-transfer surgery, for example, the subject may initially inhabit only a specific part of the feasible activation space to produce a task, but must use feedback from the parallel coordinate plot to find solutions which take less effort. In effect, visualizing the entire feasible activation space could help us understand how rehabilitation can be guided towards more advantageous local minima[131].

In parallel, a scientist with a cost function to test on a model can quickly identify how different cost function parameters can affect the space of feasible activations, and see how specific the global optima is, with respect to other muscle activation patterns. Importantly, anthropometric differences affect the shape of the feasible activation space, so those subject-specific differences must be either incorporated or may be addressed through sensitivity analysis (such as Monte-Carlo manipulation of moment arm values, as in [62]).

3.5.5 Extension to dynamical force production or movement

Limbs are valuable for more than just their ability to produce isometric forces. First, there is the extension to 'non-static isometric' force production (e.g., rotating a grasped object with respect to gravity), which must contend with time-varying muscle activation-contraction dynamics and target grasp wrench (i.e. such that the object is always securely held against a time-varying gravity vector [95]). With changes in joint angles, the end-effector Jacobian, moment arm matrix, and vector of maximal feasible contraction levels per muscle will vary nonlinearly—and with kinematic redundancy as a possibility for a given endpoint location, we can introduce multiple feasible activation spaces that are capable of producing a given task force. Even a simple task in the workspace likely exhibits redundancy at different levels of abstraction, where redundancy is sourced from feasible activation spaces and joint null spaces simultaneously.

As muscles exhibit state dependence, the ability of an animal to produce precise dynamic forces is affected by the tendon tensions from moment to moment. The inter-muscle dynamics across a human index finger, for example, would necessarily require a feasible activation trajectory—which may or may not be representable by a convex hull. Applying Feasibility Theory to non-static isometric force production may require detailed investigation into the dynamics of musculoskeletal force transduction. In parallel to the dynamics, non-convexities may emerge from neural constraints or even nonlinearities and hysteresis of muscle function.

Secondly, Feasibility Theory can be extended to address dynamical behavior by applying it to a sequence of slices in time. That is, a dynamical task can be equivalently analyzed as a sequence of 'slices'

[6, 135, 26, 107]—where one can define a feasible activation space at each slice to determine how the nervous system must change activation patterns such that it is always implementing a valid solution [107]. When strung together, these individual spaces give rise to a 'spatiotemporal tunnel'—the time-varying extension of the feasible activation space (Fig. 3.8).

3.5.6 Structure, correlation, and synergies

The physical properties of the limb and the definition of the task together give rise to a low-dimensional structure of the feasible activation space [149]. Therefore, experimental recordings of muscle activations during limb function will exhibit a dimensionality that is smaller than the number of muscles[75, 3, 133]. Thus, applying PCA to the points sampled from the feasible activation space will inevitably find that few PCs can explain the variance in the data [20].

Our application of PCA at increasing task intensities (i.e. as muscle redundancy is lost) allows us to demonstrate—for the first time to our knowledge—several important features and limitations of dimensionality reduction. For example, we see that the aspect ratio (Fig. 3.5) and orientation (Fig. 3.6) of the feasible activation spaces change as their size shrinks (Fig. 3.7). Thus, such *descriptive* synergies [20] extracted from limited experimental observations likely do not generalize well across task intensities. Producing further insights into the feasibility-synergy relationship necessitates more objective metrics of the feasible activation space's structure.

The intensity-dependent structure of feasible activation spaces also has important consequences for motor control and learning. Producing force vectors at the endpoint of a finger or limb with accurate magnitude and direction are critical for versatile manipulation and locomotion[31, 144, 40]. If a given synergy can produce such accurate force vectors only for a given task intensity (and thus inaccurate vectors at other intensities), then the attractiveness of task-specific synergies to simplify the neuromuscular control of the limb is reduced. Although we do not present an analysis of task-irrelevant synergies, data from this paper can be concatenated prior to PCA analysis to explore how principal components vary across the entire distal task.

To compensate, the nervous system would need to learn, recall, and implement intensity-specific synergies. Prior experimental work has shown that the nervous system produces accurate fingertip forces of different magnitudes by, instead, likely scaling a remembered muscle activation pattern to produce forces of different magnitudes[138], together with full-dimensional error correction [143]. The observation of higher forces yielding more variable PC loadings indicates that lower dimensional substructures could approximate low- and medium-level forces for a given direction, motivating further analyses of PCA effectiveness across task-intensity (and with NMF, for example).

Our results also show how experiments with realistically moderate numbers of participants and test trials likely do not contain sufficient information to produce robust estimates of descriptive synergies across task intensities. As per the curse of dimensionality, sampling uniformly at random from high-dimensional spaces is exponentially difficult. Thus, even for this anatomically complete 7-muscle finger model, PCA depends strongly on the number of independent observations, such as uncorrelated trials from one subject or different subjects. Figure 3.5 shows that 100 to 1,000 such ideal data points from a simulated 'test subject' are needed to produce accurate estimates of changes in the PCs with task intensity (c.f. labels a vs. b vs. c). Future studies should explore how many experimental data points are sufficient from a given subject when recording from only a subset of the many (20+) muscles of human limbs in the presence of experimental noise, inherent stochasticity of EMG, and within- and between-subject variability. Some studies have begun to ask subjects to explore different ways to perform a given task [14, 76] (i.e. estimate the structure of the feasible activation space), but in practice, such studies cannot likely collect sufficient data uniformly at random to obtain accurate estimates of the descriptive synergies[75].

PCA is one of several methods to extract lower-dimensional representations of motor patterns [34, 127, 27]. Alternative techniques do not impose orthonormality constraints or over-estimate the real dimensionality of nonlinear underlying manifolds [27]. Similarly, Non-Negative Matrix Factorization (NMF) would not be subject to the flips in sign observed in Figure 3.5 [134]. We noted that for a given task intensity, a muscle's activation across the sampled solutions can have different variance than the other muscles, and

these variances change as task intensity increases (and the feasible activation space shrinks) (See the supplemental website for the task-variance figure). While PCA helps us uncover how these shapes change in this study, PCA can be leveraged to uncover different intramuscular relationships (e.g., analyzing the eigenvalue decomposition of the *correlation* matrix, as opposed to using PCA on the *covariance* matrix). Bootstrapping or data shuffling technique for sensitivity analysis are also applicable to dimensionality reduction techniques [152].

Feasibility Theory allows us to put dimensionality reduction in perspective. First, as a natural consequence of the definition of a task (i.e. the need to meet specific mechanical constraints). And second, as an approximation to the structure of the latent feasible activation space embedded in high-dimensions. While our results suggest caution when interpreting synergies obtained experimentally, we underscore that dimensionality reduction is, nevertheless, a useful approach to capture the general geometric properties of feasible activation spaces.

3.5.7 Toward probabilistic neuromuscular control

Our results are particularly empowering for the emerging field of probabilistic neuromuscular control[66, 67, 100]. Suppose that the nervous system uses some form of probabilistic or Bayesian learning and control strategy. Such approach requires two enabling—and biologically plausible—elements: *trial-and-error iterative exploration* to build prior distributions, and *memory-based exploitation* of the probability density functions used to approximate the feasible activation spaces[66]. The parallel coordinate plots and histograms in Fig. 3.2 and 3.7 provide, to our knowledge, the first complete[109, 83] characterization of such multi-dimensional conditional motor control spaces for a realistic tendon-driven system performing a well-defined task (i.e. activation of one muscle is contingent upon the activations of the other muscles). With a better understanding of the physical task, future studies into optimal motor control can leverage the feasible activation space to contextualize motor control policies, whether they are experimentally-observed or theoretically predicted [15]. As mentioned above, the muscle activation patterns that the nervous systems actually use will necessarily be a subset of these feasible activation spaces.

Feasibility Theory critically empowers the study of fundamental aspects of probabilistic control. For example, an organism can only execute so many trial-and-error iterations during learning, likely too few to completely and exhaustively sample the high-dimensional feasible space of interest. This makes it much more likely that, by virtue of being more easily found, an organism will find and preferentially exploit the strong modes (i.e. narrow and high peaks in Figs. 3.3, 3.4, and 3.7) of the multi-dimensional probability density functions than any other region of feasible activation spaces. Thus, first, the maximal ranges of feasible activations described by the bounding box [110, 62] may have little practical bearing on how those tasks are learned and executed. And second, those same strong modes would represent strong attractors to create and reinforce motor habits. Habitual control has been proposed based on experimental and empirical data as an alternative to a strict optimization approach to neuromuscular control[35, 44]. Our work now provides the computational means to link habitual to probabilistic control in isometric force production. This allows us to generate testable hypotheses of how these motor habits are defined by the structure of the feasible activation space, how easily they are learned by the organism, and how difficult or easy it is to break out of them [97].

Motor function likely emerges from trial-and-error [1] or imitation [91, 22] to identify, remember and adopt easily-found, good enough solutions in the feasible activation space—independently of their cost. It is then possible to use some heuristic approach to improve performance to transition to less likely—but potentially 'better' solutions as per some metric relevant to the individual—subregions of the solutions space. But this likely requires numerous iterations in practice, which explains why only a few of us are experts at a given motor task, or why rehabilitation is so difficult[1, 81, 50].

3.5.8 Feasibility Theory as a theory of motor control

Feasibility Theory goes beyond Bayesian control by underscoring how the *physics* of the body, and the properties of the task are the arbiter that guides the biological process of finding, exploring, inhabiting, and exploiting low-dimensional solution spaces embedded in high-dimensions. Feasibility Theory espouses heuristic local searches—driven by the memory of likelihoods of different individual solutions—to

create what ultimately are useful, yet likely sub-optimal, motor habits. These processes hinge on trial-and-error, memory, pattern recognition, and reinforcement that come naturally to neural systems. Even though Feasibility Theory is presented in the context of neural control of the human hand, it applies to tendon-driven organisms in general.

Importantly, organisms perform strict optimization or synergy control at their peril. A feasible activation set is low-dimensional because it loses one dimension with each functional constraint that is being met [61, 144]. Thus, moving along such low-dimensional spaces to find a new valid solution is equivalent to moving along a line (which has zero volume) in 3-dimensional space. Taking a step from any one valid point to another valid point on the feasible space runs the risk of 'falling off' and failing at the task—a risk that is exponentially exacerbated in higher-dimensions. Thus, searching for improvements in the neighborhood of a known solution necessarily risk task failure and potential injury. These are all arguments in support of the evolutionary and developmentally useful strategy to use good-enough control based on habit or sensorimotor memory rather than optimization or synergy control[35, 45].

This line of thinking has consequences to neurorehabilitation. Neurological conditions disrupt feasible activation spaces, be it by affecting anatomy of the limb, muscle strength, and independence with which muscles are controlled. Functional recovery following the disruption, if not destruction, of the landscape of valid muscle activation patterns, requires re-learning existent or building new probability density functions. Older adults suffering from reduced perceptuo-motor learning rates are presented an even more constrained feasibility space [29].

A probabilistic landscape for neuromuscular function begins to explain why neurorehabilitation in aging adults is so difficult (e.g., [53, 81]) and why motor learning in children takes thousands of repetitions[1]. But it empowers us to leverage knowledge of the families of feasible solutions to create new rehabilitation strategies and testable hypotheses around them.

Conflict of Interest Statement

Author Contributions

Funding

Acknowledgments

Table 3.1: Applicability and compatibility of Feasibility Theory with dominant theories of neuromuscular control

Dimensionality Reduction	PCA, NMF, etc. describe the general shape and structure of the feasible activation space. The resulting basis functions serve as an approximation of the input-output relationship of the system (i.e., descriptive synergies).
Motor Primitives / Synergies / Modular Organization	If the basis functions mentioned above are of neural origin, they would be the means by which the nervous system inhabits the feasible activation space and executes valid solutions (i.e., prescriptive synergies).
Uncontrolled Manifold (UCM) Theory	The UCM Theory emphasizes that the temporal evolution of muscle activation patterns in the interior of the feasible activation space need not be as tightly controlled as those at its boundaries. This is because moving between interior points has no impact on the output as they constitute the null-space of the task (i.e., they are 'goal-equivalent' as in [104]). In contrast, Feasibility Theory describes details of the *structure* of the feasible activation space.
Exploration-Exploitation	Heuristic and trial-and-error approaches can be used to find points within the Feasible Activation Space because it is a needle-in-a-haystack problem. By definition, there is a small likelihood of finding a point on a low-dimensional manifold embedded in a high-dimensional space (e.g., the volume of a line is zero). Thus, the families of valid solutions found are preferentially adopted (e.g., as motor habits[35]). Such a heavily iterative approach is compatible with reinforcement learning[142], motor babbling[130], the hundreds of thousands of steps children take when learning to walk[1], or the mass practice a patient needs for effective rehabilitation[78].
Probabilistic Neuromuscular Control	If muscle activation patterns within the feasible activation space can be found (by any means), they can be combined to build probability density functions (i.e., Bayesian priors). A likely valid action for a particular situation can then be selected via Bayes' Theorem (e.g.,[66]).
Optimization / Minimal Intervention Principle / Optimal Control	Every point in the feasible activation space is, by definition, valid. However, if a cost function is used to evaluate each point in it, the feasible activation space is transformed into a fitness landscape. Optimization methods can then navigate this fitness landscape to find local and global minima (e.g.,[32, 6, 129]).

3.6 Data Availability Statement

The datasets generated and analyzed for this study can be found freely available at https://github.com/bc/space, and at the supplemental website http://valerolab.org. We designed a web-based parallel coordinate visualization that lets users interactively limit muscles, select solutions, and calculate effects on the feasible activation space from each post-hoc constraint (Fig. 3.4). Our companion site includes ample documentation, code implementation in Scala (with a comprehensive test suite), and all data visualization code in R, including an overhead view of Figure 3.7.

Figure 3.2: **Parallel coordinates characterize the high-dimensional structure of a feasible activation spaces.** Consider four points (i.e. muscle activation patterns) from the polygon that is a feasible activation space (a). The activation level for each muscle (i.e. the coordinates of each point) are sewn across three vertical parallel axes (b). As is common when evaluating muscle coordination patterns, each point can also be assigned a cost as per an assumed *cost function*. The associated cost for each muscle activation pattern can also be shown as an additional dimension. We show three representative cost functions (c). Activation levels are bound between 0 and 1, and costs are normalized to their respective observed ranges.
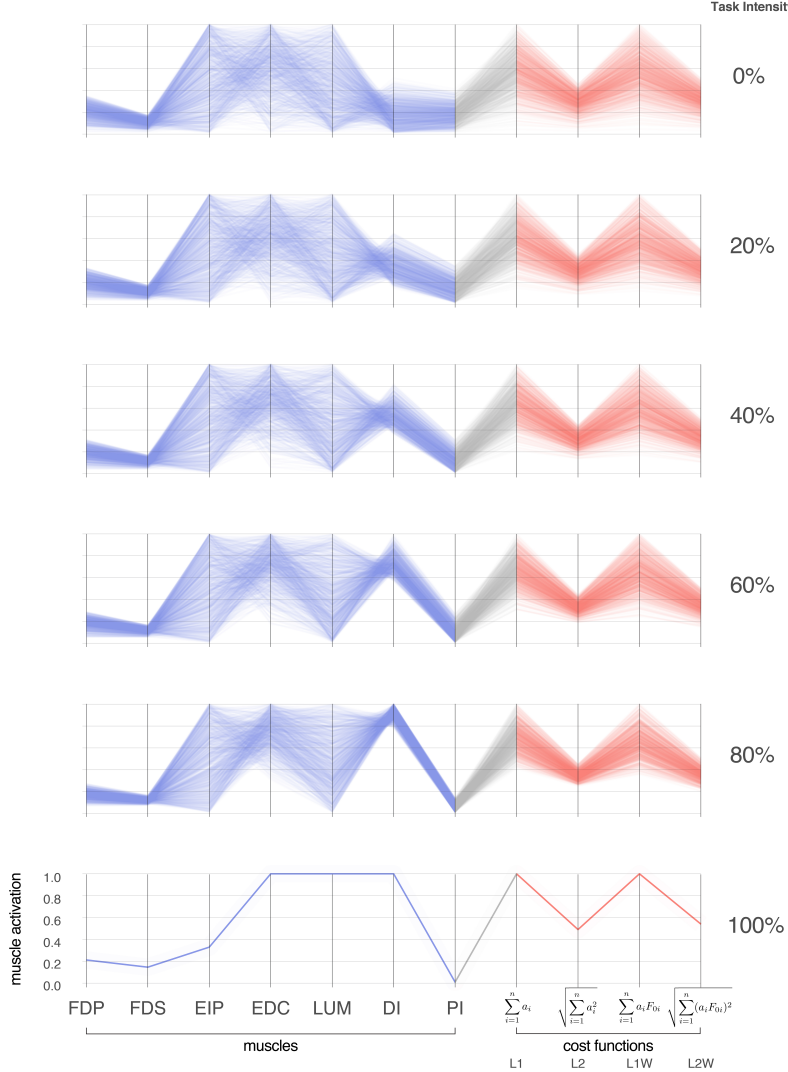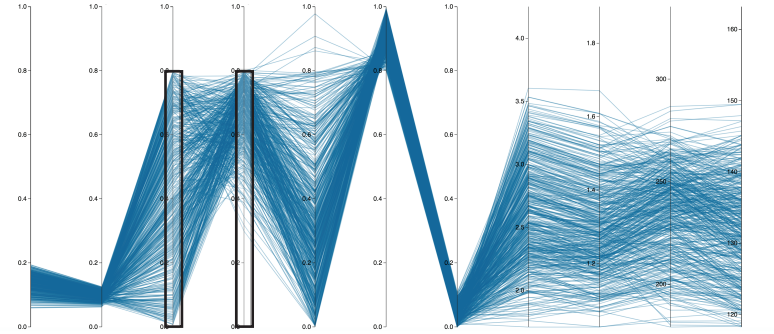
Figure 3.3: **Activation patterns of the seven muscles of the index finger across six intensities (magnitudes) of a fingertip force vector in the distal direction.** The connectivity across parallel coordinates visualizes the correlations among muscle activation patterns at different task intensities. At the extremes of 0% and 100% we have, respectively, the coordination patterns that produce pure co-contraction and no fingertip force, and the one unique solution for maximal fingertip force [144]. In between, we see how the structure of the feasible activation spaces changes, and that much redundancy is lost rather late (at intensities greater than 80%, in agreement with [110]). In blue are the activation values, and in red are normalized costs for four common cost functions in the literature. For each task intensity, we produced 1,000 points that are uniformly distributed in the polytope via the Hit-and-Run method. The muscles are *FDP: flexor digitorum profundus, FDS: flexor digitorum superficialis, EIP: extensor indicis proprius, EDC: extensor digitorum communis, LUM: lumbrical, DI: dorsal interosseous, PI: palmar interosseous.* Color is used solely to differentiate muscle activations (blue) from cost values (red).
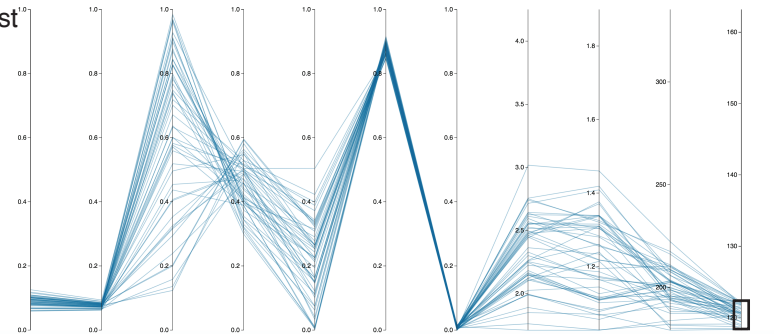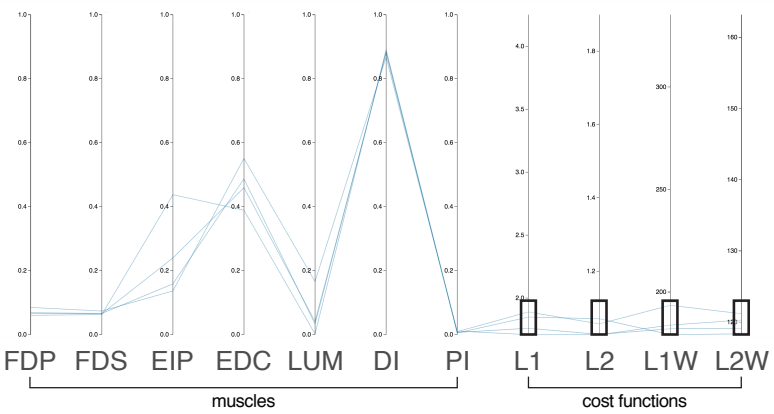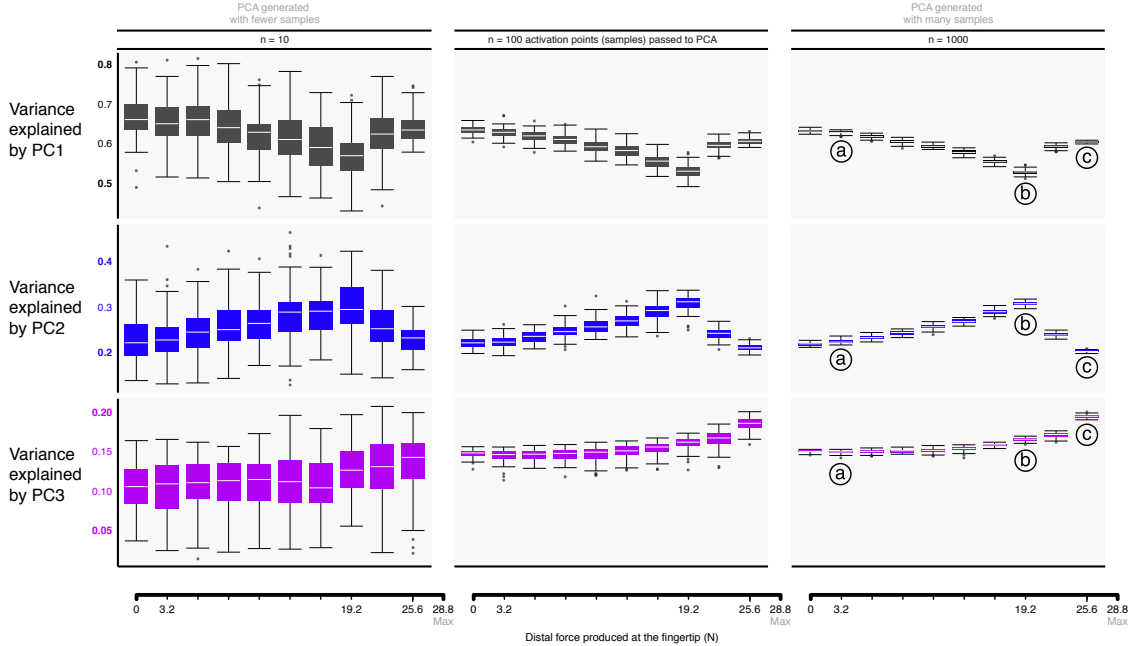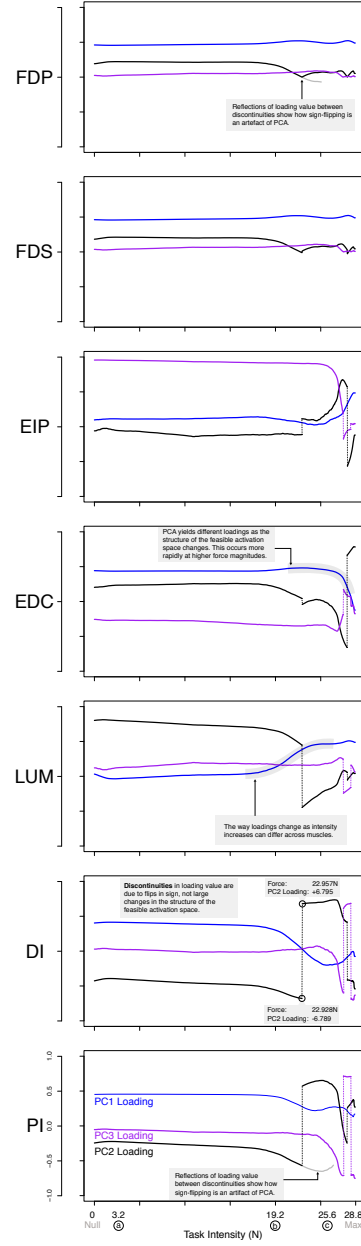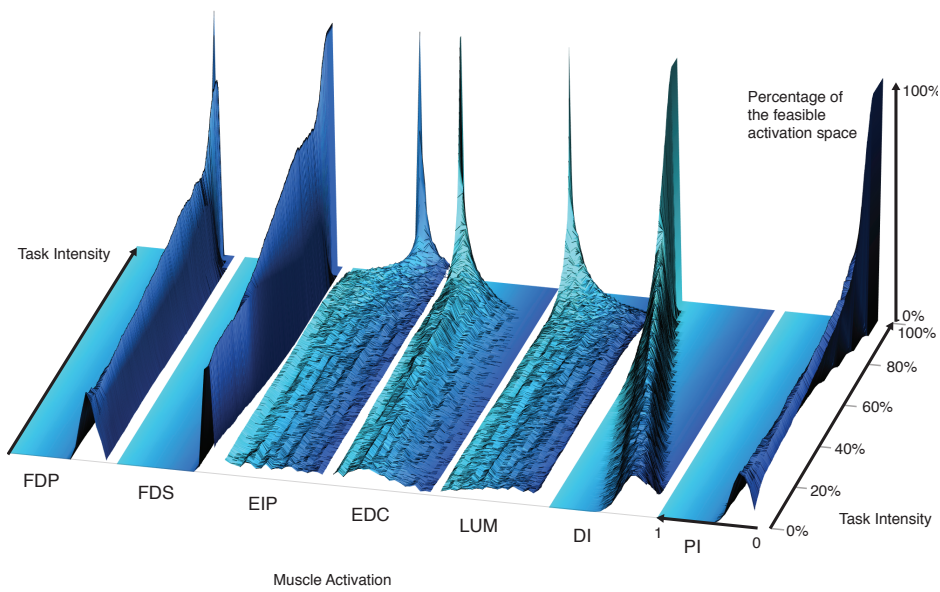
Figure 3.4: **Exploration of the feasible activation space for task intensity of 80%.** Here we show three informative examples of constraints applied to the points sampled from the feasible activation space (n=1,000; axes match those of Fig. 3.3). With this interactive visualization, we can easily see how the size (i.e. number of solutions) and characteristics of the family of valid muscle activation patterns change. For example, in the event of (Top) weakness of a group of muscles (54% reduction), (Middle) selection of the lowest 5% of a given cost function (95% reduction), and (Bottom) enforcing the lowest 10% of cost range across multiple cost functions (99.6% reduction). In all cases, the family of valid muscle activation patterns retains a wide range of activation levels for some muscles. While it is challenging to understand the structure of the feasible activation space with a static plot of the parallel coordinates, interactively manipulating the muscle ranges on one or multiple axes makes it very easy to view and describe how muscle activations change in the face of different constraints.
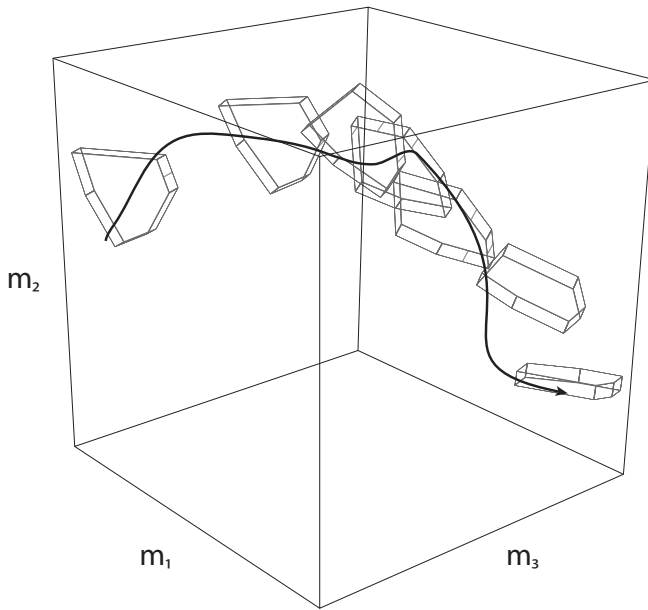
Figure 3.5: **Approximating the structure of feasible activation spaces via principal components analysis (PCA) is sensitive to both the task intensity and the amount of input data used.** Rows show the variance explained by the first (top) through third (bottom) principal components with increasing data points for a given replicate (left to right). Hit-and-Run sampling provides the ground truth for the high-dimensional structure of the feasible activation set at each task intensity. Each box plot, across all subplots, is formed from 100 metrics (replicates), where each metric is the PC variance explained for a replicate 'subject' which performed the task *n* times (where n is one of 10, 100, or 1000 task repetitions). We find that PCA approximations to this structure do not generalize across tasks intensities (i.e. the polytope changes shape as redundancy is lost), and numbers of points. That is, > 100 muscle activation patterns should be collected from a given subject to confidently estimate the real changes in variance explained as a function of task intensity. Compare points labeled a, b, c, corresponding to 11, 66, and 88% of task intensity, respectively.

Figure 3.6: **PCA loadings change with task intensity** For each of 1,000 task intensities, we collected 1,000 muscle activation patterns from the feasible activation space and performed PCA. The facet rows show the changes in PC loadings, which determine the direction of all PCs in 7-dimensional space. Note that the signs of the loadings depend on the numerics of the PCA algorithm, and are subject to arbitrary flips in sign [27]—thus for clarity we plot them such that FDP's loadings in PC1 are positive at all task intensities. Dotted vertical lines connect loadings of PC2 and PC3 in spite of flips in sign. A discontinuity here is not indicative of a major change to the feasible activation space. It instead, is a result of how PCA selects loadings. The shape of the activation space has tilted at these points, thereby flipping the sign. Note that the values are the same before and after the jump, less the sign. These loadings (i.e. synergies) change systematically, as noted for representative task intensities a, b, c in Fig. 3.5, and more so after b. This reflects changes in the geometric structure of the feasible activation space as redundancy is lost.

Figure 3.7: **The within-muscle probabilistic structure of feasible muscle activation across 1,000 levels of fingertip force intensity.** The cross-section of each density plot is the 50-bin histogram of activation for each muscle, at that task intensity. The changes in the breadth and height for each muscle's histogram reveal muscle-specific changes in their probability distributions with task intensity. Height represents the percentage of solutions for that task. The axis going into the page indicates increasing fingertip force intensity up to 100% of maximal. Color is used to provide perspective. It is interesting to note that, for example, both extensor and flexor muscles are used to produce this 'precision pinch' force. This is to be expected as the activity in the extensors is necessary to properly direct the fingertip force vector [141].

Figure 3.8: **Spatiotemporal Tunneling.** A dynamical movement can be decomposed into a sequence of slices in time, where each slice has a corresponding feasible activation space. Strung together, the sequence of feasible activation spaces form the 'spatiotemporal tunnel' through which the neuromuscular system must operate. In this 3-dimensional schematic example, the black line represents one valid time-varying sequence of activations for three muscles. Because this sequence exists within each feasible activation space, it necessarily meets the constraints of the dynamical task at each instant.

Chapter 4

Spatiotemporal tunnels constrain neuromuscular control

Brian A. Cohn [1] and Francisco J. Valero-Cuevas [2,3]

[1]University of Southern California, Department of Computer Science, Los Angeles, CA

[2]University of Southern California, Department of Biomedical Engineering, Los Angeles, CA

[3]University of Southern California, Division of Biokinesiology and Physical Therapy, Los Angeles, CA

4.1 Abstract

Animals must control their limb endpoint forces for tool use and manipulation. And while decades of research has elucidated much about **how** intentions lead to physical forces and movements, and **what** correlations exist between muscles, these methods do not address core questions about **why** these relationships occur, and what neuromuscular and physical requirements most constrain their possibilities. Our prior work has more faithfully enumerated the full dimensional neuromuscular control landscapes upon which learning must occur, but we did not address the constraints of how muscles can perform within these spaces. In this study, we address this gap by stochastically exploring the addition of a simple time parameter, and rather than optimize or reduce the dimensionality of our null space, we fully enumerate the space as a product polytope in 49 dimensions—7 muscles over a 7-step task, with the constraint matrix being solved in one step. As a result, we can select only those trajectories which meet the activation-contraction

constraint across the entire trajectory, and sample from the space in a new manner that is traditionally intractable for analyzing muscular systems of this size. By defining the physical realities that govern how evolution must derive neuromuscular structures, we discovered how powerful even simple time constraints are, and how they warp the ways muscles interact, correlate, and optimize. This theoretical and computational work offers new tools to generate hypotheses across the interplay of high-dimensional neurology and full-dimensional task physics, highlighting how the time-varying nature of activations define and limit how neuromuscular systems can evolve and learn motor patterns.

4.1.0.1 Author Contribution

BC designed analyses and code, FV supported the deep analysis of neuromuscular implications of the results.
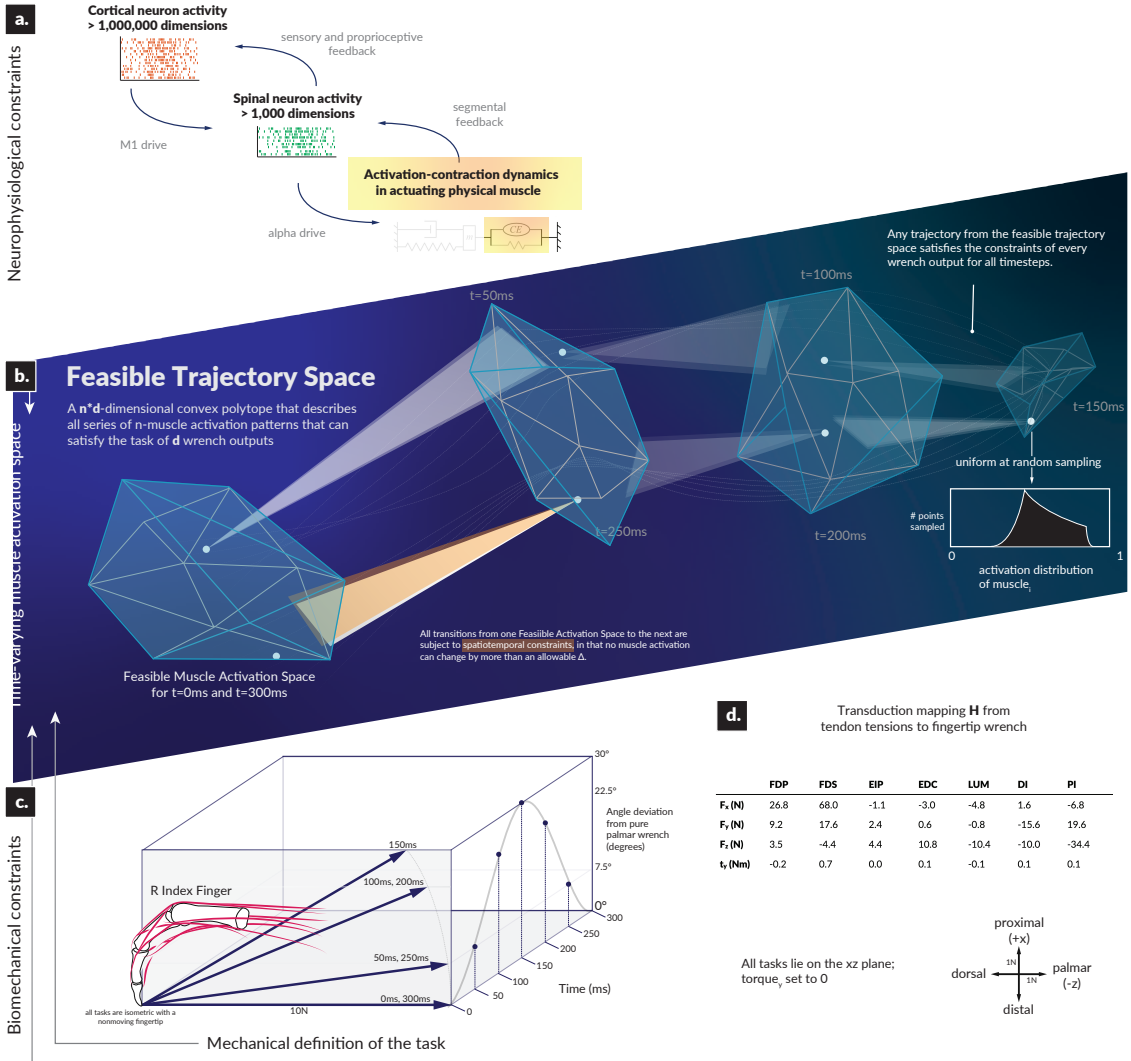
4.2 Introduction

For the case of a human tendon-driven fingertip generating endpoint forces, having more muscles than output constraints raises a long-explored question: how do animals find and select a muscle activation pattern that work, given a high dimensional space to choose from [4]? For much of the past 40 years of neuromuscular control, there have been deep analyses of the cortical circuits, evaluations of the muscle activity, and knock-out studies of different points along the pathways providing motor drive. Prior work with Feasibility Theory [30] has effectively sampled from the Feasible Activation Space, a representation of the way muscles can combine their activations to effect an output wrench[149]. Many effective procedures exist for analyzing and interpreting the high dimensional nature of under-constrained motor control, including extraction of a series of lower-dimensional vectors [3, 133, 2], approximation of their distribution as Bayesian priors [66], or by application of a heuristic cost-function to find optimal subtrajectories [129, 125]. Feasibility Theory posits that the full dimensionality of tendon-driven systems must be preserved to yield a fair and common ground in contextualizing theories of neuromuscular control, chiefly

the aforementioned synergistic, Bayesian, and optimization-based methods. However, forces change over time, and it's still difficult to this day to fully describe why an animal chooses a particular motor pattern in redirecting or scaling force. Those internal 'functions' are often approached from the musculoskeletal side, by measuring directly from the muscles activity, via measurement of tensions over time, and through spinal and cortical imaging. Much incredible progress has been made to incorporate the time-varying dynamics into these activation-to-wrench approximations, in the case where dimensionality is reduced by optimization[108], or at a series of points in a transect from the most optimal trajectory to the least [111].

Muscles cannot act immediately—they are a single element of a dynamical system with many moving parts. With motoneurons being discharged stochastically, and with limited chemical energy at any given moment, there are neurological, chemical, physiological, and physical constraints to creating changes in musculotendon tension, which acts as a series elastic element. Muscle-length and muscle velocity significantly impact the force applied at the tendon's point of insertion, and different parts of the muscle have different response speeds (i.e. slower and faster twitch models of motor control). Furthermore, integumental structures (including skin) and passive musculoskeletal structures (including ligaments) serve as a dynamical system which have their own time-varying dynamics and state. For the context of this study, we do not fully model these delays and limitation–rather, we make a upper-bound observation of the fastest change in muscle activation over time as described in the Methods.

If we could adequately reduce the size of the feasible activation space—all ways to achieve the task— we would be able to close the boundaries for hypotheses on motor control, reducing the space of viable hypotheses, and allowing for immediate feedback for scientists looking to build models which explain for the behavior of vertebrate tendon-driven control. This paper provides a novel computational tool for stochastically, and **fairly** sampling the feasible activation space, even in light of the incorporation of time as a new variable. We provide strong evidence that even a rather low-dimensional to low-dimensional tendon driven limb (a human index finger) has an incredibly broad distribution of activation trajectories for the simple task of redirecting a 10N force 30°, and that redundancy remains even after adding novel constraints of muscle activation-contraction dynamics to the full-dimensional feasible activation space.

a.

Neurophysiological constraints

Cortical neuron activity
> 1,000,000 dimensions

sensory and proprioceptive feedback

M1 drive

Spinal neuron activity
> 1,000 dimensions

segmental feedback

alpha drive

Activation-contraction dynamics
in actuating physical muscle

CE

Any trajectory from the feasible trajectory space satisfies the constraints of every wrench output for all timesteps.

t=50ms

t=100ms

t=150ms

b.

Time-varying muscle activation space

Feasible Trajectory Space

A **n*d**-dimensional convex polytope that describes all series of n-muscle activation patterns that can satisfy the task of **d** wrench outputs

uniform at random sampling

points sampled

0   1

activation distribution of muscle$_i$

t=250ms

t=200ms

Feasible Muscle Activation Space for t=0ms and t=300ms

All transitions from one Feasible Activation Space to the next are subject to spatiotemporal constraints, in that no muscle activation can change by more than an allowable Δ.

c.

Biomechanical constraints

30°

22.5°

Angle deviation from pure palmar wrench (degrees)

7.5°

150ms

0°
300

R Index Finger

100ms, 200ms

250

50ms, 250ms

200

150

Time (ms)

all tasks are isometric with a nonmoving fingertip

0ms, 300ms

100

50

10N

0

Mechanical definition of the task

d.

Transduction mapping **H** from tendon tensions to fingertip wrench

	FDP	FDS	EIP	EDC	LUM	DI	PI
F$_x$ (N)	26.8	68.0	-1.1	-3.0	-4.8	1.6	-6.8
F$_y$ (N)	9.2	17.6	2.4	0.6	-0.8	-15.6	19.6
F$_z$ (N)	3.5	-4.4	4.4	10.8	-10.4	-10.0	-34.4
t$_y$ (Nm)	-0.2	0.7	0.0	0.1	-0.1	0.1	0.1

proximal
(+x)

dorsal   palmar
(-z)

1N

1N

distal

All tasks lie on the xz plane; torque$_y$ set to 0

Figure 4.1: **Overview of the primary objective of this work.** Our objective is to computationally survey the Feasible Trajectory Space in the context of activation-contraction constraint, to better inform our perspectives of descending neuromuscular control paradigms.

We refer to this behavior as a spatiotemporal tunnel—the well-structured representation of feasible muscle activations that must be traversed by both evolutionary and learning timeframes. To achieve a series of isometric forces, the limb must meet the constraint of time (Figure 4.1).

4.3 Methods

As in [30, 113, 145] we define the linear transduction of tendon tensions into output endpoint wrench as

$$H * \bar{x} = \bar{w}. \tag{4.1}$$

Where H (a $[4,7]$ matrix in this paper for 4 output dimensions and 7 input tendon activations) represents the linear activation-to-wrench relationship, such that $H * x = \bar{w}_{output}$.

Wrenches are four dimensional as the index finger can produce a torque (i.e. scratching) $\bar{w} = (f_x, f_y, f_z, t_y)$[156]. As the data for H were collected in the same posture, and as there is strong evidence supporting the linearity of tendon-driven isometric force transduction in fixed postures, we do not need to model the intermediary Jacobian or the Moment-arm matrix [123, 144, 140, 113]. We define $x \in [0,1]^7$ where 1 represents 100% activation.

Note that the term *'muscle activation'* can take on different meanings depending on the level of the analysis being used. In our case, we use it as shorthand for the total signal needed to produce a given level of neural drive to produce force at each muscle. The reason we do this is that it encompasses the metabolic cost, intensity, and feasible rates of change of both the neural drive and muscle force. As such, it includes:

- Presynaptic input to a population of $\alpha-$motoneurones

- The neural command sent by the $\alpha-$motoneuron to the population of muscle fibers in its motorunits [115]

- The biochemical processes required for the release and uptake of acetylcholine at the motor end-plate of each muscle fiber [136]

- Ca+ release and uptake by the *sarcoplasmic reticulum* [136]

- The cross-bridge cycle at the sarcomere to produce, hold and change the level of muscle force

We make the simplification, without loss of generality, to not distinguish between muscle types and consider equal time constants for the increase and decrease of neural drive and muscle force.

And while many approaches minimize $\bar{c}^T \bar{x}$ where $\bar{c}$ represents a vector of linear weights to combine with $\bar{x}$ to form a metric of cost, e.g. if $\bar{c} = (1,1,1,1,1,1,1)$, $\bar{c}^T \bar{x}$ would compute the 'sum cost of activation', or $\bar{c} = (0,0,0,0,0,0,1)$ would compute the 'sum of just *palmar interosseus*'. Nonlinear objective functions have also been used to better understand weighted L_2 and L_3 metabolic cost functions[30]. For this paper, rather than minimization or optimization on an arbitrarily defined cost function (a model choice in itself) our approach instead **samples from the nullspace** of $\bar{x}$ uniformly-at-random (*u.a.r*). We leverage the same computational geometry technique 'Hit-And-Run' as in [30, 145], which is originally described in [83, 82].

Synaptic drive applied to motor units create forces, which ultimately generate muscle forces, and accumulate to tendon force. The tendon is compliant and together, the musculotendon is a big dynamic system with many physiological and physical constraints. It's a series elastic element.

4.3.0.1 Hit and Run sampling of the feasible activation space

Visualization and analytics of these high dimensional structures requires unique approaches to highlight different aspects of feasible activation spaces, and there has been some success in using 2D and 3D visualization to decompose neural control of force [145, 30]. As the dimensionality of the space increases, the ratio of out-of-polytope to in-polytope volumes within the unit cube expands exponentially, thereby making 2D and 3D approaches computationally intractable with systems with more than 2 muscles. Like in prior work, we sample the space with the Hit-and-Run algorithm—a Markov chain propagating within the polyhedron that yields a uniform-at-random distribution within the volume of a given convex polytope. This method is agnostic to measures of metabolic or neurologic cost, and allows for contextualization of the solutions optimization may select.

4.3.0.2 Defining the temporal constraints

One core limitation of our prior work [30] is the single-moment analysis, that does not take into account the amount of change the CNS must perform to move from solution to solution, from task to task. Muscles do not act with infinitely fast response times; to respect this, we incorporate an element of temporal constraint in our model by limiting a muscle's change in activation between $\pm\delta\%$ over a 50ms interval. Given the observation that deactivation in vertebrate muscle is often slower than activation[115], we set this limit to the faster of the two, forming a conservative bound. We refer to this metric as the activation-contraction constraint, and as we take the absolute value of the deltas, this metric is always set between $[0, 1]$. A constraint value of 0.25 means that in 50ms, activations can change their output by no more than 25% of their maximal tension.

4.3.1 Specimen

Our activation-to-wrench model H was sourced from an experiment using cadaver fingers[154], with original data (n=11) from [116]. To reveal the effects of activation-contraction constraints on a time-dependent feasible activation space, we leveraged a stochastic Monte Carlo technique to fairly extract activation trajectories—Hit-and-Run[83]. In addition to being normalized between an activation of 0 and 1 (muscles can't go negative as they can only pull), muscles were constrained in their ability to change their output activation from moment to moment. For each moment in time, the endpoint vector had to meet the requirements of its desired output wrench within a series of seven tasks. Formally, we add new constraints in the way the activations can change, which are ultimately classifiable as Lipschitz constraints [114, 19]. Formally, we sample *u.a.r.* from the null space on *x*, given A and b where $x \in [0, 1]^n$. Our Lipschitz Constraints (referred to hereafter as 'activation-contraction constraints' as they serve to link different motor patterns over time to different output wrenches.

$$|x_{i+1} - x_i| \leq \delta x \in [0, 1]^7 \tag{4.2}$$

$$\begin{pmatrix} f_x \\ f_y \\ f_z \\ \tau_y \end{pmatrix} = \mathbf{w} = H\mathbf{a} = H \begin{pmatrix} a_1 \\ a_2 \\ a_3 \\ ... \\ a_7 \end{pmatrix}, \mathbf{a} \in [0,1]^7 \tag{4.3}$$
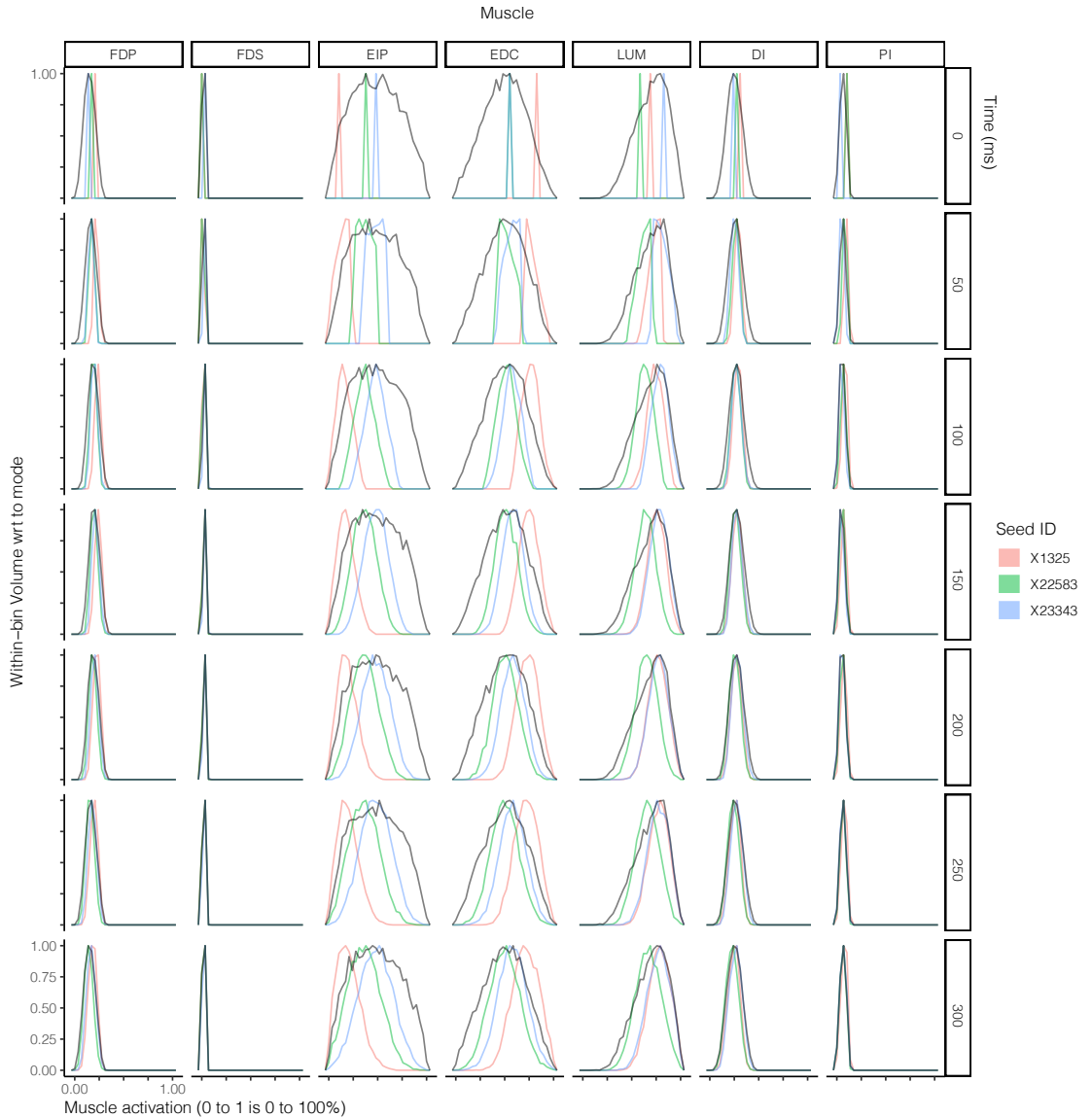
We set the task to a series of 7 individual wrenches performed over the course of 300ms, which starts at a pure f_x force (towards palmar), with a 30 degree rotation towards proximally (rotated about the axis defined by the ulnar direction), and a symmetrical return. The progress is shaped as a single cosine period, with the peak being the 4th index. Wrenches (0,6),(1,5),(2,4) are identical—providing a symmetric set of tasks to stay constant while the activation-contraction constraint demands may change.

We sampled 100,000 activation trajectories per activation-contraction constraint condition, where the constraints were set from 1 to 0.05 (Figure 4.3).
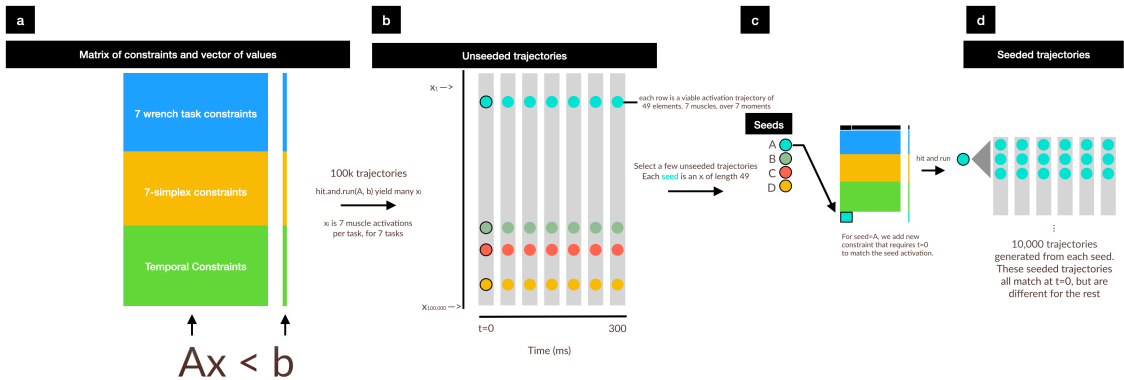
4.3.1.1 Analyzing unseeded vs seeded activation trajectory distributions

To address this difficulty in analyzing the distributions of muscle activations, we present the following ''unseeded vs seeded' trajectory analysis in Figure 4.2, with methods described in Figure 4.3.

We compute the possible trajectories when the first moment is fixed to a seed-point, and compare those ''seeded' trajectories to the ''unseeded' trajectories that were not fixed. It's important to note that unseeded trajectories are still sampled under the same activation-contraction constraint as their seeded counterpart, that all unseeded trajectories meet those activation-contraction constraint, and that all seeds must have a starting point that exists in the unseeded polytope. We describe our sampling procedure in Figure 4.3c and d. From out 100,000 unseeded trajectories we computed under a activation-contraction constraint of 0.12. From those, we selected 10 at random and called those our 'seeds'. For each seed, we trimmed off the t=50 to t=300 activation values, and appended a new constraint to the original constraint matrix, so all sampled
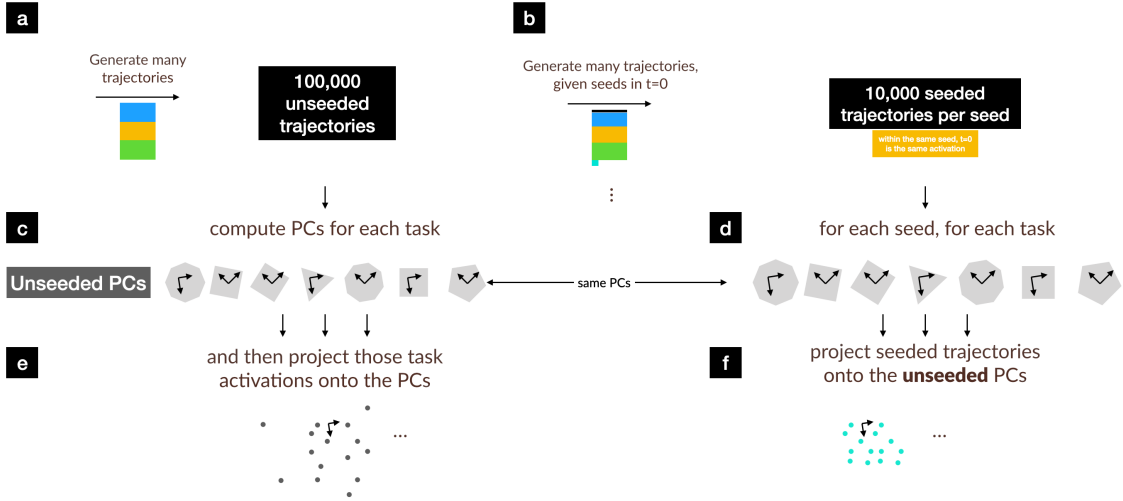
Figure 4.2: **Consequences of selecting a specific initial muscle activation pattern for a max activation-contraction speed of 0.25** Here we show the distributions of three trajectory seeds selected across a uniform sample of the unseeded H (Eq. 4.3). As in 4.10, lines are drawn by connecting the midpoints of 100 histogram bins. We observe strong hysteresis in the positioning of muscle activation when the seed trajectory locks the activation high or low on a given muscle, and that selecting a seed point implies that you cannot easily return to another seed point.

| a | b | c | d |

Matrix of constraints and vector of values

7 wrench task constraints

7-simplex constraints

Temporal Constraints

$Ax < b$

Unseeded trajectories

$x_1 \rightarrow$

each row is a viable activation trajectory of 49 elements. 7 muscles, over 7 moments

100k trajectories

hit.and.run(A, b) yield many x_i

x_i is 7 muscle activations per task, for 7 tasks

$x_{100,000} \rightarrow$

t=0   300

Time (ms)

Select a few unseeded trajectories
Each seed is an x of length 49

Seeds

A
B
C
D

For seed=A, we add new constraint that requires t=0 to match the seed activation.

hit and run

Seeded trajectories

10,000 trajectories generated from each seed. These seeded trajectories all match at t=0, but are different for the rest

Figure 4.3: **Method for generating unseeded and seeded trajectories** Unseeded trajectories can originate in any valid solution at $t = 0$ show their evolution across the subsequent polytopes (i.e., solution spaces) subject to the temporal constraints of activation-contraction dynamics of muscle. A seeded trajectory, on the other hand, is pulled from the same constraint matrix, but with an additional constraint: all of the points selected from a seed start at a same seed point (i.e., valid solution at $t = 0$). A seed point can be extracted from the unseeded trajectories. Seeded points can only evolve in time into subregions of the subsequent solution spaces that are reachable given the starting point *and* the temporal constraints of activation-contraction dynamics of muscle. Importantly, unseeded trajectories all meet activation-contraction constraints as well

trajectories were forced to match the seed in t=0 4.3. We computed 10,000 trajectories per seed. We show

all 10 in an interactive video described in Figure 4.10, and show three examples in Figure 4.2. Each show

the $[7, 7]$ by-muscle, by-moment distributions of the unseeded (in black) and seeded (a different color for

each seed).
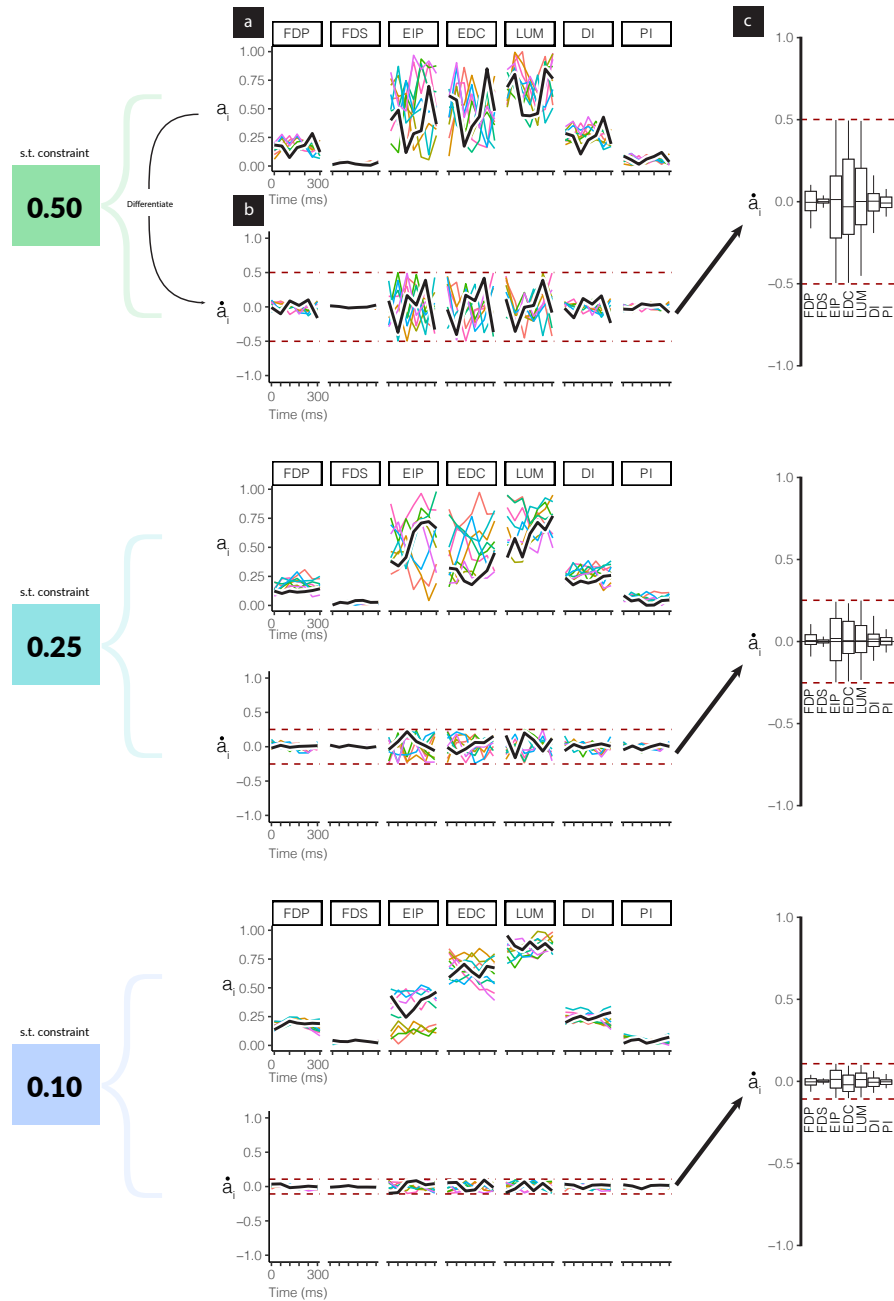
Figure 4.4: **Quantifying the evolution over time of the distribution of solutions for unseeded and seeded trajectories** Here we detail our method for analyzing and visualizing the effect of selecting a solution seeded in $t = 0$. We began by extracting one hundred thousand activation trajectories from H as in Eq. 4.3. With 10 of those trajectories, we extracted only the first value, then ran a further sampling paradigm on a modified constraint equation where the first activation pattern (of 7 muscle activations) had to match the seed's activations at t=0. As we want to visualize the effect of selecting a seed point, but cannot easily plot a 4D structure embedded in 7D, we applied principal component analysis to each of the 7 moments of time across the unseeded distribution. We then projected both the unseeded, and seeded activation trajectories across the first two PCs, highlighting where in the lower-dimensional space those solutions were most probable.

4.4 Results

The time history of feasible activations for a given action is highly restricted under activation-contraction

constraints imposed by muscle physiology 4.5.

First, Figure 4.5 demonstrate that, as the activation-contraction speed limit is reduced, the trajectories

become more spatially constrained in the regions of the feasible activation sets they can inhabit/exploit.
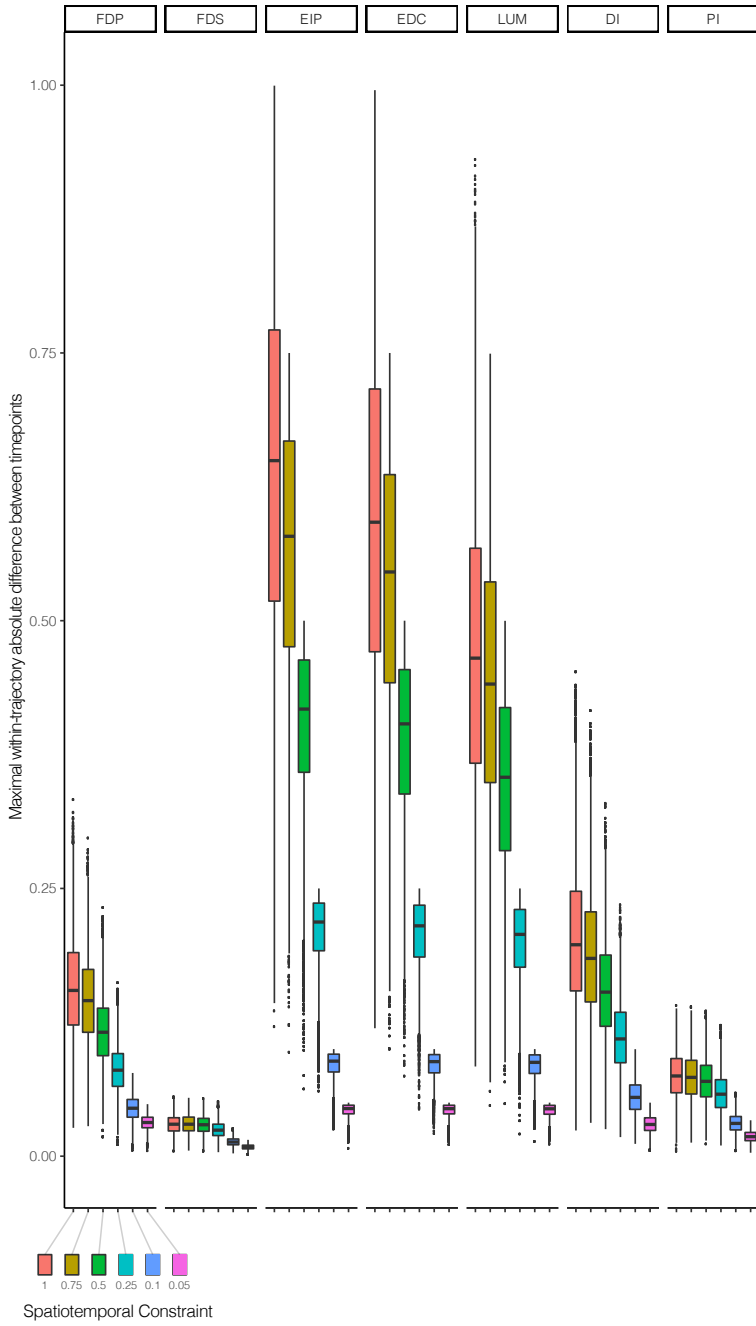
Figure 4.5: **Ten example trajectories with three levels of activation-contraction constraints** For each level, we show a) ten example trajectories, where each color is a different trajectory. b) Those trajectories, differentiated to show how quickly the activations were changing with the upper and lower activation-contraction constraints shown as dotted lines, and c) a distribution of the trajectory 'activation-contraction speeds', grouped by muscle. Note that colors on part c) do not relate to a) and b). Outliers are not shown on c. Note that unlike Figure 4.6 which shows the $max(|\dot{a}_i|)$, this figure shows the raw differentiated muscle activations as $\dot{a}$ and thus is signed from ± 1.

This allows us to describe the effects of the *activation-contraction constraint* under which muscle coordination happens to be able to produce a force and change its direction. Figure (4.5a,b shows 10 example trajectories (from the 10,000 calculated) as they traverse the 49-dimensional space (i.e., 7 muscles over 7 timepoints or tasks). For completeness, Figure 4.5c also provide boxplots of the per-muscle activation levels across all 10,000 trajectories sampled. Note that the limit on activation-contraction speed naturally affects muscles with larger feasible activation ranges (shown as the top row of Figure 4.8). But also note that as the maximal activation-contraction speed is reduced, those same muscles will visit/exploit increasingly smaller subspaces of their feasible activation sets. This spatiotemporal interaction is best seen in *EIP*, which has a naturally large range of feasible activation, which are suitably exploited when the activation-contraction constraint is less-constraining. But then shrinks as the constraint becomes more strict. However, changes also spill over to muscles with naturally smaller ranges of feasible activations such as *FDP*. This muscle has few trajectories with an activation-contraction rate greater than 0.25 to begin with, but becomes limited in range as the activation-contraction speed is reduced 4.5c.
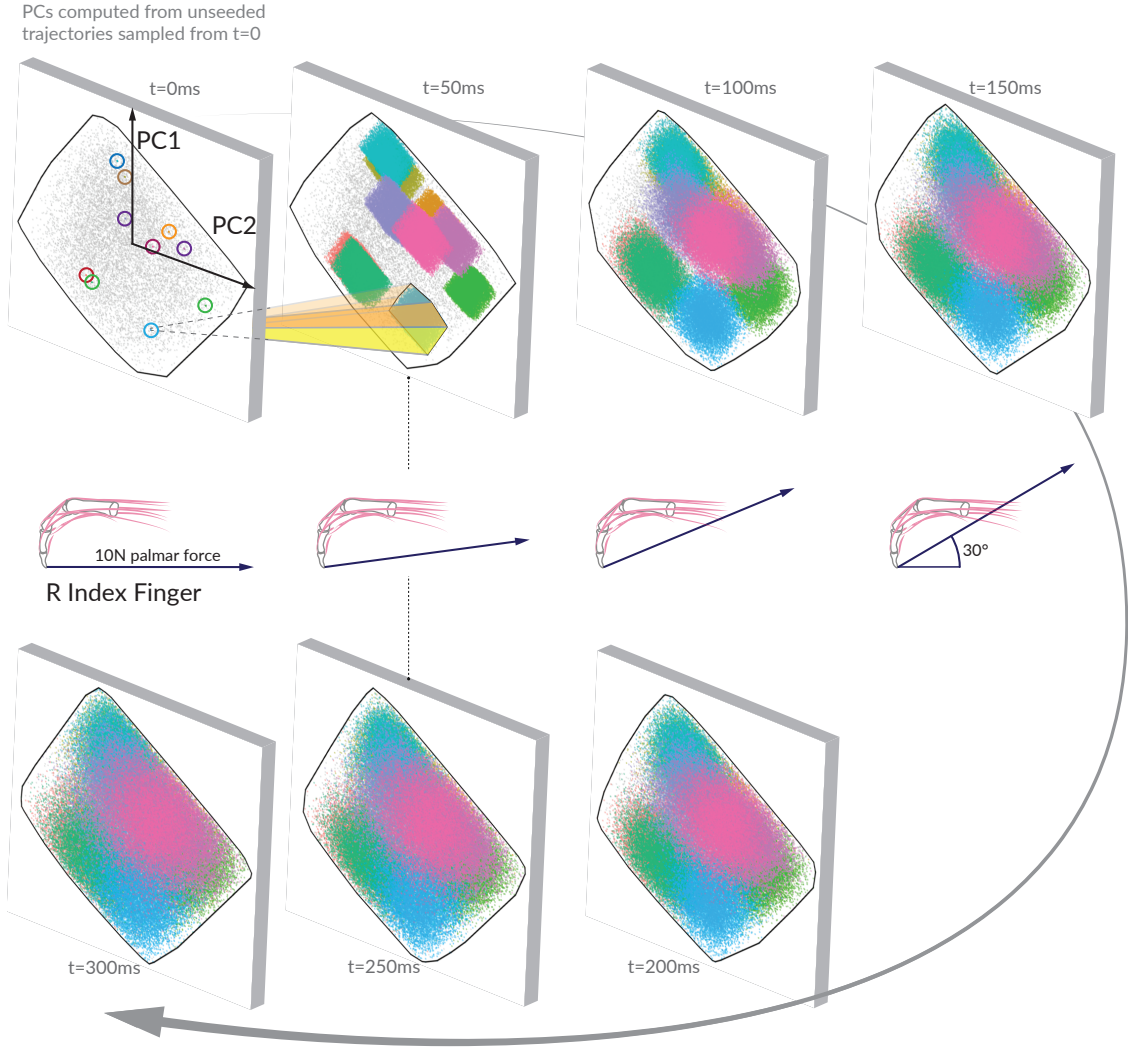
A closer look further confirms that muscles that have a narrow range of feasible activations will be least sensitive to changes in activation-contraction constraints. Figure 4.6 shows the distribution of the *maximal* change in activation for all muscles, and we see that only the muscles that have greater ranges of activation have non-overlapping central quartiles between 0.75 and 0.5 activation-contraction speed. It is hard to drag race in a driveway. We observe how, for example, *FDP*, *FDS*, and *PI* are more affected by the reduction of maximal activation-contraction speed.

Producing a fingertip force and changing its direction requires selecting a specific solution and implementing a specific sequence of activation patterns. Our 'seeded analysis' reflects the consequences of choosing an initial activation pattern (a 'seed') to subsequent feasible activation patterns (Figure 4.2). We show this for three choices of initial seeds selected at random (top row), where the subsequent feasible activations for each muscle are limited in where they can go given the activation-contraction speed of 0.25. As we do observe many changes in the profiles of trajectories when time is considered, and do not observe changes in some of the by-muscle distributions (as seen in Supplementary Figure 4.8, traditional

Figure 4.6: **The effect of differing activation-contraction constraints on the distribution of max($|\dot{a}_i|$), compared across muscles** When we sample trajectories, we get a bunch of n-dimensional trajectories, where n=7 muscles. From each of those trajectories, we differentiate them (e.g. $\dot{a}_i = a_{i+1}^{LUM} - a_i^{LUM}$), and we show here the distributions of e.g. $\dot{a}^{LUM}$. These speeds are grouped by the applied activation-contraction constraint. The case with no activation-contraction constraints is a 1.0; a 0.1 means a muscle is spatiotemporally constrained so that it cannot change by more than 10% within 50ms.

techniques for visualizing these spaces, including density distributions and parallel coordinates as used in

[30] could be misleading on the raw activations, when incorporating the concept of time.

Figure 4.7: **Spatiotemporal tunnels for each of 10 seed points** The 'seed' activation you choose in the first moment highly constrains where your muscle activations can go across the following six tasks. Shown for a activation-contraction constraint of 0.12 (in that no muscle can change more than 12% in tension from slice to slice). Each slice of the tunnel is a task, where the points have been projected onto the unseeded PCs (PC1 and PC2), which were computed separated for each slice, providing polytope-relevant changes in the distributions of seeded distributions with respect to the unseeded trajectory distribution.

Finally, the hypothesis illustrated conceptually in Figure 4.1 is highly supported by data in Figure

4.7. We show how, for ten randomly selected seed points, the activation-contraction constraints shown

in Figure 4.2 limit the evolution of muscle activations over time to produce a force and cyclically change

its direction. To create an adequate visualization, we had to find a method to fairly represent, project, and render the 49-dimensional space of trajectories onto a page as a 2D representation. We achieved this objective through a series of relative PCA mappings: we take many trajectories, split them into individual moments, compute the first two principal components, then project those points onto PC1 and PC2. The result is a view of the feasible activation space as a distribution landscape. From there, we make use of this visualization by projecting seeded trajectories onto those same PC's (See Figure 4.4), all culminating in a visible window into the effect of adding activation-contraction constraints, Figure 4.7. These 'tunnels' represent a representation of time-constrained activations over time, given a starting point in t=0. A single seed point defines where the activation must move, highly limiting the space of feasible activation patterns that can be used to achieve the rest of the task; a spatiotemporal tunnel exists.

4.5 Discussion

Activation-contraction constraints highly affect the neuromuscular control landscape upon which all learning, motor control, and evolution must operate. This work has strong implications to many elements of control systems where a null space exists for a relatively static task. One such example is the positioning of the tongue in production of varying vowel sounds, where the 10 muscles can yield multiple motor patterns which "result in similar tongue position, shape, and/or contacts with the palate"[49]. In extension to changing vowels over a short timespan, a perspective borne from spatiotemporal feasibility implies that speaking a single word requires finding, selecting, and repeating feasible activation trajectories so as to be intelligible. Even a few millimeters of variance in tongue and jaw position can yield distinguishably-different vowels[162]. With production of sound being highly dependent on anatomy at the species and within-population level [128], neuromuscular strategies for manipulating the characteristics of sound define the "universal inventory of phonemic contrasts available for use in language"[120]. This example serves as just one new perspective generated by our research.

Variability across all valid solutions does not necessarily decrease in light of activation-contraction constraints becoming more strict. The *utility* of a muscle has been described many times as a description of the bounds within which that muscle can be used [113, 30, 145, 62]. Our work highlights how those bounds are too optimistic a bound for time-varying evaluations of spatiotemporal feasibility, even in a very simplistic force redirection task.

Many experimental studies suggest that a pair of muscles can be highly correlated with one another, and these techniques have been leveraged to build lower dimensional representations of motor patterns, including with our work [30]. Looking at this simple force-redirection action, and the strong spatiotemporal effects, it's clear that any synergies or motor primitives would also be subject to similar constraints at a higher level. Control of these spaces with lower dimensional approximations, if learned or evolved, could be able to leverage the consistency of activations across small tasks, suggesting that planning the activation for the last set of the movement in a feed-forward manner represents a selection from a greatly reduced feasible activation space, as per Figure 4.7. As these muscles don't have to change very much, this alludes to there being solutions that could be less tiresome to implement and repeat—solutions that could be preferentially turned into motor habits. We see the effects upon the control strategies that are possible, and as these constraints twist and change over the course of ontogeny, we enlighten some elements of how motor control is intertwined between the physics and anatomy we inherit, and the muscles and control strategies we build and learn.

The nature of activation-contraction constraints have implications on our interpretations of sensorimotor manifolds and the latent representation that animals have for neuromuscular control spaces[77]. Random sampling of the raw 7-dimensional activation space is statistically untenable, and when poised with a real task of force redirection, sampling a point on the feasible trajectory space is impossible. If an individual has variability due to hierarchical sensorimotor control, it is possible to apply spatiotemporal feasibility modelling to understand how those tremorous activations affect the set of solutions for achieving a given redirection or scaling task. Furthermore, examining motor noise in this context creates a smaller

subset of possible actions that the CNS can perform, so we can address some of the mechanisms on the physical endpoint. This work is highly compatible with sensory representations as well[121, 126].

Ultimately, these neuromuscular landscapes have existed throughout history; this work is conducive to comparing posture-specific spatiotemporal structures, as well as cross-species comparisons of spatiotemporal tunneling in the context of evolutionary biology, for example, in comparing the index finger manipulability between humans and bonobos[124]. With the wealth of cadaveric, computational, and in-vivo studies, there is a wide variety of future comparisons to support ongoing research into muscle redundancy [122, 94].
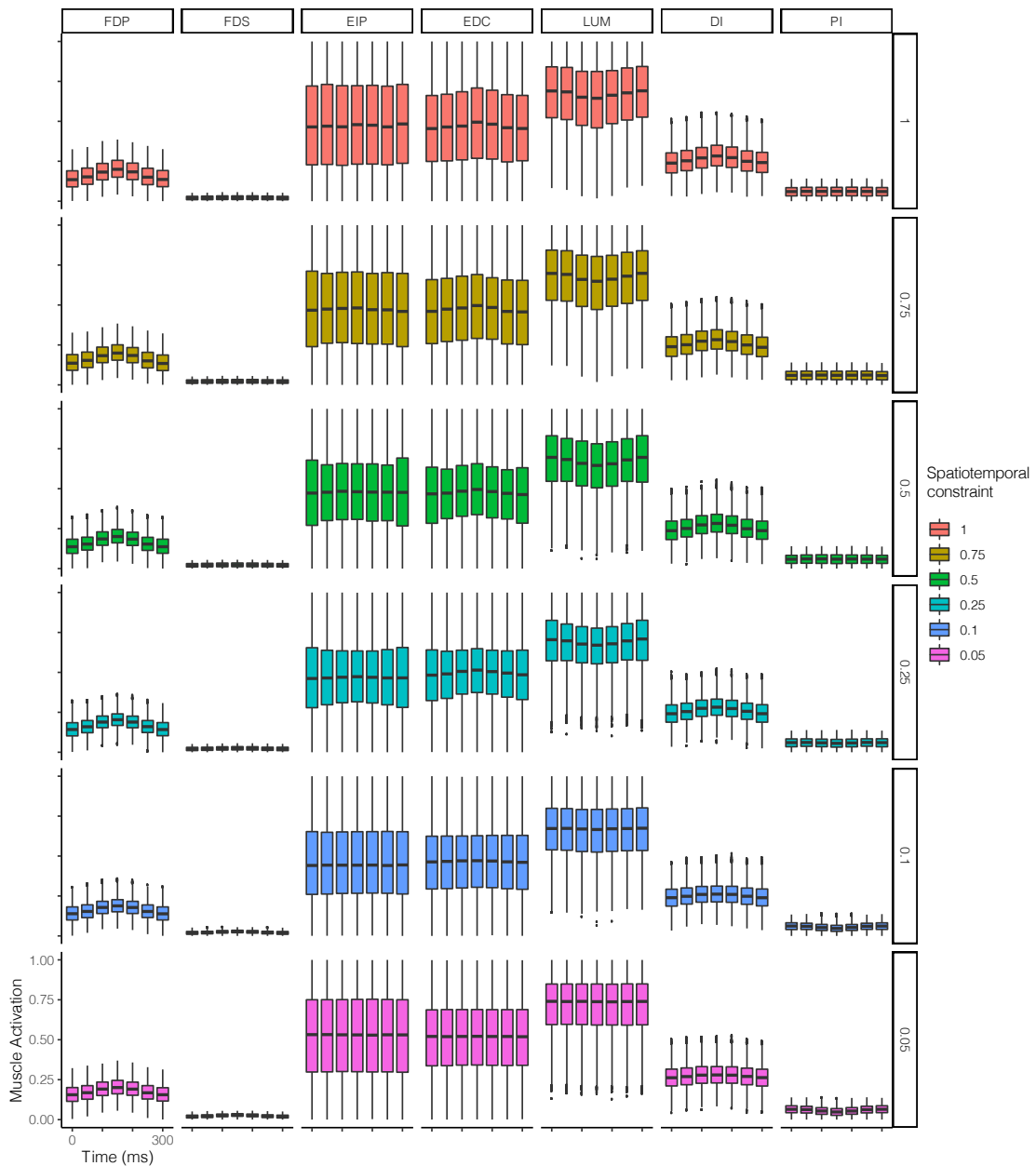
4.6   Supplementary Information

These methods were (computationally) performant within 49 dimensional trajectory space (taking c. 40 minutes per 100,000 sampled points), but we are hesitant to make claims for this method supporting higher dimensionality. Evaluation of these claims in a model with many more muscles e.g. n=31 muscles in a cat hindlimb model [113, 140] is a viable next step. Primarily the longest operation is the removal of redundant constraints, and the selection of the first hit-and-run point, and although we have made multiple steps toward parallelizing and memoising some of these operations across multiple runs, some complexities of spatiotemporal sampling may be intractable at their core, requiring invention of new methods.

We describe how activation distributions (undifferentiated) change with respect to their variance in Figure 4.9, highlighting how the variance in the by-muscle, by-moment distributions are affected by time, and how that effect is permuted by activation-contraction constraint. Intensifying activation-contraction constraint from 1 to 0.5 for EIP meant both a reduction in the general variance, but over time the line dips deeper under activation-contraction constraint up to 0.25, but then becomes more shallow and consistent as constraints move toward 0.05. The same trend is observed with EDC and LUM. The variance of the muscle activation space for FDP, FDS, DI and PI are much more consistent across differing activation-contraction constraint. This suggest that when we observe the structure of the feasible activation space

under activation-contraction constraint, those constraints may not change the distribution or span of a given by-muscle utility distribution.
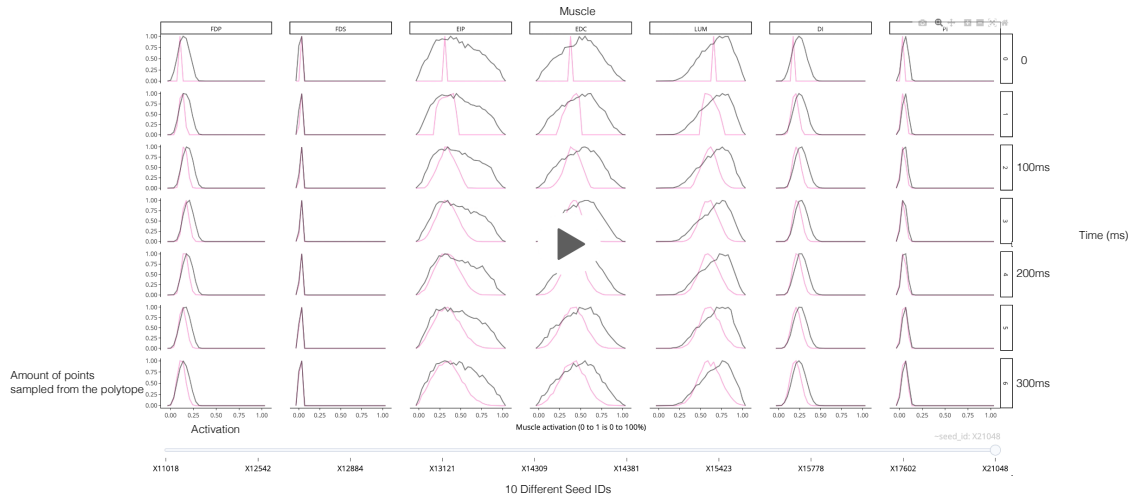
We will make code for computing spatiotemporal feasibility sampling available under an MIT License at https://github.com/bc/feasibilitytheory.
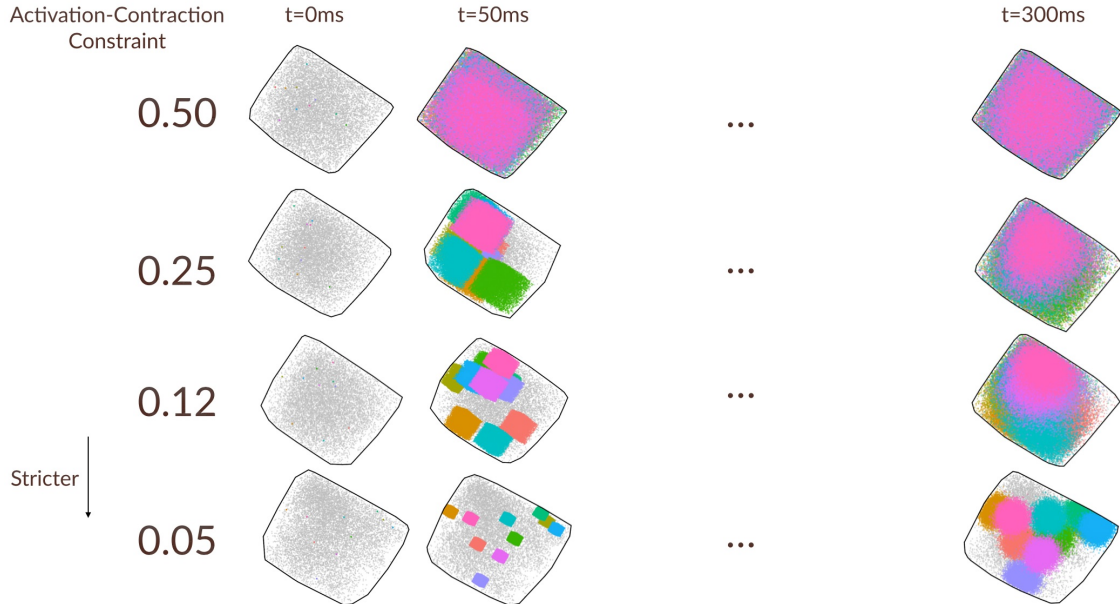
Figure 4.8: **Activation distributions under differing activation-contraction constraints** Taking all of the points collected, we group them by muscle, task, and by the spatiotemporal constraint under which they were collected. You can see each color represents a different spatiotemporal constraint, and the boxplots represent the way each muscle was used, at that task index. All trajectories sampled are unseeded.

Figure 4.9: **Supplemental Figure: Variance of a across trajectories (within a given muscle) does not necessarily go down as the feasible activation space is under more strict activation-contraction constraint** Given the velocity constraints, we extract a long series of activations for each muscle, at each task index. Per muscle, we computed the variance of each series, creating a visualization of the feasible activation space as the task is performed, and across differing activation-contraction constraint (and the degenerate case). dimensions are barely affected by either the change in the task, nor by the activation-contraction constraint. variance, and also had a bigger effect in their variance shrinking under more activation-contraction constraint. Temporal constraint led to reduction in variance across those muscles, indicating that the distribution across the muscle may become more uniformly distributed

Figure 4.10: **Interactive seed trajectory explorer** In comparing unseeded distributions with seeded distributions, we designed an interactive data exploration supplement to highlight how different the seeded trajectories could be, and how they were often highly constrained by their activation in t=0. **Bottom:** we provided a slider so the user could change the seeds, and see how the distributions compared with the unseeded distribution (which remained constant across all seeds, for this given redirection task). Lines are drawn by connecting the midpoints of 100 histogram bins.

Figure 4.11: **Spread of different seed points under varying activation contraction constraints**

4.7 Conclusion and ongoing work

For vertebrate limbs with many more muscles than degrees of freedom, with billions of neural connections, and with many ways to solve a given force, movement, or manipulation task, the question remains: how does the nervous system solve these highly under-constrained problems, and why do they solve it that way? It's remained a challenge to understand the root of the variance—even the best models are not always right. With this work's alternative approach to motor control, rather than observing *how* muscles work across a task, we define *why* muscles must work a certain way. The work presented herein serves as a strong foundation to build new neuromuscular control studies. Work from Cohn et. al. 2018 has a place in contextualizing studies of motor control, [117, 111, 103, 37, 112] and this work led to a good application of feasibility theory at the intersection of tendon-driven control and task-based optimization [84]. The whole of this work is focused on a simple isometric task, as it is a stable system, and building a strong framework requires strong assumptions as a foundation—this focus on isometric of course raises questions about posture-dependent control strategies, and the implications for movement. Work from [6] suggests that a series of static tasks have a similar analytical solution with respect to dynamical solutions–and although these methods could be applied directly as a series of static tasks (with a changing H matrix going down the diagonal of the constraint matrix), there lie many opportunities in expanding dynamical system representation into a linear subspace that can be sampled fairly. By working our way from the task, through the bones and joints of the hand, and finally into the requirements on the tendon tensions, we clearly render a new view of the solution set the nervous system (brain and spinal cord) has to pick from. In doing so, we provide deep context into the choice of neuromuscular control. Ultimately, this work highlights the way animals control their muscles for simple tasks, across both timescales of evolutionary-derivation and lifelong-learning.

Reference List

[1] Karen E Adolph, Whitney G Cole, Meghana Komati, Jessie S Garciaguirre, Daryaneh Badaly, Jesse M Lingeman, Gladys LY Chan, and Rachel B Sotsky. How do you learn to walk? thousands of steps and dozens of falls per day. *Psychological science*, 23(11):1387–1394, 2012.

[2] Cristiano Alessandro, Filipe O Barroso, Adarsh Prashara, David P Tentler, Hsin-Yun Yeh, and Matthew C Tresch. Coordination amongst quadriceps muscles suggests neural regulation of internal joint stresses, not simplification of task performance. *Proceedings of the National Academy of Sciences*, 117(14):8135–8142, 2020.

[3] Cristiano Alessandro, Ioannis Delis, Francesco Nori, Stefano Panzeri, and Bastien Berret. Muscle synergies in neuroscience and robotics: from input-space to task-space perspectives. *Frontiers in computational neuroscience*, 7, 2013.

[4] K. N. An, E. Y. Chao, W. P. Cooney, and R. L. Linscheid. Forces in the normal and abnormal hand. *J Orthop Res*, 3(2):202–211, 1985.

[5] Kai-Nan An, Y Ueba, EY Chao, WP Cooney, and RL Linscheid. Tendon excursion and moment arm of index finger muscles. *Journal of biomechanics*, 16(6):419–425, 1983. Publisher: Elsevier.

[6] Frank C Anderson and Marcus G Pandy. Static and dynamic optimization solutions for gait are practically equivalent. *Journal of biomechanics*, 34(2):153–161, 2001.

[7] Michael A Arbib. Levels of modeling of mechanisms of visually guided behavior. *Behavioral and Brain Sciences*, 10(3):407–436, 1987. Publisher: Cambridge University Press.

[8] Edith M Arnold, Samuel R Ward, Richard L Lieber, and Scott L Delp. A model of the lower limb for analysis of human movement. *Annals of biomedical engineering*, 38(2):269–279, 2010.

[9] D. Avis and K. Fukuda. A pivoting algorithm for convex hulls and vertex enumeration of arrangements and polyhedra. *Discrete & Computational Geometry*, 8(3):295–313, 1992.

[10] Myroslav Bachynskyi, Antti Oulasvirta, Gregorio Palmas, and Tino Weinkauf. Biomechanical simulation in the analysis of aimed movements. In *CHI'13 Extended Abstracts on Human Factors in Computing Systems*, pages 277–282. ACM, 2013.

[11] RD Beer. Intelligence as adaptove behaviour, volume 6 of perspectives in artificial intelligence, 1990.

[12] Richard Bellman and Howard Osborn. Dynamic programming and the variation of green's functions. *Journal of Mathematics and Mechanics*, pages 81–85, 1958.

[13] Richard E Bellman. *Adaptive control processes: a guided tour*. Princeton university press, 2015.

[14] Denise J Berger and Andrea d'Avella. Effective force control by muscle synergies. *Frontiers in computational neuroscience*, 8, 2014.

[15] Max Berniker, Megan K O'Brien, Konrad P Kording, and Alaa A Ahmed. An examination of the generalizability of motor costs. *PloS one*, 8(1):e53759, 2013.

[16] Nikolai Bernstein. The co-ordination and regulation of movements. *The co-ordination and regulation of movements*, 1966. Publisher: Pergamon Press.

[17] Emilio Bizzi and Vincent CK Cheung. The neural origin of muscle synergies. *Frontiers in computational neuroscience*, 7:51, 2013. Publisher: Frontiers.

[18] Emilio Bizzi and Vincent CK Cheung. The neural origin of muscle synergies. *Frontiers in computational neuroscience*, 7, 2013.

[19] Stephen Boyd, Stephen P Boyd, and Lieven Vandenberghe. *Convex optimization*. Cambridge university press, 2004.

[20] Oliver Brock and Francisco Valero-Cuevas. Transferring synergies from neuroscience to robotics: Comment on "hand synergies: Integration of robotics and neuroscience for understanding the control of biological and artificial hands" by m. santello et al. *Physics of life reviews*, 17:27–32, 2016.

[21] B. Büeler, A. Enge, and K. Fukuda. Exact volume computation for polytopes: A practical study. *Polytopes: Combinatorics and Computation*, 29:131–154, 2000.

[22] Luigi Cattaneo and Giacomo Rizzolatti. The mirror neuron system. *Archives of neurology*, 66(5):557–560, 2009.

[23] E Y Chao and K N An. Graphical interpretation of the solution to the redundant problem in biomechanics. *Journal of Biomechanical Engineering*, 100:159–67, 1978.

[24] E. Y. Chao and K. N. An. Graphical Interpretation of the Solution to the Redundant Problem in Biomechanics. *Journal of Biomechanical Engineering*, 100(3):159–167, 08 1978.

[25] V. Chvatal. *Linear Programming*. W.H. Freeman and Company, 1983.

[26] Flor A Cianchetti and Francisco J Valero-Cuevas. Anticipatory control of motion-to-force transitions with the fingertips adapts optimally to task difficulty. *Journal of neurophysiology*, 103(1):108–116, 2009.

[27] Robert H Clewley, John M Guckenheimer, and Francisco J Valero-Cuevas. Estimating effective degrees of freedom in motor systems. *IEEE Transactions on Biomedical Engineering*, 55(2):430–442, 2008.

[28] Dave Cliff. Computational neuroethology: A provisional manifesto. In *Proceedings of the first international conference on simulation of adaptive behavior on From animals to animats*, pages 29–39, 1991.

[29] Rachel O Coats, Andrew D Wilson, Winona Snapp-Childs, Aaron J Fath, and Geoffrey P Bingham. The 50s cliff: perceptuo-motor learning rates across the lifespan. *PloS one*, 9(1):e85758, 2014.

[30] Brian A Cohn, May Szedlák, Bernd Gärtner, and Francisco J Valero-Cuevas. Feasibility theory reconciles and informs alternative approaches to neuromuscular control. *Frontiers in computational neuroscience*, 12:62, 2018.

[31] Kelly J Cole. Age-related directional bias of fingertip force. *Experimental brain research*, 175(2):285–291, 2006.

[32] R.D. Crowninshield and R.A. Brand. A physiologically based criterion of muscle force prediction in locomotion. *Journal of Biomechanics*, 14(11):793–801, 1981.

[33] Andrea d' Avella and Emilio Bizzi. Shared and specific muscle synergies in natural motor behaviors. *Proceedings of the National Academy of Sciences of the United States of America*, 102(8):3076–3081, 2005.

[34] Andrea d' Avella, Philippe Saltiel, and Emilio Bizzi. Combinations of muscle synergies in the construction of a natural motor behavior. *Nature neuroscience*, 6(3):300, 2003.

[35] Aymar De Rugy, Gerald E Loeb, and Timothy J Carroll. Muscle coordination is habitual rather than optimal. *The Journal of Neuroscience*, 32(21):7384–7391, 2012.

[36] Vincent De Sapio, Darren Earl, Rush Green, and Katherine Saul. Human factors simulation using demographically tuned biomechanical models. In *Proceedings of the Human Factors and Ergonomics Society Annual Meeting*, volume 58, pages 944–948. SAGE Publications Sage CA: Los Angeles, CA, 2014.

[37] Jonathan B Dingwell and Joseph P Cusumano. Humans use multi-objective control to regulate lateral foot placement when walking. *PLoS computational biology*, 15(3):e1006850, 2019.

[38] Jonathan B Dingwell, Joby John, and Joseph P Cusumano. Do humans optimally exploit redundancy to control step variability in walking? *PLoS computational biology*, 6(7), 2010. Publisher: Public Library of Science.

[39] Jonathan B Dingwell, Joby John, and Joseph P Cusumano. Do humans optimally exploit redundancy to control step variability in walking? *PLoS computational biology*, 6(7):e1000856, 2010.

[40] J Maxwell Donelan, David W Shipman, Rodger Kram, and Arthur D Kuo. Mechanical and metabolic requirements for active lateral stabilization in human walking. *Journal of biomechanics*, 37(6):827–835, 2004.

[41] M. Dyer, A. Frieze, and R. Kannan. A random polynomial time algorithm for approximating the volume of convex bodies. *Proc. of the 21st annual ACM Symposium of Theory of Computing*, pages 375–381, 1989.

[42] Leonardo Abdala Elias, Renato Naville Watanabe, and André Fabio Kohn. Spinal mechanisms may provide a combination of intermittent and continuous control of human posture: predictions from a biologically based neuromusculoskeletal model. *PLoS computational biology*, 10(11), 2014. Publisher: Public Library of Science.

[43] Ioannis Z Emiris and Vissarion Fisikopoulos. Efficient random-walk methods for approximating polytope volume. *arXiv preprint arXiv:1312.2873*, 2013.

[44] Qiushi Fu, Jason Y Choi, Andrew M Gordon, Mark Jesunathadas, and Marco Santello. Learned manipulation at unconstrained contacts does not transfer across hands. *PloS one*, 9(9):e108222, 2014.

[45] Qiushi Fu and Marco Santello. Context-dependent learning interferes with visuomotor transformations for manipulation planning. *Journal of Neuroscience*, 32(43):15086–15092, 2012.

[46] K. Fukuda. Lecture: Polyhedral computation, 2014.

[47] Juan A Gallego, Matthew G Perich, Lee E Miller, and Sara A Solla. Neural manifolds for the control of movement. *Neuron*, 94(5):978–984, 2017.

[48] Brian A Garner and Marcus G Pandy. Estimation of musculotendon properties in the human upper limb. *Annals of biomedical engineering*, 31(2):207–220, 2003. Publisher: Springer.

[49] Bryan Gick, Blake Allen, François Roewer-Després, and Ian Stavness. Speaking tongues are actively braced. *Journal of Speech, Language, and Hearing Research*, 60(3):494–506, 2017.

[50] Malcolm Gladwell. *Outliers: The story of success*. Hachette UK, 2008.

[51] Roger V Gonzalez, Thomas S Buchanan, and Scott L Delp. How muscle architecture and moment arms affect wrist flexion-extension moments. *Journal of biomechanics*, 30(7):705–712, 1997. Publisher: Elsevier.

[52] Samuel R Hamner, Ajay Seth, and Scott L Delp. Muscle contributions to propulsion and support during running. *Journal of biomechanics*, 43(14):2709–2716, 2010.

[53] Robert M Hardwick, Vikram A Rajan, Amy J Bastian, John W Krakauer, and Pablo A Celnik. Motor learning in stroke: Trained patients are not equal to untrained patients with less impairment. *Neurorehabilitation and Neural Repair*, page 1545968316675432, 2016.

[54] JS Higginson, RR Neptune, and FC Anderson. Simulated parallel annealing within a neighborhood for optimization of biomechanical systems. *Journal of biomechanics*, 38(9):1938–1942, 2005.

[55] Archibald Vivian Hill. The heat of shortening and the dynamic constants of muscle. *Proceedings of the Royal Society of London. Series B-Biological Sciences*, 126(843):136–195, 1938. Publisher: The Royal Society London.

[56] Katherine RS Holzbaur, Wendy M Murray, and Scott L Delp. A model of the upper extremity for simulating musculoskeletal surgery and analyzing neuromuscular control. *Annals of biomedical engineering*, 33(6):829–840, 2005. Publisher: Springer.

[57] Hans Hultborn. Spinal reflexes, mechanisms and concepts: from Eccles to Lundberg and beyond. *Progress in neurobiology*, 78(3-5):215–232, 2006. Publisher: Elsevier.

[58] Sarah Ann Hummel. *Frisbee flight simulation and throw biomechanics*. University of California, Davis, 2003.

[59] Joshua M Inouye, Jason J Kutch, and Francisco J Valero-Cuevas. A novel synthesis of computational approaches enables optimization of grasp quality of tendon-driven hands. *IEEE transactions on robotics*, 28(4):958–966, 2012. Publisher: IEEE.

[60] Joshua M Inouye, Jason J Kutch, and Francisco J Valero-Cuevas. Optimizing the topology of tendon-driven fingers: Rationale, predictions and implementation. In *The Human Hand as an Inspiration for Robot Hand Development*, pages 247–266. Springer, 2014.

[61] Joshua M Inouye and Francisco J Valero-Cuevas. Muscle synergies heavily influence the neural control of arm endpoint stiffness and energy consumption. *PLoS Comput Biol*, 12(2):e1004737, 2016.

[62] Valero-Cuevas F. J., Cohn B. A., Yngvason H. F., and Lawrence E. L. Exploring the high-dimensional structure of muscle redundancy via subject-specific and generic musculoskeletal models. *J Biomech*, In press, 2015.

[63] Derek G Kamper, Heidi C Fischer, and Erik G Cruz. Impact of finger posture on mapping from muscle activation to joint torque. *Clinical Biomechanics*, 21(4):361–369, 2006.

[64] Kevin G Keenan, Veronica J Santos, Madhusudhan Venkadesan, and Francisco J Valero-Cuevas. Maximal voluntary fingertip force production is not limited by movement speed in combined motion and force tasks. *Journal of Neuroscience*, 29(27):8784–8789, 2009. Publisher: Soc Neuroscience.

[65] Kevin G Keenan and Francisco J Valero-Cuevas. Experimentally valid predictions of muscle force and EMG in models of motor-unit function are most sensitive to neural properties. *Journal of neurophysiology*, 98(3):1581–1590, 2007. Publisher: American Physiological Society.

[66] Konrad P Körding and Daniel M Wolpert. Bayesian integration in sensorimotor learning. *Nature*, 427(6971):244–247, 2004.

[67] Konrad Paul Kording. Bayesian statistics: relevant for the brain? *Current Opinion in Neurobiology*, 25:130 – 133, 2014. Theoretical and computational neuroscience.

[68] Peter R Krekel, Edward R Valstar, Jurriaan De Groot, Frits H Post, Rob GHH Nelissen, and Charl P Botha. Visual analysis of multi-joint kinematic data. In *Computer Graphics Forum*, volume 29, pages 1123–1132. Wiley Online Library, 2010.

[69] Vijaya Krishnamoorthy, Simon Goodman, Vladimir Zatsiorsky, and Mark L Latash. Muscle synergies during shifts of the center of pressure by standing persons: identification of muscle modes. *Biological cybernetics*, 89(2):152–161, 2003.

[70] A D Kuo and F E Zajac. Human standing posture: multi-joint movement strategies based on biomechanical constraints. *Progress in Brain Research*, 97:349–358, 1993.

[71] Arthur D Kuo and Felix E Zajac. A biomechanical analysis of muscle strength as a limiting factor in standing posture. *Journal of Biomechanics*, 26:137–150, 1993. Publisher: Elsevier.

[72] Jason J Kutch and Francisco J Valero-Cuevas. Muscle redundancy does not imply robustness to muscle dysfunction. *Journal of biomechanics*, 44(7):1264–1270, 2011. Publisher: Elsevier.

[73] Jason J Kutch and Francisco J Valero-Cuevas. Muscle redundancy does not imply robustness to muscle dysfunction. *Journal of biomechanics*, 44(7):1264–1270, 2011.

[74] Jason J Kutch and Francisco J Valero-Cuevas. Challenges and new approaches to proving the existence of muscle synergies of neural origin. *PLoS computational biology*, 8(5), 2012. Publisher: Public Library of Science.

[75] Jason J Kutch and Francisco J Valero-Cuevas. Challenges and new approaches to proving the existence of muscle synergies of neural origin. *PLoS computational biology*, 8(5):e1002434, 2012.

[76] L. Kuxhaus, S. S. Roach, and F. J. Valero-Cuevas. Quantifying deficits in the 3D force capabilities of a digit caused by selective paralysis: application to the thumb with simulated low ulnar nerve palsy. *J Biomech*, 38:725–736, Apr 2005.

[77] Alban Laflaquière, Alexander V. Terekhov, Bruno Gas, and J. Kevin O'Regan. Learning an internal representation of the end-effector configuration space. *arXiv:1810.01866 [cs, stat]*, October 2018. arXiv: 1810.01866.

[78] Catherine E Lang, Jillian R MacDonald, Darcy S Reisman, Lara Boyd, Teresa Jacobson Kimberley, Sheila M Schindler-Ivens, T George Hornby, Sandy A Ross, and Patricia L Scheets. Observation of amounts of movement practice provided during stroke rehabilitation. *Archives of physical medicine and rehabilitation*, 90(10):1692–1698, 2009.

[79] Gerald E Loeb. Overcomplete musculature or underspecified tasks? *Motor control*, 4(1):81–83, 2000. Publisher: Human Kinetics, Inc.

[80] Gerald E Loeb. Optimal isn't good enough. *Biological cybernetics*, 106(11-12):757–765, 2012.

[81] Keith R Lohse, Catherine E Lang, and Lara A Boyd. Is more better? using metadata to explore dose–response relationships in stroke rehabilitation. *Stroke*, 45(7):2053–2058, 2014.

[82] L. Lovász. Hit-and-run mixes fast. *Math. Prog.*, 86:443–461, 1998.

[83] László Lovász. Hit-and-run mixes fast. *Mathematical Programming*, 86(3):443–461, 1999.

[84] Ali Marjaninejad, Jie Tan, and Francisco J Valero-Cuevas. Autonomous control of a tendon-driven robotic limb with elastic elements reveals that added elasticity can enhance learning. *arXiv preprint arXiv:1909.12436*, 2019.

[85] Ali Marjaninejad and Francisco J. Valero-Cuevas. Should anthropomorphic systems be "redundant"? In *Biomechanics of Anthropomorphic Systems, Springer Tracts in Advanced Robotics (STAR) series*, page In Press. Springer, 2018.

[86] J Lucas McKay, Thomas J Burkholder, and Lena H Ting. Biomechanical capabilities influence postural control strategies in the cat hindlimb. *Journal of biomechanics*, 40(10):2254–2260, 2007. Publisher: Elsevier.

[87] J Lucas McKay and Lena H Ting. Functional muscle synergies constrain force production during postural tasks. *Journal of biomechanics*, 41(2):299–306, 2008. Publisher: Elsevier.

[88] Andrew Miller, P Allen, V Santos, and F Valero-Cuevas. From robotic hands to human hands: a visualization and simulation engine for grasping research. *Industrial Robot: An International Journal*, 2005. Publisher: Emerald Group Publishing Limited.

[89] Richard M Murray, Zexiang Li, S Shankar Sastry, and S Shankara Sastry. *A mathematical introduction to robotic manipulation*. CRC press, 1994.

[90] Wendy M Murray, Thomas S Buchanan, and Scott L Delp. Scaling of peak moment arms of elbow muscles with upper extremity bone dimensions. *Journal of biomechanics*, 35(1):19–26, 2002. Publisher: Elsevier.

[91] Erhan Oztop, Mitsuo Kawato, and Michael Arbib. Mirror neurons and imitation: A computationally guided review. *Neural Networks*, 19(3):254–271, 2006.

[92] B. I. Prilutsky. Muscle coordination: the discussion continues. *Motor Control*, 4(1):97–116, 2000. 0 1087-1640 Journal article.

[93] Boris I Prilutsky. Muscle coordination: the discussion continues. *Motor Control*, 4(1):97–116, 2000. Publisher: Human Kinetics, Inc.

[94] Dan Qiu and Derek G Kamper. Orthopaedic applications of a validated force-based biomechanical model of the index finger. In *2014 36th Annual International Conference of the IEEE Engineering in Medicine and Biology Society*, pages 4013–4016. IEEE, 2014.

[95] Kornelius Rácz, Daniel Brown, and Francisco J Valero-Cuevas. An involuntary stereotypical grasp tendency pervades voluntary dynamic multifinger manipulation. *Journal of neurophysiology*, 108(11):2896–2911, 2012.

[96] Kornelius Rácz and Francisco J Valero-Cuevas. Spatio-temporal analysis reveals active control of both task-relevant and task-irrelevant variables. *Frontiers in computational neuroscience*, 7, 2013.

[97] Giby Raphael, George A Tsianos, and Gerald E Loeb. Spinal-like regulator facilitates control of a two-degree-of-freedom wrist. *Journal of Neuroscience*, 30(28):9431–9444, 2010.

[98] John A Rieffel, Francisco J Valero-Cuevas, and Hod Lipson. Morphological communication: exploiting coupled dynamics in a complex mechanical structure to achieve locomotion. *Journal of the royal society interface*, 7(45):613–621, 2010. Publisher: The Royal Society.

[99] Kornelius Rácz and Francisco Valero-Cuevas. Spatio-temporal analysis reveals active control of both task-relevant and task-irrelevant variables. *Frontiers in computational neuroscience*, 7:155, 2013. Publisher: Frontiers.

[100] Terence D Sanger. Distributed control of uncertain systems using superpositions of linear operators. *Neural computation*, 23(8):1911–1934, 2011.

[101] Terence D Sanger, Daofen Chen, Mauricio R Delgado, Deborah Gaebler-Spira, Mark Hallett, Jonathan W Mink, and others. Definition and classification of negative motor signs in childhood. *Pediatrics*, 118(5):2159–2167, 2006. Publisher: Am Acad Pediatrics.

[102] Terence D Sanger, Daofen Chen, Darcy L Fehlings, Mark Hallett, Anthony E Lang, Jonathan W Mink, Harvey S Singer, Katharine Alter, Hilla Ben-Pazi, Erin E Butler, and others. Definition and classification of hyperkinetic movements in childhood. *Movement Disorders*, 25(11):1538–1549, 2010. Publisher: Wiley Online Library.

[103] Massimo Sartori, Francisco J Valero-Cuevas, Alfred C Schouten, Matthew Tresch, Yoshihiko Nakamura, and Manish Sreenivasa. *Neuromechanics and Control of Physical Behavior: From Experimental and Computational Formulations to Bio-inspired Technologies*. Frontiers Media SA, 2019.

[104] John P Scholz and Gregor Schöner. The uncontrolled manifold concept: identifying control variables for a functional task. *Exp Brain Res*, 126:289–306, 1999.

[105] Stephen H Scott. Optimal feedback control and the neural basis of volitional motor control. *Nature Reviews Neuroscience*, 5(7):532–545, 2004. Publisher: Nature Publishing Group.

[106] Stephen H Scott. Optimal feedback control and the neural basis of volitional motor control. *Nature Reviews Neuroscience*, 5(7):532–546, 2004.

[107] Cole S Simpson, M Hongchul Sohn, Jessica L Allen, and Lena H Ting. Feasible muscle activation ranges based on inverse dynamics analyses of human walking. *Journal of biomechanics*, 48(12):2990–2997, 2015.

[108] Cole S. Simpson, M. Hongchul Sohn, Jessica L. Allen, and Lena H. Ting. Feasible muscle activation ranges based on inverse dynamics analyses of human walking. *Journal of Biomechanics*, 48(12):2990–2997, September 2015.

[109] Robert L Smith. Efficient monte carlo procedures for generating points uniformly distributed over bounded regions. *Operations Research*, 32(6):1296–1308, 1984.

[110] M Hongchul Sohn, J Lucas McKay, and Lena H Ting. Defining feasible bounds on muscle activation in a redundant biomechanical task: practical implications of redundancy. *Journal of biomechanics*, 46(7):1363–1368, 2013.

[111] M. Hongchul Sohn, Daniel M. Smith, and Lena H. Ting. Effects of kinematic complexity and number of muscles on musculoskeletal model robustness to muscle dysfunction. *PLOS ONE*, 14(7):e0219779, July 2019.

[112] M Hongchul Sohn and Lena Ting. The cost of being stable: Trade-offs between effort and stability across a landscape of redundant motor solutions. *bioRxiv*, page 477083, 2018.

[113] M.Hongchul Sohn, J. Lucas McKay, and Lena H. Ting. Defining feasible bounds on muscle activation in a redundant biomechanical task: practical implications of redundancy. *Journal of Biomechanics*, 46(7):1363–1368, April 2013.

[114] H.H. Sohrab. *Basic Real Analysis*. Birkhäuser Boston, 2003.

[115] D Song, G Raphael, N Lan, and G E Loeb. Computationally efficient models of neuromuscular recruitment and mechanics. *Journal of Neural Engineering*, 5(2):008, June 2008.

[116] CW Spoor. Balancing a force on the fingertip of a two-dimensional finger model without intrinsic muscles. *Journal of Biomechanics*, 16(7):497–504, 1983.

[117] Manish Sreenivasa, Francisco J Valero-Cuevas, Matthew Tresch, Yoshihiko Nakamura, Alfred C Schouten, and Massimo Sartori. Neuromechanics and control of physical behavior: From experimental and computational formulations to bio-inspired technologies. *Frontiers in computational neuroscience*, 13:13, 2019.

[118] Katherine M Steele, Matthew C Tresch, and Eric J Perreault. The number and choice of muscles impact the results of muscle synergy analyses. *Frontiers in computational neuroscience*, 7, 2013.

[119] Katherine M Steele, Matthew C Tresch, and Eric J Perreault. Consequences of biomechanically constrained tasks in the design and interpretation of synergy analyses. *Journal of neurophysiology*, 113(7):2102–2113, 2015.

[120] Kenneth Noble Stevens and Samuel Jay Keyser. Quantal theory, enhancement and overlap. *Journal of Phonetics*, 38(1):10–19, 2010.

[121] Giovanni Sutanto, Nathan Ratliff, Balakumar Sundaralingam, Yevgen Chebotar, Zhe Su, Ankur Handa, and Dieter Fox. Learning latent space dynamics for tactile servoing. In *2019 International Conference on Robotics and Automation (ICRA)*, pages 3622–3628. IEEE, 2019.

[122] A Synek and D H Pahr. The effect of the extensor mechanism on maximum isometric fingertip forces: A numerical study on the index finger. *Journal of Biomechanics*, 49(14):3423–3429, October 2016.

[123] Alexander Synek, Szu-Ching Lu, Sandra Nauwelaerts, Dieter H Pahr, and Tracy L Kivell. Metacarpophalangeal joint loads during bonobo locomotion: model predictions versus proxies. *Journal of the Royal Society Interface*, 17(164):20200032, 2020.

[124] Alexander Synek, Szu-Ching Lu, Evie E Vereecke, Sandra Nauwelaerts, Tracy L Kivell, and Dieter H Pahr. Musculoskeletal models of a human and bonobo finger: parameter identification and comparison to in vitro experiments. *PeerJ*, 7:e7470, 2019.

[125] Evangelos Theodorou and Francisco J Valero-Cuevas. Optimality in neuromuscular systems. In *Engineering in Medicine and Biology Society (EMBC), 2010 Annual International Conference of the IEEE*, pages 4510–4516. IEEE, 2010.

[126] Stephen Tian, Frederik Ebert, Dinesh Jayaraman, Mayur Mudigonda, Chelsea Finn, Roberto Calandra, and Sergey Levine. Manipulation by feel: Touch-based control with deep predictive models. In *2019 International Conference on Robotics and Automation (ICRA)*, pages 818–824. IEEE, 2019.

[127] Lena H Ting and Jane M Macpherson. A limited set of muscle synergies for force control during a postural task. *Journal of Neurophysiology*, 93(1):609–613, 2005.

[128] Ingo Titze, Tobias Riede, and Ted Mau. Predicting achievable fundamental frequency ranges in vocalization across species. *PLoS computational biology*, 12(6), 2016.

[129] Emanuel Todorov and Michael I Jordan. Optimal feedback control as a theory of motor coordination. *Nature neuroscience*, 5(11):1226–1235, 2002.

[130] Bert CL Touwen. *Neurological development in infancy*. Heinemann London, 1976.

[131] Joseph D Towles, Vincent R Hentz, and Wendy M Murray. Use of intrinsic thumb muscles may help to improve lateral pinch function restored by tendon transfer. *Clinical Biomechanics*, 23(4):387–394, 2008.

[132] Matthew C Tresch. A balanced view of motor control. *Nature Neuroscience*, 10(10):1227–1228, 2007.

[133] Matthew C Tresch and Anthony Jarc. The case for and against muscle synergies. *Current opinion in neurobiology*, 19(6):601–607, 2009.

[134] M.C. Tresch, V.C.K. Cheung, and A. d'Avella. Matrix factorization algorithms for the identification of muscle synergies: evaluation on simulated and experimental data sets. *Journal of neurophysiology*, 95(4):2199–2212, 2006.

[135] Ursula Trinler, Kristen Hollands, Richard Jones, and Richard Baker. A systematic review of approaches to modelling lower limb muscle forces during gait: applicability to clinical gait analyses. *Gait & posture*, 61:353–361, 2018.

[136] George A Tsianos, Cedric Rustin, and Gerald E Loeb. Mammalian muscle model for predicting force and energetics during physiological behaviors. *IEEE Transactions on Neural Systems and Rehabilitation Engineering*, 20(2):117–133, 2011.

[137] Dimitrios Tsirakos, Vasilios Baltzopoulos, and Roger Bartlett. Inverse optimization: functional and physiological considerations related to the force-sharing problem. *Critical Reviews^{TM} in Biomedical Engineering*, 25(4-5), 1997.

[138] F J Valero-Cuevas. Predictive modulation of muscle coordination pattern magnitude scales fingertip force magnitude over the voluntary range. *J Neurophysiol*, 83(3):1469–1479, 2000.

[139] F. J. Valero-Cuevas. A mathematical approach to the mechanical capabilities of limbs and fingers. *Adv. Exp. Med. Biol.*, 629:619–633, 2009.

[140] F. J. Valero-Cuevas, B. A. Cohn, H. F. Ingvason, and E. L. Lawrence. Exploring the high-dimensional structure of muscle redundancy via subject-specific and generic musculoskeletal models. *Journal of biomechanics*, 48(11):2887–2896, August 2015.

[141] F. J. Valero-Cuevas and V. R. Hentz. Releasing the A3 pulley and leaving flexor superficialis intact increases pinch force following the Zancolli lasso procedures to prevent claw deformity in the intrinsic palsied finger. *J. Orthop. Res.*, 20:902–909, Sep 2002.

[142] F. J. Valero-Cuevas, H. Hoffmann, M. U. Kurse, J. J. Kutch, and E. A. Theodorou. Computational models for neuromuscular function. *IEEE Reviews in Biomedical Engineering (2) October*, page 110ñ135, 2009.

[143] F. J. Valero-Cuevas, M. Venkadesan, and E. Todorov. Structured variability of muscle activations supports the minimal intervention principle of motor control. *J. Neurophysiol.*, 102:59–68, Jul 2009.

[144] F. J. Valero-Cuevas, F. E. Zajac, and C. G. Burgar. Large index-fingertip forces are produced by subject-independent patterns of muscle excitation. *J Biomech*, 31:693–703, Aug 1998.

[145] FJ Valero-Cuevas, BA Cohn, M Szedlák, K Fukuda, and B Gärtner. Structure of the set of feasible neural commands for complex motor tasks. In *Conference proceedings of the Annual International Conference of the IEEE Engineering in Medicine and Biology Society. IEEE Engineering in Medicine and Biology Society. Annual Conference*, volume 2015, page 1440. NIH Public Access, 2015.

[146] F.J. Valero-Cuevas, H. Hoffmann, M.U. Kurse, J.J. Kutch, and E.A. Theodorou. Computational models for neuromuscular function. *Biomedical Engineering, IEEE Reviews in*, 2:110–135, 2009.

[147] Francisco J Valero-Cuevas. An integrative approach to the biomechanical function and neuromuscular control of the fingers. *Journal of biomechanics*, 38(4):673–684, 2005.

[148] Francisco J Valero-Cuevas. A mathematical approach to the mechanical capabilities of limbs and fingers. In *Progress in motor control*, pages 619–633. Springer, 2009.

[149] Francisco J Valero-Cuevas. *Fundamentals of Neuromechanics*, volume 8 of *Biosystems and Biorobotics*. SpringerVerlag London, 2015.

[150] Francisco J Valero-Cuevas, Vikrant V Anand, Anupam Saxena, and Hod Lipson. Beyond parameter estimation: Extending biomechanical modeling by the explicit exploration of model topology. *IEEE Transactions on Biomedical Engineering*, 54(11):1951–1964, 2007. Publisher: IEEE.

[151] Francisco J Valero-Cuevas, Heiko Hoffmann, Manish U Kurse, Jason J Kutch, and Evangelos A Theodorou. Computational models for neuromuscular function. *IEEE Reviews in Biomedical Engineering*, 2:110–135, 2009. Publisher: IEEE.

[152] Francisco J Valero-Cuevas, Verena Klamroth-Marganska, Carolee J Winstein, and Robert Riener. Robot-assisted and conventional therapies produce distinct rehabilitative trends in stroke survivors. *Journal of neuroengineering and rehabilitation*, 13(1):92, 2016.

[153] Francisco J Valero-Cuevas and Marco Santello. On neuromechanical approaches for the study of biological and robotic grasp and manipulation. *Journal of neuroengineering and rehabilitation*, 14(1):101, 2017.

[154] Francisco J Valero-Cuevas, Joseph D Towles, and Vincent R Hentz. Quantification of fingertip force reduction in the forefinger following simulated paralysis of extensor and intrinsic muscles. *Journal of biomechanics*, 33(12):1601–1609, 2000.

[155] Francisco J Valero-Cuevas, Jae-Woong Yi, Daniel Brown, Robert V McNamara, Chandana Paul, and Hood Lipson. The tendon network of the fingers performs anatomical computation at a macroscopic scale. *IEEE Transactions on Biomedical Engineering*, 54(6):1161–1166, 2007. Publisher: IEEE.

[156] Francisco J Valero-Cuevas, Felix E Zajac, and Charles G Burgar. Large index-fingertip forces are produced by subject-independent patterns of muscle excitation. *Journal of biomechanics*, 31(8):693–703, 1998. Publisher: Elsevier.

[157] M. Venkadesan and F. J. Valero-Cuevas. Neural control of motion-to-force transitions with the fingertip. *J. Neurosci.*, 28:1366–1373, Feb 2008.

[158] Madhusudhan Venkadesan and Francisco J Valero-Cuevas. Neural control of motion-to-force transitions with the fingertip. *Journal of Neuroscience*, 28(6):1366–1373, 2008. Publisher: Soc Neuroscience.

[159] F. E. Zajac. Muscle coordination of movement: a perspective. *J Biomech*, 26 Suppl 1:109–124, 1993.

[160] Felix E Zajac. Muscle and tendon: properties, models, scaling, and application to biomechanics and motor control. *Critical reviews in biomedical engineering*, 17(4):359–411, 1989.

[161] E Paul Zehr and Richard B Stein. What functions do reflexes serve during human locomotion? *Progress in neurobiology*, 58(2):185–205, 1999. Publisher: Elsevier.

[162] Zhaoyan Zhang. Mechanics of human voice production and control. *The journal of the acoustical society of america*, 140(4):2614–2635, 2016.